Technische Universität München

Max-Planck-Institut für Quantenoptik

# Nonlinear spectroscopy of a single-atom-cavity system

## Ingrid Schuster

Vollständiger Abdruck der von der Fakultät für Physik
der Technischen Universität München
zur Erlangung des akademischen Grades eines

Doktors der Naturwissenschaften (Dr. rer. nat.)

genehmigten Dissertation.

Vorsitzender: Univ.-Prof. Dr. H. Friedrich

Prüfer der Dissertation: 1. Hon.-Prof. Dr. G. Rempe
2. Univ.-Prof. Dr. R. Gross

Die Dissertation wurde am 05.06.2008
bei der Technischen Universität München eingereicht
und durch die Fakultät für Physik am 04.07.2008 angenommen.

# Abstract

The radiative properties of an atom are not only determined by its internal structure, but also by its environment. By modifying the density of the surrounding electromagnetic modes, the interaction of an atom with light can be increased significantly. Such a situation is realized for an atom placed inside a cavity which supports only a single mode. If the coupling of the atom to this privileged mode exceeds the interaction of atom and cavity with the external modes, a new system with its own characteristic energy structure emerges. This constitutes the 'strong-coupling regime' of cavity-QED. Here, the energy levels of the system form a ladder of doublets. The first doublet has a classical interpretation -the normal-mode splitting resulting from a harmonic dipole oscillator being coupled to an electromagnetic field-, and has been experimentally observed in the spectrum of various types of cavity-QED systems.

This thesis reports on the first experimental observation of a higher-doublet state in the transmission spectrum of an optical cavity-QED system, consisting of a single rubidium atom which is localized in the mode of a high-finesse Fabry-Pérot type microcavity by means of an intracavity dipole trap. When probing the system at low intensity, only single-photon transitions to the first doublet are driven, and the spectrum reveals the normal modes. For rising intensities, a state consisting of two photons strongly coupled to the atom is populated via a two-photon transition, visible as an additional resonance at a characteristic frequency and with an amplitude rising quadratically with the probe intensity.

The observed transmission spectra are compared to different theory models. Only the quantum model, in which a two-level atom is coupled to a quantized cavity mode, is able to reproduce the measurements, whereas theories for a classical field fail to explain the data. These results prove the quantum nature of the combined atom-cavity system in the optical domain and show that states consisting of a single atom entangled with a quantized field are experimentally accessible, paving the way for more fundamental studies on this model system for light-matter interaction.

# Contents

# List of Figures

# Chapter 1

# Introduction

Nearly one hundred years ago, Max Planck introduced the idea of quantizing the exchange of energy between the electromagnetic field and matter in order to explain the spectrum of black-body radiation [1]; a few years later, the quantum hypothesis was extended by Albert Einstein's explanation of the photoelectric effect [2]. The origins of quantum theory actually lie in the interpretation of electrodynamical processes between matter and light, and quantum electrodynamics (QED) has remained an area of active research until today.

A single atom coupled to a single mode of the radiation field became a model system for the fundamental study of QED. This system has been experimentally realized in the domain of cavity QED, which exploits the modified mode density in confined space, for example between two highly reflecting mirrors, to resonantly enhance the interaction of an atom with only one mode sustained by the cavity. Depending on the quality of the cavity mirrors, this coherent interaction can dominate the incoherent coupling of the atom and the cavity field to the non-privileged modes of the surrounding vacuum. Such a situation marks the strong-coupling regime of cavity QED [3]: atom and photons lose their respective identities to form a bound system with unique characteristics.

The seminal work of Jaynes and Cummings [4] constitutes the first theoretical study of the strong-coupling regime. A central result was the description of the energy eigenstates of the coupled system, which consist of a ladder of doublet states ('dressed states') with anharmonic splitting, mirroring the two-state atom coupled to the equidistant ladder of Fock states of the quantized light field. The frequency splitting of a given doublet defines the Rabi frequency, i.e. the rate at which energy is exchanged between the atom and the light field. This splitting depends on the square root of the number of photons in the mode; thereby the quantization of matter-light interaction becomes accessible to experimental observation.

Experiments can be divided into two domains: microwave and optical cavity QED. The first experimental realization of strong coupling of a single atom to a cavity field was achieved with superconducting microwave resonators at cryogenic temperatures [5], which are characterized by extremely long field decay times of up to several 100 ms [6, 7]. Using alkali atoms in a long-lived, highly excited Rydberg state, coherent evolution of the coupled system is mostly limited by the transit time of atoms passing through the cavity and can be observed through the appearance of Rabi oscillations in the atomic state behind the interaction zone (see [8, 9] for a review). The anharmonicity of the energy-level structure and thus bound atom-photon states were first seen in the time domain via the collapse and revival of these Rabi oscillations [10, 11].

In the optical regime, both coupling and decoherence of atom and cavity field evolve on a much faster timescale, which prohibits monitoring the system via the detection of the short-lived atomic state. Instead, information is obtained by detecting photons which escape from the cavity; in contrast to microwaves, excellent photodetectors are available at optical wavelengths. Here, the loss of photons from the cavity is not a detrimental decoherence process, but rather allows for continuous observation, as is necessary, for example, for studies on the conditional evolution of an open quantum system [12, 13].

The energy-level structure of an optical cavity-QED system can be probed in a spectroscopy experiment. A splitting due to the first doublet of dressed states has already been observed in the spectrum of several of such systems [14, 15, 16, 17, 18, 19, 20]; the observation of this 'normal-mode splitting' has been established as a benchmark measurement for having entered the strong-coupling regime. But only the observation of the higher states promises essential insight into the physical nature of the underlying system. The normal modes by themselves can be explained by three theories [21]: Firstly, by classical linear dispersion theory [14] or a model of coupled harmonic oscillators; secondly, in a mixed classical-quantum approach by combining a classical light field with a quantized two-state atom, leading to the bistability state equation [22]; and finally in the frame of quantum mechanics, quantizing both atom and light field. Only the higher states, which are predicted exclusively in the quantum picture, allow to confirm its validity in this context. For this reason, spectroscopic observation of the higher dressed states has been an incentive for several theory proposals [23, 24, 25] and is also a goal for cavity-QED systems outside atomic physics [26, 27].

The central result of this thesis is the first experimental observation of a dressed state beyond the first doublet in a spectroscopy experiment, performed with a single atom trapped inside a high-finesse cavity. This state, consisting of two photons strongly coupled to one atom, is excited directly by driving a two-photon transition from the ground state of the system. A resonance appears in the spectrum which is distinct from the normal-mode resonances, owing to the anharmonicity of the level splitting in the Jaynes-Cummings model. Introducing another scan technique to cross a parameter region which is devoid of any classical resonances, the quantum resonances are probed exclusively. The observed peaks in the spectra provide direct proof of the quantization of atom-field interaction in the optical regime, which up to now could be evidenced only indirectly in experiments monitoring fluctuations in the intensity of the transmitted cavity field [28, 29, 30, 31].

The success of this experiment relied on both physical insights and technological knowledge about optical cavity-QED systems in the strong-coupling regime which has been gained in the course of many years of previous measurements. The challenge to achieve coherent coupling rates which surpass the cavity linewidth as well as the typical linewidth of optical dipole transitions was mastered in the 1990s, after it became possible to produce extremely high-reflecting dielectric mirrors [32]. Optical cavities critically depend on a small mode volume, with a mirror separation on the order of 100 $\mu$m and an even smaller mode waist; therefore very slow atoms were required to achieve transit times long enough for the observation of coupling effects on the single-atom level. Consequently, optical cavity QED greatly profited from the advance of laser-cooling and trapping techniques [33, 34, 35], which opened the possibility of preparing cold atomic samples and slow atomic beams. By diluting the flux, it became possible to observe the transit of single atoms through the cavity mode [36, 37], and use the forces exerted by a cavity field containing only few photons to localize the atoms inside the mode for a short time [38, 39].

The atomic motion inside the resonator is governed by forces which differ considerably from the ones acting on an atom within a laser beam in free space [40, 41, 42, 43, 44, 45]. On the one hand, diffusion of the atom is enhanced due to fluctuations in the cavity light field, on the other hand, the finite linewidth of the cavity leads to a delayed adjustment of the cavity field to the position of a moving atom. This mechanism is at the base of a very efficient cooling method [46], which is most useful in connection with a dipole trap to localize the atom.

The implementation of dipole traps constituted a milestone in optical cavity QED with single atoms. The first intracavity dipole traps, created by exciting additional cavity modes far-red detuned from the atomic resonance [47, 48], already helped to increase the interaction time between the atom and the mode significantly. Using a combination of cavity modes of different longitudinal and transverse orders, a blue-detuned trap has been realized which stores the atom at a place of vanishing trap light intensity [20]. Trapping beams consisting of a standing-wave pattern which can be shifted allow for a very precise control of the atomic position [49]; employing such a trap in a configuration transverse to the cavity axis, single atoms have been loaded into the cavity mode deterministically [50, 51, 52]. Combined with cavity-cooling in three dimensions, the storage time of single atoms inside the resonator was shown to increase to several seconds [53, 54].

The growing ability to localize the atom led to more and more progress in the study of the structure of the atom-cavity system. The normal-mode spectrum was first observed in thermal beam experiments [14, 15, 16, 17], down to diluted beams with single atoms passing the cavity [55]. An experiment aiming to evidence signatures of doublet states beyond the normal modes failed due to fluctuations in the number of atoms in the cavity [56]. These fluctuations are removed by using a trapped atom, as could be shown with the measurement of the normal-mode spectrum in a single-trapped-atom–cavity system [18, 19, 20].

In the experiment reported here, a red-detuned intracavity dipole trap is used to confine the atom in a region of strong coupling for a time span sufficiently long in order to separately resolve the classical and quantum resonances [57, 58]. The general features of the obtained spectra are in agreement with the predictions of a quantum theory for a motionless atom, in this way ruling out the classical and semiclassical model. A full understanding of the spectra is achieved by extensive numerical simulations, which take into account the residual motion of the atom within the trapping potential.

The employed excitation scheme contains an inherent nonlinearity in the scaling of the transition probability as a function of probe laser intensity. The two-photon resonance is observed to grow nearly quadratically with rising probe intensity. This scaling cannot be attributed to saturation of the atom, since we deliberately operate in a parameter regime where the atomic excitation probability is small. It rather is a unique quantum property of the combined atom-cavity system, which can accommodate only photon pairs at the given resonance frequency. This system therefore conveys a nonlinear interaction between two photons, mediated by only a single atom.

This thesis is organized as follows: in chapter 2, the theory of the strongly-coupled atom-cavity system, interacting with its environment, is introduced on the basis of a quantum model of a two-state atom coupled to a quantized light field. The connections of this model to the classical coupled-harmonic-oscillator model and the model of optical bistability are highlighted. Chapter 3 gives a review on previous works related to the higher-order dressed states, and puts forward a proposal for the observation of these states in an optical atom-cavity system by analyzing the expected signature of these resonances in a spectrum for the given experimental setup. In chapter 4, theory is extended to include effects due to the residual motion of the trapped atom. The experimental setup as well as the measurement and data evaluation procedure are presented in chapter 5. Chapter 6 contains the results of the measurements and the comparison to the different theories, and chapter 7 gives perspectives for future measurements and possible applications of these quantum resonances.

# Chapter 2

# Theory of the ideal strongly coupled single-atom-cavity system

A single atom strongly coupled to a single mode of a high-finesse resonator (Fig. 2.1) is a model system of quantum mechanics, allowing to research the interaction of matter and light at a fundamental level. The beauty of this system lies in its conceptual simplicity: it combines a basic unit of matter, a single atom, with the simplest form of an electromagnetic field, a single mode, in such a way that their mutual interaction surpasses any coupling to the environment. Yet this system provides a wealth of physical effects, with explanations both inside and outside the framework of classical physics, and offers a multitude of applications ranging from cooling of particles to the generation of non-classical light and the wide field of quantum information [8, 9, 59].

This chapter presents the theoretical concept on which this model is based. In section 2.1, first the energy-level structure of the closed system is derived, leading to the Jaynes-Cummings model. This model is extended to describe irreversible coupling to the environment with the help of a master equation. Now, excitation and decay of the states can be included, and ultimately, spectroscopy of the system becomes possible. Up to here, the system is treated quantum mechanically. This yields an infinite set of coupled equations for the system operators which cannot be solved analytically. In section 2.2, two different theories which can be seen as

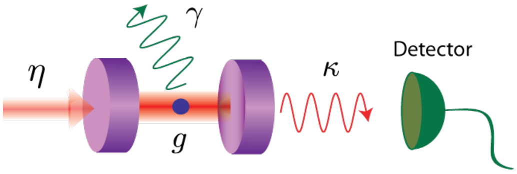

**Figure 2.1: The atom-cavity system.** A single atom is strongly coupled (coupling rate $g$) to a single mode of the electromagnetic field inside a high-finesse optical resonator. The system is coherently pumped by a laser impinging on one of the mirrors (pump strength $\eta$). Losses can arise through spontaneous emission of photons from the atom (rate $2\gamma$) and through photons lost from the mode (rate $2\kappa$), escaping from one of the mirrors. Detection of these photons allows to observe the system.

approximations to the quantum theory are presented: the classical and the semiclassical models. These models, which allow for analytical solutions, are discussed separately and finally compared to the full quantum mechanical model, which is solved numerically.

## 2.1 Quantum description of the atom-cavity system

### 2.1.1 Closed quantum system

In this section, a quantum-mechanical model for a closed atom-cavity system is derived, i.e. coupling to the environment is neglected. This model was introduced to quantum optics by Jaynes and Cummings in 1963 to describe a molecular beam maser [4], and has since become the standard model for many types of experimental atom-cavity systems and also analogous systems from other fields [60].

**Validity of the model**

This model assumes that the atom possesses only two internal states (a ground state $|g\rangle$ and an excited state $|e\rangle$), and interacts with only one mode of the electromagnetic field inside the resonator. At first, the validity of these assumptions in the experimental realization of the system needs to be verified. Usually, atoms have a complicated internal level structure due to the fine and hyperfine splitting. In the experiment, $^{85}$Rb atoms are optically pumped towards the outermost magnetic sublevel of their ground state ($^5S_{1/2}F = 3, m_f = 3$) and then driven to the excited state ($^5P_{3/2}F' = 4, m_f' = 4$) by a circularly polarized, near-resonant laser field; this effectively restricts the internal structure to two levels. The atom is placed inside a near-planar Fabry-Perot type cavity of high finesse, with a free spectral range (FSR) on the order of $2\pi \times 1$ THz, exceeding the typical linewidths of atomic and cavity resonances (on the order of $2\pi \times 1$ MHz) by 6 orders of magnitude. This ensures that only one longitudinal spatial mode (without loss of generality and in accordance with the experiment, a TEM$_{00}$ mode is chosen) of the cavity is near-resonant to the atomic transition. Modes of a different transverse mode order, e.g. the TEM$_{10}$ or TEM$_{01}$ modes, are detuned by several GHz and thus can also be neglected. With the help of polarization optics, only the circular polarization mode is excited which drives the closed atomic transition. The choice of the circular basis is possible because the cavity used here does not show birefringence and thus does not impose a basis of polarization modes onto the system, as is checked experimentally in appendix A.2. Under these conditions, the Jaynes-Cummings model gives a good approximation of the experiment as long as the system is in the strong-coupling regime, i.e. coupling to the environment can be neglected.

### Jaynes-Cummings Hamiltonian

In the dipole approximation[1] and the rotating-wave approximation (RWA)[2] , the Jaynes-Cummings Hamiltonian for a system of a single atom interacting with a single mode is given by

$$H_{JC} = \hbar\omega_c a^\dagger a + \hbar\omega_a \sigma^\dagger\sigma + \hbar g(a^\dagger\sigma + \sigma^\dagger a) \tag{2.1}$$

This Hamiltonian is intended to describe the evolution of the internal state of the atom and the state of the field. Therefore, the kinetic energy of the atom is not considered and the position is treated as a parameter. $\omega_c$ and $\omega_a$ are the resonance frequencies of the cavity and the atom. $a^\dagger$ and $a$ are the bosonic creation and annihilation operators for photons in the mode, which obey the commutation relation $[a, a^\dagger] = 1$. $\sigma^\dagger = |e\rangle\langle g|$ and $\sigma = |g\rangle\langle e|$ are the rising and lowering operators describing the fermionic two-state atom, which follow the usual pseudo-spin algebra $[\sigma^\dagger, \sigma] = \sigma_z, [\sigma_z, \sigma^\dagger] = 2\sigma^\dagger, [\sigma_z, \sigma] = -2\sigma$ of Pauli matrices, and $\sigma_z = |e\rangle\langle e| - |g\rangle\langle g|$ is the population inversion of the atom. The constant $g$ describes the dipole coupling between atom and field:

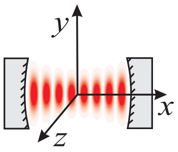

Coordinate system

$$g = g_0\psi(\boldsymbol{r}) \tag{2.2}$$

$$g_0 = \sqrt{\frac{\omega_c}{2\hbar\varepsilon_0 V}}\, d_{ge} \tag{2.3}$$

$$\psi(\boldsymbol{r}) = \cos(kx)e^{-(y^2+z^2)/w_0^2} \tag{2.4}$$

$\psi(\boldsymbol{r})$ is the spatial mode function of the $\mathrm{TEM}_{00}$ resonator mode with the wave number $k = \omega_c/c$ and the waist $w_0$, V is the mode volume (approximately given by $V = \pi w_0^2 L/4$,[3] where $L$ is the length of the resonator), $d_{ge}$ is the dipole matrix element which describes the transition strength between the two atomic states $|g\rangle$ and $|e\rangle$ for the given polarization, and $\varepsilon_0$ is the permittivity of the vacuum.

The dipole interaction term $\hbar g(a^\dagger\sigma + \sigma^\dagger a)$ describes processes where a photon in the mode is annihilated while the atom is excited or vice versa. Therefore this Hamiltonian couples states of the form $|g, n+1\rangle$ and $|e, n\rangle$, where (n+1) is the total

---

[1] The dipole approximation assumes that the size of the atom is much smaller than the wavelength of the electromagnetic field; therefore the amplitude of the field can be considered constant across the dimension of the atom.

[2] The full dipole interaction Hamiltonian is $(a + a^\dagger)g(\sigma + \sigma^\dagger)$. If $|\omega_a - \omega_c| \ll (\omega_a, \omega_c)$, terms of the form $\sigma a$ and $\sigma^\dagger a^\dagger$ with a time evolution of $e^{\pm i(\omega_a+\omega_c)t}$ in the Heisenberg picture average out on the timescale of the evolution of the operators $\sigma a^\dagger$ and $\sigma^\dagger a$, which evolve with $(e^{\pm i(\omega_a-\omega_c)t})$. In the rotating-wave approximation, these terms are neglected.

[3] The beam waist $w$ is assumed to be constant over the length of the resonator ($w \approx w_0$ for $x < L$), which is justified if the Rayleigh length of the mode $x_R = \pi w_0^2/\lambda \gg L$ is much larger than the resonator length ($\lambda = 2\pi c/\omega_c$ is the wavelength of the mode).

number of excitations in the system. The new eigenstates of the system, the *dressed states*, are a linear combination of pairs of these *bare states*:

$$\begin{aligned} |n+1,+\rangle &= \cos\theta\,|e,n\rangle + \sin\theta\,|g,n+1\rangle && (2.5\text{a}) \\ |n+1,-\rangle &= -\sin\theta\,|e,n\rangle + \cos\theta\,|g,n+1\rangle\,, && (2.5\text{b}) \\ n = 0,1,2\ldots & \end{aligned}$$

apart from the singlet ground state $|g,0\rangle$. The mixing angle $\theta$ is a function of the coupling $g$ and the detuning between atom and cavity resonance:

$$\tan\theta = \frac{2g\sqrt{n+1}}{(\omega_a-\omega_c)+\sqrt{4g^2(n+1)+(\omega_a-\omega_c)^2}} \qquad (2.6)$$

The eigenenergies of the system form a ladder of doublets, with a central spacing of one photon energy $\hbar\omega_c$ and a splitting which increases with the square root of $n$ (see Fig. 2.2):

$$E_{(n+1),\pm} = \hbar n\omega_c + \frac{1}{2}\hbar(\omega_a+\omega_c) \pm \frac{1}{2}\hbar\sqrt{4g^2(n+1)+(\omega_a-\omega_c)^2} \qquad (2.7)$$

$$E_{(n+1),+} - E_{(n+1),-} = \hbar\sqrt{4g^2(n+1)+(\omega_a-\omega_c)^2} \qquad (2.8)$$

Spectroscopy of the first doublet of these states in a degenerate system ($\omega_a = \omega_c$) gives a pair of resonances with the splitting $E_{1,+} - E_{1,-} = 2g$, the so-called vacuum-Rabi splitting, which is discussed in section 2.2.1.

The Jaynes-Cummings model can be extended to account for more than one atom in the mode, leading to the Tavis-Cummings model [61]. This model is not considered here.

### 2.1.2 Open quantum system

A prerequisite for spectroscopy on the system is a coupling to the environment, allowing the system to be driven and the observation of photons emitted either through coherent radiation or through incoherent decay processes. Indeed, in the optical regime decay usually cannot be neglected, but plays an integral role in the evolution of the system [62]. The transition from the closed to the open quantum system therefore requires two steps: (a) the inclusion of a pump term in order to drive the system and replenish losses and (b) a coupling to modes other than the privileged cavity mode to describe the decay of the excitation of both atom and cavity mode. Note that the eigenstates of the system will gradually start to deviate from the ones given in the Jaynes-Cummings model as the perturbations of the system through probing and decay increase, and efforts have been made to analytically describe these new eigenstates [63, 64]. However, in the following the perturbations are assumed to be so small that although they cannot be neglected in the evolution of the system, the Jaynes-Cummings model still gives a good approximation of the eigenstates.

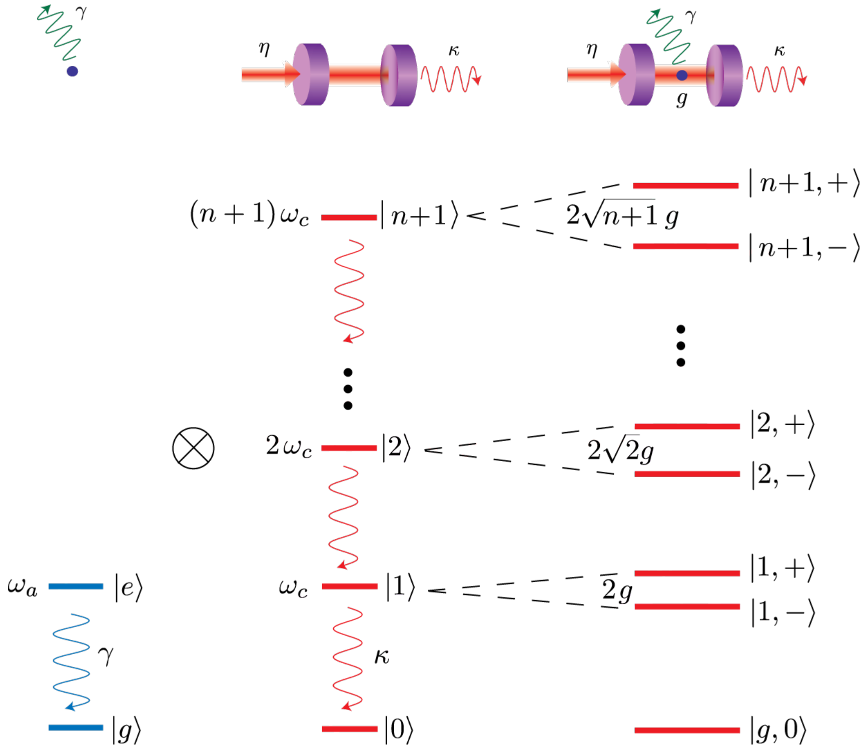

**Figure 2.2: The Jaynes-Cummings model.** This model describes the coupling of a single two-state atom to one mode of the electromagnetic field, represented by a harmonic oscillator with an infinite number of equally spaced levels. The energy levels of the combined system form a ladder of doublets. The splitting between the levels of one doublet increases with the square root of the principal quantum number of the mode $n$, such that the level spacing becomes anharmonic. Losses are not included in the Jaynes-Cummings model, which describes the coherent evolution of a closed quantum system. The decay rates $(\gamma, \kappa)$ of the atomic polarization and the cavity field are introduced in the figure for later reference.

### Pump term

In general, there are two ways to externally excite the system: the atom may be pumped by a laser beam which enters the cavity from the side and the cavity mode can be pumped by a laser beam shining on one of the mirrors. The latter possibility is realized in the experiment, so the description is restricted to this case. Quantum mechanically, the excitation of the cavity mode by a coherent near-resonant field can be described by adding a pump term of the following form to the Jaynes-Cummings Hamiltonian Eq. 2.1:

$$H_{JCP} = H_{JC} + H_P \tag{2.9a}$$
$$H_P = \hbar\eta(a e^{-i\omega_l t} + a^\dagger e^{i\omega_l t}) \tag{2.9b}$$

where $\eta$ is the strength and $\omega_l$ the frequency of the pump field. The spatial mode matching between pump beam and cavity mode is assumed to be perfect and absorption in the cavity mirrors is neglected; these imperfections can be included separately when dealing with a specific experimental situation.

### Master equation

There are several approaches which allow to model the interaction of a system with its environment; an overview can be found in [65]. One way is to derive a master equation, which describes the time evolution of the system density matrix under inclusion of the coupling to the environment. An outline of the derivation of the master equation is given below. A detailed description can be found, e.g., in [66, 67, 68]. The idea is the following:

In principle, system and environment must be considered jointly, and thus are described by a density matrix $\varrho_{tot}$, which includes all degrees of freedom. Mathematically, $\varrho_{tot}$ is composed of vectors from the combined Hilbert space $\mathcal{H}_{tot} = \mathcal{H}_S \bigotimes \mathcal{H}_R$ of system and environment; the environment is the collection of all free-space modes which couple to either the atom or the cavity mode. The time evolution of this density matrix obeys the von-Neumann equation

$$\dot{\varrho}_{tot} = -\frac{i}{\hbar}[H_{tot}, \varrho_{tot}] \tag{2.10}$$

where the total Hamiltonian $H_{tot}$ consists of the Hamiltonians of the subsystems $H_{JCP}, H_R$ and a Hamiltonian $H_{int}$ describing their interaction:

$$H_{tot} = H_{JCP} + H_R + H_{int} \tag{2.11}$$

It is assumed that the interaction term is small and that the environment is not influenced by the system, but essentially remains in a state of thermal equilibrium, which is the vacuum state for modes of optical frequencies. Therefore, the total density operator (in the interaction picture with respect to $H_{int}$) can be written as

$$\varrho_{tot}(t) = \varrho_S(t) \otimes \varrho_R + \mathcal{O}(H_{int}(t)) \tag{2.12}$$

and Eq. 2.10 can be calculated by perturbation theory in the Born approximation, retaining terms up to second order in $H_{int}$.

However, only the time evolution of the density matrix pertaining to the system (labelled $\varrho_S$) is of interest, whereas the environment is simply a reservoir which provides a source of fluctuations and dissipates energy. $\varrho_S$ can be obtained by tracing over the degrees of freedom of the reservoir:

$$\varrho_S = \mathrm{Tr}_R[\varrho_{tot}] \tag{2.13}$$

Note that in this way, the system state is constructed to include a statistical mixture of reservoir states, and thus is no longer expected to be a pure state. The trace over the reservoir can be evaluated using the Markov approximation, which states that the reservoir has a very short 'memory' of its interaction with the system, in the sense that correlations between the system and the reservoir and also correlations within the reservoir itself decay very rapidly as compared to the timescale of evolution of the system density matrix, given by $(g, \gamma, \kappa)^{-1}$. This allows to calculate the derivative $\dot{\varrho}_S = d\varrho_S/dt$ on a timescale $dt$ which averages over these fast fluctuations but is still short compared to the typical time evolution of the system. With these assumptions, the master equation for the density matrix $\varrho_S \equiv \varrho$ reads

$$\begin{aligned}
\dot{\varrho} &= \mathcal{L}\varrho && (2.14a)\\
\mathcal{L}\varrho &\equiv -\frac{i}{\hbar}[H_{JCP}, \varrho] + \kappa\mathcal{L}_a\varrho + \gamma\mathcal{L}_\sigma\varrho && (2.14b)\\
\mathcal{L}_a\varrho &\equiv 2a\varrho a^\dagger - a^\dagger a\varrho - \varrho a^\dagger a && (2.14c)\\
\mathcal{L}_\sigma\varrho &\equiv 2\sigma\varrho\sigma^\dagger - \sigma^\dagger\sigma\varrho - \varrho\sigma^\dagger\sigma && (2.14d)
\end{aligned}$$

Here, the Liouville super operator $\mathcal{L}$ has been introduced; it is a sum consisting of a unitary part (the commutator with the Hamiltonian) which describes the coherent evolution of the closed system and a non-unitary part $\kappa\mathcal{L}_a\varrho + \gamma\mathcal{L}_\sigma\varrho$ which describes the coupling of the mode and the atom to the environment. The coefficients $\kappa$ and $\gamma$ are the decay rates of the cavity field and the atomic polarization, respectively. The master equation can be used to calculate the time evolution of the expectation value of any system operator $\hat{o}$:

$$\langle\dot{\hat{o}}\rangle = \mathrm{Tr}[\hat{o}\dot{\varrho}] = \mathrm{Tr}[\hat{o}(\mathcal{L}\varrho)] \qquad (2.15)$$

An instructive illustration is the calculation of the derivative of the expectation value of the photon number in the mode $\langle a^\dagger a\rangle$ in the case $g = 0$, for which the cyclic property of the trace and the commutation relation $[a, a^\dagger] = 1$ is invoked:

$$\frac{d}{dt}\langle a^\dagger a\rangle = -2\kappa\langle a^\dagger a\rangle \qquad (2.16)$$

In this way, the phenomenologically known decay behavior of the field intensity is recovered.

### Heisenberg equations of motion

The next step is to derive the time evolution of a set of system operators $(a, \sigma, \sigma_z)$ from the master equation. The time evolution is governed by three different characteristic frequencies: the atomic resonance frequency $\omega_a$, the cavity frequency $\omega_c$ and the frequency of the pump (or probe) beam $\omega_l$. In order to reduce the degrees of freedom, we change to the reference frame of the probe beam and define detunings with respect to $\omega_l$. Additionally, complex detunings which also include the decay rates are introduced following ref. [69]:

$$\Delta_a := \omega_l - \omega_a \quad (2.17a) \qquad \tilde{\Delta}_a := \Delta_a + i\gamma \quad (2.18a)$$

$$\Delta_c := \omega_l - \omega_c \quad (2.17b) \qquad \tilde{\Delta}_c := \Delta_c + i\kappa \quad (2.18b)$$

With these definitions, the time evolution of the operators reads:

$$
\begin{aligned}
\langle \dot{a} \rangle &= i(\tilde{\Delta}_c \langle a \rangle - \eta - g \langle \sigma \rangle) &\quad (2.19a)\\
\langle \dot{\sigma} \rangle &= i(\tilde{\Delta}_a \langle \sigma \rangle + g \langle a\sigma_z \rangle) &\quad (2.19b)\\
\langle \dot{\sigma}_z \rangle &= -2\gamma(1 + \langle \sigma_z \rangle) + 2ig(\langle a^\dagger \sigma \rangle - \langle a\sigma^\dagger \rangle) &\quad (2.19c)
\end{aligned}
$$

These are the Heisenberg equations of motion for the operators of interest. The steady state of the system is obtained by setting $(\{\langle \dot{\sigma} \rangle, \langle \dot{a} \rangle, \langle \dot{\sigma}_z \rangle\} = 0)$.

## 2.2 Different cavity-QED models

This section discusses different approaches to solve the Heisenberg equations of motion. An exact analytic solution for these coupled operator equations is not possible, because the set $(a, \sigma, \sigma_z)$ is not complete. This can be seen from Eq. 2.19b, which involves the time evolution of $\langle a\sigma_z \rangle$. However, the equations become analytically solvable in certain limits, leading to different cavity-QED models which help to gain insight into the system from different points of view.

### 2.2.1 Classical model of coupled harmonic oscillators

A simplification of the system which is often justified under experimental conditions is the assumption of low atomic excitation, which is desired to keep the rate of spontaneous emission and thus the heating rate low. Most often this limit is realized by choosing an appropriately low pump intensity, but it can also be reached by adapting the detuning of the pump beam so that the overlap $|\langle e, 0|\alpha\rangle|^2$ of the excited state $|\alpha\rangle = \alpha_+ |1, +\rangle + \alpha_- |1, -\rangle$ with the bare atomic state $|e, 0\rangle$ is small. Mathematically, this limit is reached by setting $\langle a\sigma_z \rangle = -\langle a \rangle$ in Eq. 2.19b (atom always in state $|g\rangle$), and dropping Eq. 2.19c. In this way, a new, closed set of coupled equations is obtained:

$$
\begin{aligned}
\langle \dot{a} \rangle &= i(\tilde{\Delta}_c \langle a \rangle - \eta - g \langle \sigma \rangle) &\quad (2.20a)\\
\langle \dot{\sigma} \rangle &= i(\tilde{\Delta}_a \langle \sigma \rangle - g \langle a \rangle) &\quad (2.20b)
\end{aligned}
$$

For this system, the steady state can be calculated [3]. Following the notation of [69], a new dimensionless complex parameter $\nu$ is introduced in analogy to the cooperativity parameter $C = g^2/2\gamma\kappa$

$$
\nu = \frac{g^2}{\tilde{\Delta}_a \tilde{\Delta}_c} \quad (2.21)
$$

to obtain a concise form of the result:

$$
\begin{aligned}
\langle a \rangle_0 &= \frac{\eta}{\tilde{\Delta}_c} \frac{1}{1 - \nu} &\quad (2.22a)\\
\langle \sigma \rangle_0 &= \frac{\eta\, g}{\tilde{\Delta}_a \tilde{\Delta}_c} \frac{1}{1 - \nu} = \frac{g}{\tilde{\Delta}_a} \langle a \rangle_0 &\quad (2.22b)
\end{aligned}
$$

The steady state intracavity photon number and atomic excitation are given by the modulus square of the last equations (we recall that $\langle \hat{o}^\dagger \rangle = \langle \hat{o} \rangle^*$):

$$\left\langle a^\dagger a \right\rangle_0 = \frac{\eta^2}{|\tilde{\Delta}_c|^2} \frac{1}{|1-\nu|^2} \tag{2.23a}$$

$$\left\langle \sigma^\dagger \sigma \right\rangle_0 = \frac{\eta^2 \, g^2}{|\tilde{\Delta}_a \tilde{\Delta}_c|^2} \frac{1}{|1-\nu|^2} \tag{2.23b}$$

These equations are sufficient to calculate a spectrum of the system, which shows two resonances, the normal-mode resonances. They are characterized by the eigenfrequencies $\omega_\pm$, which can be obtained from Eqns. 2.20:

$$\omega_\pm - \omega_l = -\frac{1}{2}(\tilde{\Delta}_a + \tilde{\Delta}_c) \pm \frac{1}{2}\sqrt{4g^2 + (\tilde{\Delta}_a - \tilde{\Delta}_c)^2}, \tag{2.24}$$

These frequencies $\omega_\pm$ have complex values. The real part $\mathrm{Re}\,(\omega_\pm)$ determines the position of the resonances; the imaginary part $\mathrm{Im}(\omega_\pm)$ describes their widths.

In Fig. 2.3(a), the position of the normal modes is indicated in a 2D-parameter plot as a function of the detunings $(\Delta_a, \Delta_c)$. Spectra which show the response of the intracavity photon number (proportional to the signal of a detector in transmission of the cavity) to a scan of the probe frequency for the degenerate case $\Delta_a = \Delta_c$ and two non-degenerate cases $\Delta_c \lessgtr \Delta_a$ are presented in Fig 2.3(b). For $\Delta_a = \Delta_c$, the amplitudes of both resonances are equal and the distance between the resonances reaches its minimum value $\omega_+ - \omega_- \approx 2g$. If atom and cavity are detuned, the overlap $|\langle g, 1|1, +/-\rangle|^2$ of one of the dressed states with the bare cavity state $|g, 1\rangle$ increases, leading to a better visibility of this 'cavity-like' peak since only the bare cavity state is pumped as well as observed; in addition, the distance between the resonances increases. Since effects of saturation are neglected in this low-excitation limit, the obtained spectra are linear in the probe power ($P_{pump} \propto \eta^2$).

Considering the widths of the resonances ($\Gamma_{\mathrm{HWHM}} = (\gamma + \kappa)/2$ in the degenerate case), it is clear that they can only be resolved in the strong-coupling regime, with $g \gg (\gamma, \kappa)$. Here, the influence of the decay on the position of the resonances can be neglected, and the resonance frequencies match the first pair of dressed states in the Jaynes-Cummings ladder (cp. Eq. 2.7). Therefore, this approximation is equivalent to truncating the Jaynes-Cummings ladder after the first doublet and restricting the maximal number of excitations in the system to 1 (see Fig. 2.4). Higher energy levels are explicitly excluded.

### Classical interpretation of the normal mode spectrum

The phenomenon that the originally degenerate resonances of bare atom and cavity (for $\omega_a = \omega_c$) split into two new resonances in the coupled system is called normal-mode or vacuum-Rabi splitting. It has been observed in many atom experiments, with atomic beams passing a cavity [15, 16, 17], atoms trapped inside cavities [18, 19, 20], and recently with Bose-Einstein condensates inside cavities [70, 71]. The normal-mode splitting has also been seen in cavity QED systems outside atomic

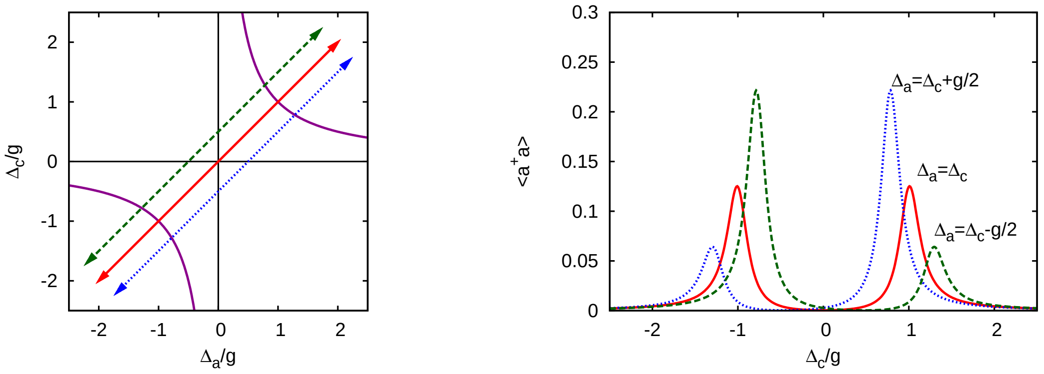
(a) Location of normal-mode resonances

(b) Normal-mode spectra

**Figure 2.3: Normal-mode spectra. (a)** The normal modes form an avoided crossing between the resonances of the bare atom and the bare cavity (curves), with the minimal splitting of $2g$ occurring for the symmetric case $\Delta_a = \Delta_c$. In **(b)**, spectra along different scan directions (as indicated in (a)) are shown. Due to the experimental configuration of pumping and detecting losses from the cavity mode, the amplitudes of the normal-mode resonances differ if $\Delta_a \neq \Delta_c$. The parameters are $(\gamma, \kappa) = 0.1g, \eta^2 = \kappa^2$.

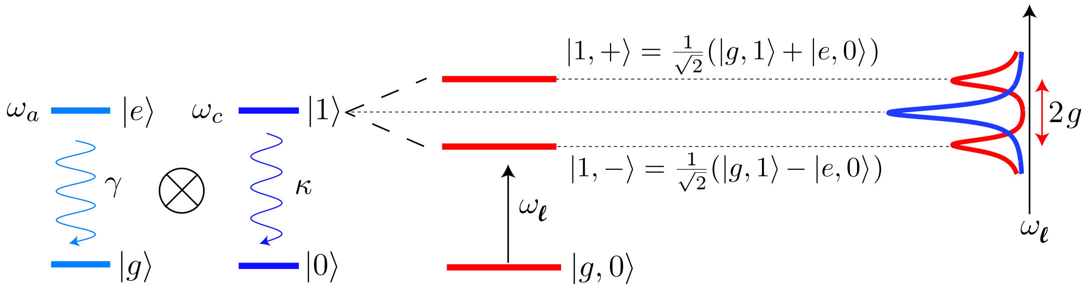

**Figure 2.4: Normal-mode splitting.** When atom and cavity are coupled, the Lorentzian-shaped transmission spectrum of the cavity resonance splits into two new resonances, the normal modes. This splitting is already predicted in the low-saturation limit and is reminiscent of the normal-mode spectrum of two coupled classical harmonic oscillators. The structure of the system is equivalent to truncating the Jaynes-Cummings ladder after the first doublet of dressed states.

physics, with quantum dots coupled to micropillars [72, 73] or microdiscs [74] or placed inside photonic crystals [75], and also with Josephson junctions as artificial atoms which were coupled to microcircuits [76]. In fact, observation of the normal-mode splitting is a benchmark signature that a system has reached the strong-coupling regime of cavity QED.

However, this splitting is no pure quantum effect; it can as well be explained classically. This is already implicit in the form of Eqns. 2.20, which are the low-intensity limit of the Heisenberg equations of motion. When replacing the expectation values of the operators by classical amplitudes, these equations describe a set of coupled, damped harmonic oscillators, which can be interpreted as the atomic dipole (amplitude governed by $\sigma$) and the single-mode field inside the cavity (amplitude governed by $a$) [3]. The two observed resonances are equivalent to those obtained from this classical picture, also explaining the terminology of 'normal modes'. However, this analogy only holds as far as mean values are concerned; correlations of the operators are lost in this picture. Quantum mechanically, the interpretation of the atom as a harmonic oscillator becomes obvious from the initial approximation $\langle a\sigma_z\rangle \rightarrow -\langle a\rangle$, which is also satisfied when $\sigma_z = [\sigma, \sigma^\dagger] \rightarrow -1$. This changes the fermionic commutator relation to the bosonic one, setting atom and light field on the same footing. A different classical explanation of the normal-mode splitting was presented by Zhu et al. [14], who derive this spectrum from linear dispersion theory. Here, the normal-mode resonances are a consequence of the phase shift picked up by the light beam on a round trip in the resonator. This phase shift depends on both the cavity length and the refractive index caused by the presence of the atom and vanishes on the normal-mode frequencies, leading to constructive interference.

### 2.2.2 Semiclassical nonlinear optical bistability theory

The classical limit described in the previous section treats both atom and field as linear harmonic oscillators, omitting effects of saturation. Obviously, this approximation breaks down for stronger driving, when the substitution $\sigma_z \rightarrow -1$ no longer holds. In this case, a different approximation can be made which respects the quantized nature of the two-state atom: only the field is treated classically by assuming that the operator $a$ can be replaced by a complex number $\langle a\rangle$. With this approximation, the Heisenberg equations of motion (2.19) become:

$$\begin{aligned}
\langle\dot{\sigma}\rangle &= i(\tilde{\Delta}_a \langle\sigma\rangle + g\langle a\rangle\langle\sigma_z\rangle) && \text{(2.25a)}\\
\langle\dot{a}\rangle &= i(\tilde{\Delta}_c \langle a\rangle - \eta - g\langle\sigma\rangle) && \text{(2.25b)}\\
\langle\dot{\sigma}_z\rangle &= -2\gamma(1+\langle\sigma_z\rangle) + 2ig(\langle a^\dagger\rangle\langle\sigma\rangle - \langle a\rangle\langle\sigma^\dagger\rangle) && \text{(2.25c)}
\end{aligned}$$

This set of equations is equivalent to the single-atom limit of the Maxwell-Bloch equations, which are used to describe the interaction of a sample of two-state atoms with a coherent light field. The steady state of this system can be solved analytically. To this end, the saturation parameter $s_0$ is defined:

$$\langle\sigma_z\rangle_0 \equiv -\frac{1}{1+s_0} \tag{2.26}$$

Notice that $s_0 \rightarrow 0$ in the low saturation limit. With these definitions, a new coupled set of equations is derived:

$$\begin{aligned}
\langle a\rangle_0 &= \frac{\eta}{\tilde{\Delta}_c}\left[1 - \frac{\nu}{1+s_0}\right]^{-1} && \text{(2.27a)}\\
s_0 &= \frac{2g}{|\tilde{\Delta}_a|^2}|\langle a\rangle_0|^2 && \text{(2.27b)}
\end{aligned}$$

This set of equations can be combined to a cubic equation for $\langle a\rangle_0$, leading to three solutions. For one class of input parameters, two of these solutions are complex and

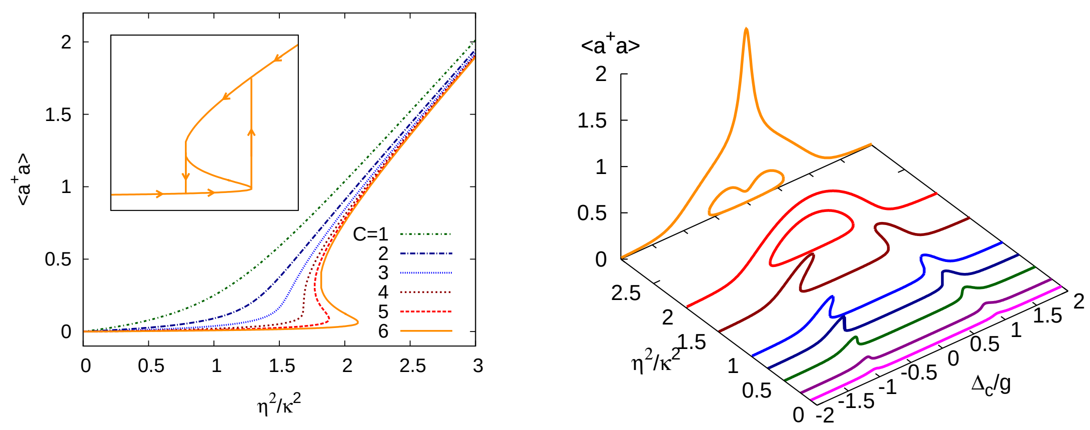
(a) Intensity dependence and hysteresis (b) Spectra for different intensities

**Figure 2.5: Optical bistability.** In this model, only the atom is quantized (allowing for saturation effects) while the electric field is described by the classical Maxwell equations. **(a)** Depending on the cooperativity parameter C, more than one stable solution for the intensity of the intracavity light field is possible and the system can show hysteresis upon a change of the pump intensity (inset). Parameters: $\Delta_a = \Delta_c = 0$. **(b)** Spectra calculated at different pump intensities show that the normal mode structure is recovered for small pumping. Bistability occurs only at higher intensities, where the peaks bend and finally meet to form a closed structure. Parameters: $\kappa = \gamma = 0.1g$ $(C = 50)$.

therefore not physically relevant. However, in certain regimes all three solutions have real values, and consequently the steady state of the system is multivalued. In this regime, the amplitude of the intracavity field can switch between two values (the third solution is unstable), which is why this limit is called optical bistability theory and the equation for $|\langle a\rangle_0|^2$ (Eq. 2.27) is called the bistability state equation [22]. In Fig. 2.5, the functional dependence between the pump strength and the intracavity photon number is plotted for different cooperativity parameters $C = g^2/2\gamma\kappa$. While for small $C$ the solution stays unique, for $C > 4$ the typical s-shaped curve indicates that two stable solutions are possible. Thus the system can show hysteresis, with the observed transmission depending on its own history. In any case, the theory of bistability predicts a nonlinear relation between input and output intensity. The low-intensity limit (Eq. 2.23a) discussed in the previous section is formally recovered if one sets $s_0 = 0$.

### Optical bistability for atomic ensembles and on the single atom level

The system for which optical bistability is traditionally known consists of a nonlinear (saturable or with intensity-dependent dispersion) medium inside a resonator. The first experimental observations of optical bistability succeeded with vapors [77]; in the meantime, this effect has also been established with several cold atoms passing through or stored in a cavity [28, 17, 78]. However, at the level of single atoms measurements suggest disagreement with the prediction of optical bistability [55].

The theory of OB is a mean-field theory in the sense that quantum fluctuations of the field are neglected. If these fluctuations are significant, they should prevent the system from settling into one of two possible steady states and thus destroy bistability [79, 80]. Therefore such an effect is not expected for a single atom inside the cavity as long as the number of photons in the mode is small, even if the atom is saturated.

### 2.2.3 Quantum model

In the two cavity-QED models discussed so far, the field is treated classically. Field quantization becomes important in an atom-cavity system which is characterized by a small saturation photon number[4] $n_s \lesssim 1$, i.e. where the presence or absence of a single photon in the mode has a large influence on the dynamics of the system. To include field quantization, the term $\langle a\sigma_z\rangle$ in Eqns. 2.19 has to be retained, precluding an analytical solution. For a numerical solution, a finite set of basis vectors has to be chosen from the combined Hilbert space of the system $\mathcal{H}_s = \mathcal{H}_a \otimes \mathcal{H}_c = \{\{|g,i\rangle, |e,i\rangle\}, i \in \mathbb{N}_0\}$, where $\mathcal{H}_a = \{|g\rangle, |e\rangle\}$ is the two-dimensional Hilbert space of the atomic states and $\mathcal{H}_c = \{|i\rangle, i \in \mathbb{N}_0\}$ is the Hilbert space of the mode, expressed in the infinite basis of Fock states. High Fock states will not be occupied at moderate pump intensities, therefore this basis can be truncated for numerical calculations. One method which helps to ensure convergence of the steady state even at a lower number of basis vectors, which is essential due to limited computational power, is the introduction of a referred state following the procedure in [69]. The referred state is chosen here to be the steady state $\varrho_\alpha$ of the system in the low saturation limit. The basis of Fock states is then displaced by shifting the field operator $a$ by its position-dependent low-saturation expectation value $\alpha(\boldsymbol{r}) = \mathrm{Tr}[a\varrho_\alpha] = \langle a\rangle_0$ (Eq. 2.22a). This defines the new field operator $c$:

$$c = a - \alpha(\boldsymbol{r})\mathbb{I} \tag{2.28}$$

where $\mathbb{I}$ is the identity matrix. The vacuum state of $c$ then corresponds to a coherent state $\alpha(\boldsymbol{r})$:

$$0 = c\,|0\rangle_c = (a - \alpha(\boldsymbol{r}))\,|0\rangle_c \rightarrow a\,|0\rangle_c = \alpha(\boldsymbol{r})\,|0\rangle_c \tag{2.29}$$

This is why states which do not deviate too far from the low-saturation limit converge faster in the displaced basis.

The master equation 2.14 then reads

$$\begin{aligned} \dot{\varrho} &= -\frac{i}{\hbar}[H_c, \varrho] + \kappa\mathcal{L}_c\varrho + \gamma\mathcal{L}_\sigma\varrho && \text{(2.30a)}\\ \mathcal{L}_c\varrho &\equiv 2c\varrho c^\dagger - c^\dagger c\varrho - \varrho c^\dagger c && \text{(2.30b)}\\ \mathcal{L}_\sigma\varrho &\equiv 2\sigma\varrho\sigma^\dagger - \sigma^\dagger\sigma\varrho - \varrho\sigma^\dagger\sigma && \text{(2.30c)} \end{aligned}$$

with the shifted Hamiltonian $H_c$ ($\alpha \equiv \alpha(\boldsymbol{r})$ implicit)

$$\begin{aligned} H_c = &-\Delta_a\sigma^\dagger\sigma - g\alpha\sigma^\dagger - g\alpha^*\sigma + g(c^\dagger\sigma + c\sigma^\dagger)\\ &-\Delta_c c^\dagger c + (\eta + \tilde{\Delta}_c\alpha)c^\dagger + (\eta + \tilde{\Delta}_c^*\alpha^*)c \end{aligned} \tag{2.31}$$

---

[4] The saturation photon number is defined as $n_s = \frac{\gamma^2}{2g^2}$

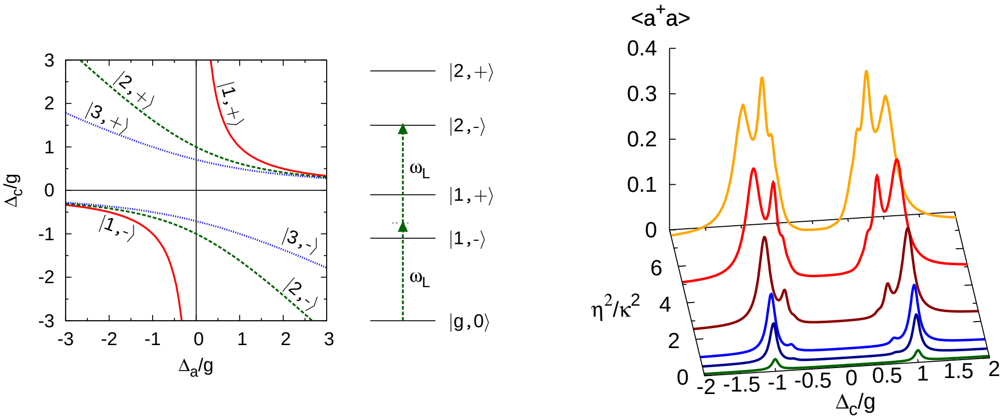
(a) Location of multiphoton resonances

(b) Spectra for different intensities

**Figure 2.6: Quantum theory.** This model retains the quantization of the light field, reproducing higher doublets from the Jaynes-Cummings ladder which can be accessed by simultaneously absorbing more than one photon from the pump field. Such a two-photon transition to the state $|2,-\rangle$ is indicated in **(a)**, together with the location of the resonances from the first three doublets in the $(\Delta_a,\Delta_c)$-plane. In **(b)**, spectra for different pump powers are shown. At low powers, the normal-mode spectrum is recovered; the additional resonances appear only at higher pump powers. Parameters: $\gamma = \kappa = 0.05g$. For the calculation, the basis was truncated at $|n_{fock}\rangle = |10\rangle$.

Expectation values of operators can then be calculated numerically using standard methods (for details, see appendix A.1).

In Fig. 2.6, the steady state expectation value of the intracavity photon number $\langle a^\dagger a\rangle = \mathrm{Tr}[a^\dagger a \varrho_0]$ is shown as a function of the probe detuning $(\Delta_a = \Delta_c)$ for different input intensities. In the low-intensity limit, the spectrum matches the spectra obtained from the previous models, showing the normal-mode splitting. As the pump strength is increased, additional resonances start growing on the inside slopes of the normal modes. In terms of the Jaynes-Cummings picture, these resonances can be interpreted as multiphoton transitions to higher-lying doublets $(E_{(n+1),\pm})$. Their location is determined by the resonance condition

$$(n+1)\hbar\omega_l = E_{n+1,\pm} \tag{2.32}$$

where $E_{n+1,\pm}$ are the energy levels of the Jaynes-Cummings ladder. In Fig. 2.6(a), the resonance condition for multiphoton transitions of different order is indicated in the $(\Delta_a,\Delta_c)$-plane. The higher-lying states have no classical interpretation, their existence is a direct consequence of field quantization.

### 2.2.4 Remarks on the essential differences between the models

In the low-saturation limit, the classical, semiclassical and the quantum model coincide in their description of the system: all three equally predict the normal-mode splitting, which occurs at arbitrarily low intensities. As the atomic excitation is increased, the three models start to deviate. The classical model fails to describe the system as saturation effects are neglected. These are considered in the semiclassical theory, where the atom is quantized. Deviations between the semiclassical and quantum theory arise in parameter regimes with low saturation photon numbers, and can already be significant at rather low, though non-vanishing excitation probability of the atom.

# Chapter 3

# Investigating the structure of the atom-cavity system

There is a variety of experimental approaches to determine the structure of the coupled atom-cavity system. In microwave experiments, the quantization of the system can be observed via Rabi oscillations in the time domain. In the optical domain, indirect evidence of the higher dressed states can be found in the photon statistics of the transmitted light field, and there are also cavity-QED systems outside atomic physics which are governed by the same Hamiltonian and thus suited for similar studies. These experiments are reviewed in the first part of this chapter. The second part concentrates on possibilities to observe the higher-lying states in the spectrum of an optical cavity-QED experiment. Different methods to resolve such a resonance under the given experimental boundary conditions are introduced, and the inherent nonlinearity of the resonance is discussed.

## 3.1 Evidence of higher states in previous experiments

### 3.1.1 Microwave experiments

With the advent of the one-atom maser in 1985 [5], it became possible to study the energy exchange between a single atom and a single mode in the microwave domain: When an atom in the excited state enters the mode, its excitation is coherently exchanged with the field, and the probability of finding the atom in the excited state after its exit from the resonator becomes an oscillatory function of its transit time. If atom and cavity are on resonance, the rate of oscillation is given by the single-atom Rabi frequency $\Omega = 2g\sqrt{n+1}$, where $2g$ is the vacuum Rabi frequency and $n$ is the number of photons in the resonator field. When exciting the mode, the intracavity field possesses a probability distribution over discrete photon numbers, therefore the Rabi oscillations will collapse and revive after a time characteristic to this distribution due to constructive or destructive interference of the Rabi nutations of different frequencies. This effect was first observed in 1987 [10]. In a conceptually similar, but more refined experiment in 1996 [11], a Fourier transform of the time-dependent excitation probability even revealed discrete resonances with a characteristic decrease in distance proportional to $\sqrt{n}-\sqrt{n-1}$ which is associated with the occupation of dressed states in several consecutive doublets.

A similar signature of the quantized states was obtained in a very different system, a trapped ion which was cooled almost to the motional ground state. The coupling between the internal state of the atom and its quantized motion states is governed by the same Jaynes-Cummings Hamiltonian used for the atom-cavity system, and consequently the number state distribution of the motion couples in the same way to the evolution of the internal atomic state [81].

In the dispersive regime of large detuning between atom and cavity resonance, the dressed states separate into products of bare states, and each cavity photon linearly changes the transition energy of the atom by a characteristic ac Stark shift. In this regime, a non-destructive count of the number of photons in the resonator was recently accomplished by real-time observation of the collapse of the wavefunction of the field [82], representing maybe one of the most beautiful proofs of field quantization in a regime where atom and field are mostly decoupled. Consequently, the quantization of the electromagnetic field and the validity of the Jaynes-Cummings model are well documented by cavity QED experiments in the microwave domain [8].

### 3.1.2 Optical correlation experiments

In the visible regime, not only the coupling but also the decoherence rates of both the atomic polarization and the cavity field are much higher than in microwave experiments, therefore a similar state detection of the atom is not practicable. Instead, the photons escaping from the cavity can be used for an indirect observation of the coherent evolution of the system in a photon correlation measurement. The idea, as developed for multiple atoms in the cavity, is the following [83]: We start by assuming that the atom-cavity system has evolved into its steady (pure) state, sharing excitation between the atoms and the mode. Detecting a photon emitted from the cavity projects the quantum-mechanical wavefunction of the system to a non-equilibrium state with one less excitation in the mode. The system evolves back to its steady state on the timescale given by the inverse Rabi frequency; only after this time has the probability of emitting a photon from the mode reached its initial value. Therefore, the second-order correlation function

$$g^2(\tau) = \frac{\langle p(t)p(t+\tau)\rangle}{\langle p(t)\rangle^2} \tag{3.1}$$

which gives the conditioned probability of measuring a photon at time $(t+\tau)$ after detecting a first photon at time $t$, normalized on the probability of detecting two independent photons, shows oscillations on this timescale. This effect has been seen in different experiments with atomic beams crossing an optical high-finesse resonator [28, 29, 30]. In general, measuring the intensity correlation is a possibility to distinguish between classical and non-classical fields. In classical physics, the fluctuations of the field are described by stochastic probabilities, leading to restrictions in the correlation function due to the Schwartz inequalities [80]: $g^{(2)}(0) > g^{(2)}(\tau)$ and $|g^{(2)}(0) - 1| > |g^{(2)}(\tau) - 1|$. These inequalities state at first that for classical fields the correlation function must assume its absolute maximum at time 0, a requirement which prohibits anti-bunching $g^{(2)}(0) < 1$, as $g^{(2)}(\infty) = 1$ is the limit assumed for infinite time when all correlations have decayed. Second, the largest deviation from this limit must also appear at time $\tau = 0$. Quantum physics provides a way of violating these inequalities as probabilities must be replaced by amplitudes which can interfere. Indeed, the afore-mentioned experiments reported non-classical correlations, proving the quantum nature of the transmitted field.

Considering a single atom inside a high-finesse resonator, a non-classical feature in the correlation function is intuitively accessible when having in mind the energy spectrum given by the Jaynes-Cummings model: The transmitted light is anti-bunched if the system is probed on one of the normal-mode resonances. Due to the anharmonic splitting of the doublets, the photon energy required to drive a transition from the ground state to the first doublet differs from the one needed to drive a transition from the first to the second doublet (see Fig. 2.2). Therefore, once the system is excited to the first doublet, no other photon of the same frequency can enter the cavity as long as the first excitation has not decayed. The resulting anti-bunching was observed for a single Cs atom [31] trapped inside a high-finesse resonator, for an atom passing a microdisk resonator [84] and for a quantum dot placed inside a photonic crystal cavity [85].

### 3.1.3 Cavity-QED systems outside atomic physics

In recent years, cavity-QED systems outside atomic physics have undergone a rapid development. In these systems, the two-level atom is replaced by an 'artificial atom' made of a microscopic structure in a solid-state device which is integrated into a cavity. Such systems promise easier manageability and scalability than classical atom or ion traps, which is essential for applications in the field of quantum computation [86]. Several of these systems have already shown normal-mode splitting, and are now suited to investigate the strong-coupling regime competitively to the traditional atom-cavity experiments. In the following, two groups of such systems are introduced.

#### Superconducting circuits

One modern field of cavity QED is circuit QED [86], which employs superconducting circuits on chips to implement strong coupling. Charge ('Cooper pair box') or flux qubits consisting of Josephson junctions pose as artificial atoms, emitting in the microwave regime. Such a qubit can be coupled to superconducting LC circuits in the form of SQUIDs or transmission line resonators printed on the chip, in which a microwave photon manifests itself as electric current. In the near-resonant regime, these systems have shown normal-mode splitting in the spectrum [76, 87, 88] and in the time domain [89], where moreover signatures of distinct interfering Rabi oscillations from higher dressed states [90] were found in a manner similar to refs. [11, 81]. In another experiment in the dispersive regime, the intensity-dependent ac Stark shift was used in order to spectrally resolve the photon-number distribution of coherent and thermal pump fields [91]. Spectroscopic observation of the quantized light-matter states in the near-degenerate case, where the contributions of atom and cavity are non-separable, has so far not been reported.

#### Quantum dot systems

Cavity QED with semiconductor structures has also progressed quickly [26]. Here, a quantum dot [92] with a resonance at optical frequencies is used as artificial atom. The quantum dot can be combined with different kinds of optical microcavities [93]. The most important ones having already reached the strong-coupling regime are micropillars consisting of two opposing Bragg reflectors [72], microdisks which rely on total internal reflection to sustain whispering gallery modes [74, 94], and photonic crystal slabs which consist of a periodic structure of holes with a defect to confine light [75, 95, 96]. In these systems, the search for two-photon nonlinearities is a major goal as well [26, 27].

## 3.2 Spectroscopy of higher levels in optical cavity QED

While there is evidence for the existence of the higher doublets of the Jaynes-Cummings ladder from previous cavity-QED experiments, these experiments operate in a regime where cumulative effects from the presence of several different energy levels are observed. This section provides the theoretical background needed to devise an experiment which allows direct excitation and spectroscopic detection of a two-photon state. The signature of this state in the spectra is addressed under consideration of the parameters and limitations provided by the given atom-cavity apparatus (see section 5).

### 3.2.1 Monochromatic spectroscopy

The idea of resolving the higher-order states in optical spectroscopy has been discussed in literature for several years [3, 23, 24]. In general, one can distinguish between two possible approaches to excite a higher doublet: The first one is the bi-chromatic (step-wise) excitation, which starts with the resonant excitation of one of the normal-modes using one frequency, and continues from there to excite a state of the next doublet by using light with a second frequency. This idea has been experimentally approached in a system with an atom beam [56], which failed mostly due to large atom-number fluctuations, and also in a previous measurement with a single trapped atom in this experiment, where the measurement result was not conclusive owing to lack of signal to noise ratio [97, 98]. Here, the second approach is chosen: monochromatic excitation, i.e. a direct excitation of a higher state via a virtual level, using two photons of the same frequency as illustrated in Fig. 2.6(a). This approach has several advantages: for one, a higher doublet state can be populated without inadvertently probing also one of the normal-mode states, such that this background can be minimized and an exclusive excitation of the desired final state becomes feasible; for another, monochromatic excitation comes along with a nonlinear dependence of the higher state population on the probe intensity. While the intensity-dependence is discussed in more detail in section 3.2.2, the next paragraph concentrates on the unique addressability of the higher states.

### Anharmonicity of the spectrum

In order to drive a multiphoton transition, the resonance condition (Eq. 2.32) has to be met. Written in terms of detunings, the resonance condition for the excitation of the $(n+1)$th doublet reads

$$(n+1)\Delta_c = \frac{1}{2}(\Delta_c - \Delta_a) \pm \frac{1}{2}\sqrt{4g^2(n+1) + (\Delta_a - \Delta_c)^2} \tag{3.2}$$

In the degenerate case $\Delta_a = \Delta_c$, this equation reduces to

$$\Delta_c = \pm \frac{g}{\sqrt{(n+1)}} \tag{3.3}$$

This equation shows that the level spacing is anharmonic, i.e. that a light field of a given frequency can resonantly excite at most one eigenstate of the system even if multiphoton transitions are considered, as long as $n$ is small. In the limit $n \to \infty$, the resonance frequency tends towards $\Delta_c = 0$, and consequently the anharmonicity of the level structure is lost in this semiclassical limit. Therefore, a separate resolution of these states is most promising if the number of excitations in the system is kept low, and best resolution is obtained for the first and second doublet $|\pm,1\rangle, |\pm,2\rangle$, where the difference in the detunings reaches its maximum of $\pm(1 - 1/\sqrt{2})g$. In order to resolve these resonances in a spectrum, the coupling constant $g$ obviously must by far exceed the linewidths of the resonances, given by a combination of $(\gamma, \kappa)$; therefore the system must be situated deeply in the strong coupling regime. The parameters given by the measurement setup (see chapter 5) are $(g_0, \gamma, \kappa) = 2\pi(16, 3, 1.25)$ MHz, and the effective coupling $g$ is reduced by a factor of about 0.7 due to non-ideal localization of the atom in the cavity mode. Using these parameters, the spectrum of the atom-cavity system for the degenerate case is depicted in Fig. 3.1(a). It is obvious that the coupling is not large enough to separate the single- from the two-photon resonance.

However, by leaving the degenerate case and introducing a detuning between the bare atom and cavity resonance frequencies, it is possible to increase the distance between resonance frequencies for the lower dressed states of consecutive doublets, while the distance for the upper states is reduced. This is illustrated in the two upper panels of Fig. 3.1, where the positions of the resonances in a spectrum are indicated by the intersection of the straight arrow, which depicts the probe frequency

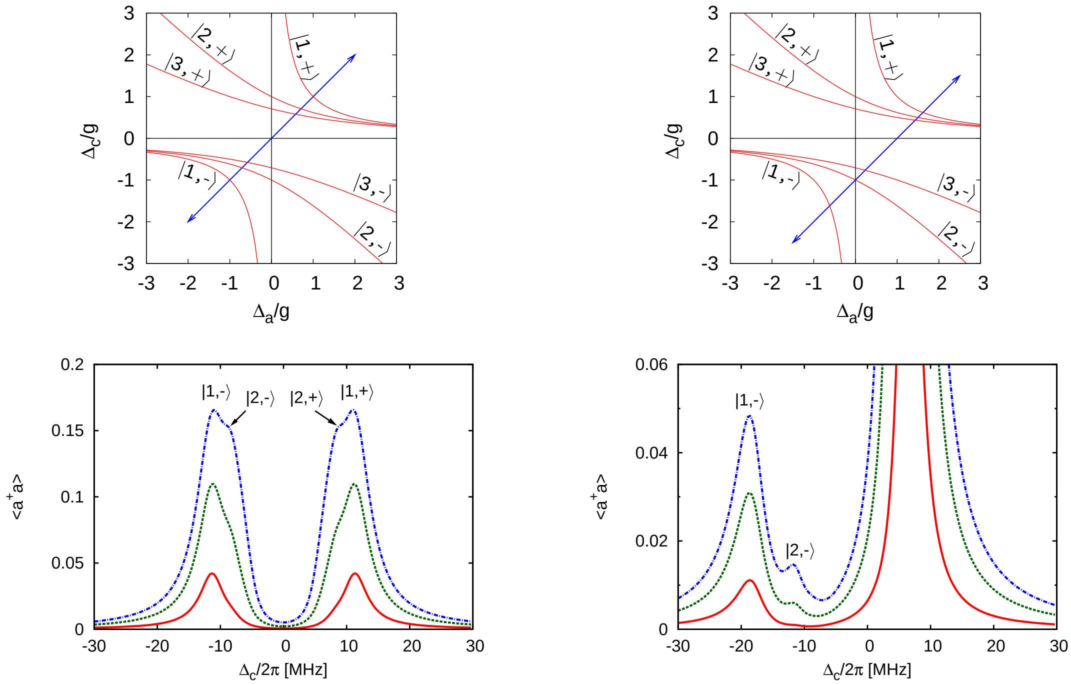
(a) Symmetric diagonal spectra

(b) Asymmetric diagonal spectra

**Figure 3.1: Quantum spectra.** Scanning the laser frequency, the quantum model predicts resonances stemming from multiphoton transitions in addition and close to the normal-mode resonances. These additional resonances appear only at higher intensities. For the parameters of the system $(g, \gamma, \kappa) = 2\pi(0.7 \cdot 16, 3, 1.25)$ MHz, these resonances cannot be separately resolved in a symmetric spectrum $(\Delta_a = \Delta_c)$ **(a)**, but only in an asymmetric spectrum (here: $\Delta_a = \Delta_c + g$), where the two-photon transition appears as a separate peak at $\Delta_c \approx -2\pi \times 11$ MHz **(b)**. The pump power for the consecutive spectra is $\eta^2 = (0.5, 1.5, 2.5)\kappa^2$.

scan, with the different curves indicating the resonance conditions for the different doublets in the $(\Delta_a,\Delta_c)$-plane. Fig. 3.1(b) displays a scan calculated for $\Delta_a - \Delta_c = g$, a parameter set which allows to separate the resonances $|1,-\rangle$ and $|2,-\rangle$. Observing these two resonances at the predicted positions would confirm that the system is correctly described by the anharmonic ladder structure of the Jaynes-Cummings model.

### Selective excitation of the quantum resonances

A disadvantage of these spectra is that the classical normal-mode resonances are the most prominent ones for pump intensities which are experimentally reasonable; the purely quantum multiphoton resonances appear small in comparison. In order to circumvent this problem, a new scanning technique is proposed here which allows to concentrate purely on the quantum part of the spectrum. This technique is based on the observation that the resonance condition (Eq. 3.2) for the first doublet $n = 0$ cannot be fulfilled for any detuning $\Delta_c$ as long as the probe frequency is equal to the bare atom frequency, i.e. $\Delta_a = 0$, whereas it can be fulfilled for all

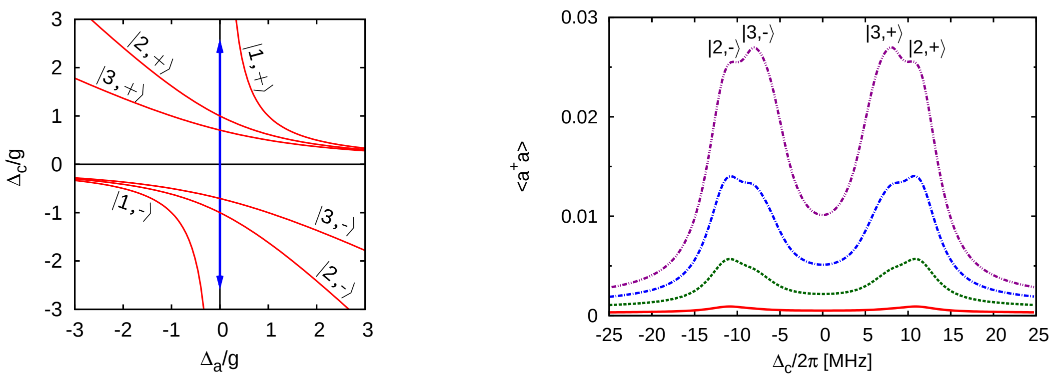
(a) Vertical scan idea

(b) Vertical spectra

**Figure 3.2: Quantum spectra for vertical scan direction.** **(a)** By scanning vertically along ($\Delta_a = 0$), the normal-mode resonances can be avoided and only the multiphoton resonances are visible. **(b)** The lowest-order resonance which appears is a two-photon resonance, whereas a contribution from three-photon transitions leads to a double-peak structure at higher scan intensities. The pump power is $\eta^2 = (0.5, 1.5, 2.5, 3.5)\kappa^2$ for the consecutive spectra. For other parameters, see Fig. 3.1.

higher doublets ($n \geq 1$). This break in symmetry arises from the fact that the atom is a two-state particle whereas the light field has an infinite number of states, a property which becomes important as soon as Fock states beyond the first pair are occupied. This structural property of the system can be exploited to avoid crossing the normal modes by performing a scan along the direction $\Delta_a = 0$, as illustrated in Fig. 3.2. Technically, this scan direction can be realized by varying the cavity frequency instead of the probe frequency: $\omega_l = \omega_a = \text{const}, \omega_c = \text{variable}$. For these parameters, resonances of the higher doublets will occur at

$$\Delta_c = \pm \frac{g}{\sqrt{n}}, n \geq 1 \tag{3.4}$$

The spectrum for different probe intensities is depicted in Fig. 3.2(b). The two visible resonances stem from the excitation of the states $|2, \pm\rangle$ and $|3, \pm\rangle$; the normal modes do not produce a resonance, but only a background stemming from off-resonant excitation due to their finite linewidths. This is illustrated in Fig. 3.3, where two of the symmetric spectra introduced in Fig. 3.2(b) are approximated by curves which describe the contributions of the different transition orders. The contribution of the single-photon transitions is calculated in the classical limit presented in section 2.2.1, without the use of fit parameters. The contribution of the higher photon transitions is modeled by Lorentzian curves with a position and width given by the real and imaginary part of the solution of Eq. 3.2, when replacing $(\Delta_a, \Delta_c) \rightarrow (\tilde{\Delta}_a, \tilde{\Delta}_c)$ and solving for ($\Delta_a = 0$); the amplitude of these Lorentzians is fitted. This ansatz reproduces the spectra calculated from the numerical solution of the master equation reasonably well for not too high input intensities, except for the region around $\Delta_c = 0$, where higher transition orders would already have to be taken into account. It shows that the single-photon contribution gives a broad, slightly curved background which approximates the quantum spectrum only in the limit of

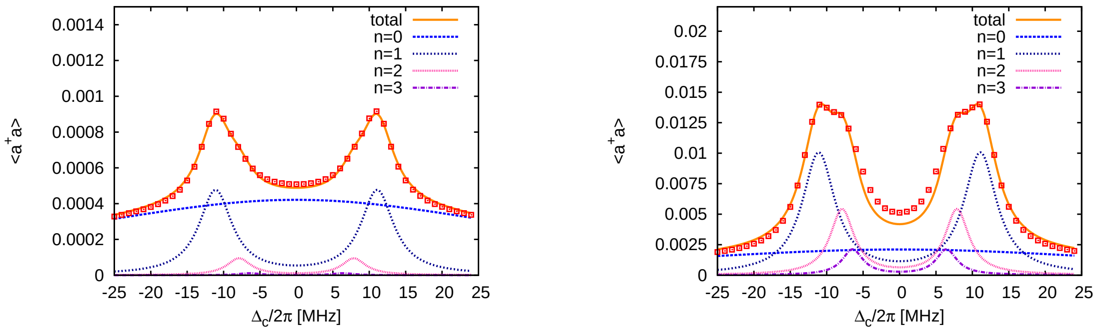

(a) Pump power $\eta^2 = 0.5\kappa^2$

(b) Pump power $\eta^2 = 2.5\kappa^2$

**Figure 3.3: Line shapes of vertical spectra.** The spectra calculated by numerically solving the master equation (points) for two different pump powers are approximated by a sum (solid line) of different contributions: a background from single-photon off-resonant transitions calculated with the classical model (Eq. 2.23a ) ($n = 0$), and Lorentzian transmission curves with the peak positions and linewidths obtained from Eq. 3.2 for complex detunings $(\tilde{\Delta}_a, \tilde{\Delta}_c)$. Three Lorentzian curves for the two-photon ($n = 1$), the three-photon ($n = 2$) and the four-photon ($n = 3$) transitions were considered. Their amplitudes are fitted in the region $-2\pi \times 25$ MHz to $-2\pi \times 7$ MHz. This model reproduces the peak shapes reasonably well apart from a small deviation around $\Delta_c = 0$.

far detuning $|\Delta_c| \gg g$, and the most important contribution for these spectra stems from two-photon transitions, with the relative weight of three- and more photon transitions growing for higher powers.
A scan taken along a vertical line slightly mismatched from $\Delta_a = 0$ will lead to an asymmetric spectrum with non-equal peak heights and spacings, as shown in Fig. 3.4(b) for $\Delta_a = 2\pi \times 2$ MHz. Nevertheless, the contribution of single-photon transitions remains small as long as the deviation from $\Delta_a = 0$ is small in comparison to $g$.

## 3.2.2 Nonlinear intensity response

In the last section, it was shown that the anharmonicity of the level spacing in the Jaynes-Cummings model allows to selectively excite a multiphoton transition by choice of the appropriate input frequency, visible in the separate resolution of a single- and a two-photon resonance in the spectra. These spectra 3.1(b),3.2(b) also indicate that the different orders of resonances react differently to a change in the input power. This intensity response is the topic of the following section. However, first comes a short digression concerning different classes of optical nonlinear processes and how they relate to the nonlinearity observed in this experiment.

### Origin of nonlinear optical effects

In general, a great variety of nonlinear processes are known in optical physics which occur from the interaction of light with a medium. They can be roughly separated

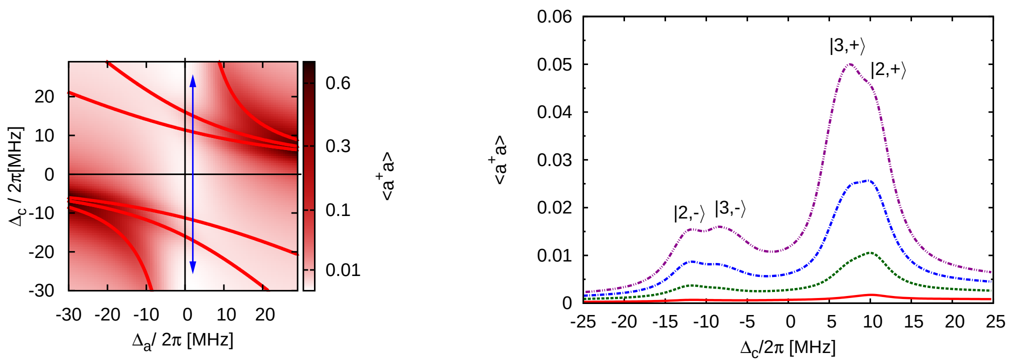

(a) Photon number for different detunings

(b) Asymmetric vertical spectra

**Figure 3.4: Asymmetric vertical spectra.** Scanning vertically with a slight, constant detuning from ($\Delta_a = 0$) results in an asymmetric spectrum, where the amplitudes of the left and right group of peaks quickly start to deviate. The average intracavity photon number as a function of detunings ($\Delta_a$,$\Delta_c$) for a pump power of ($\eta^2 = 2.5\kappa^2$) is depicted in **(a)**. Notice the nonlinear color bar. The solid curves indicate the position of the resonances according to Eq. 3.2 and the arrow indicates the scan direction for the spectra shown in **(b)**. The spectra are calculated for $\Delta_a = 2\pi \times 2$ MHz and pump powers of $\eta^2 = (0.5, 1.5, 2.5, 3.5)\kappa^2$. For other parameters, see Fig. 3.1.

into two groups: effects which rely on inducing a nonlinear polarizability of the medium, resulting in a nonlinear susceptibility, and effects which are based on the actual excitation of an electronic transition. The first type is commonly used for effects which are broadly labeled 'frequency mixing', including sum- and difference frequency generation and optical parametric amplification inside a nonlinear crystal [99]. Microscopically, the nonlinear response of the polarization of the medium to an intense driving field can be explained by an oscillator model: Induced by the electric field of the impinging light, the bound electron oscillates about the nucleus in a potential which is harmonic in lowest order, but becomes increasingly anharmonic for higher driving intensities. This model accounts for the redistribution of intensity from one frequency component of the field to another, but also allows for self-modulation of the impinging light by an intensity-dependent refractive index, the optical Kerr effect. However, the nonlinearity created by a single atom is small, and usually macroscopic media and high intensities are required to observe these phenomena. Although the light field is enhanced greatly inside a high-finesse resonator, it can be shown that the classical model with the usual ansatz of an anharmonic potential does not reproduce the phenomena connected to the higher energy levels which are predicted by the quantum Jaynes-Cummings model [100].

The second type of nonlinearities are characterized by a (near-)resonant interaction of the light with an electronic transition in the medium. This field covers all kinds of saturation nonlinearities, from saturation broadening of an atomic transition line to spectral hole burning and saturable absorbers which are used for short pulse generation in lasers. A special kind of saturation nonlinearity can occur if the absorber is placed inside a cavity: optical bistability, which was already introduced in sec-

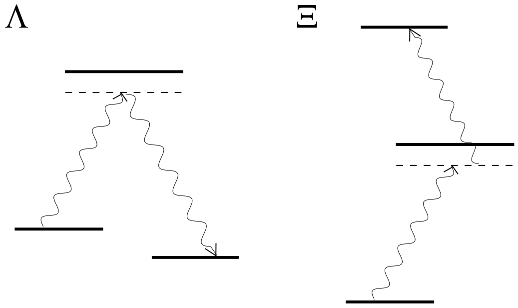

**Figure 3.5: Three-level systems.** The Λ-system is characterized by two (near-) degenerate ground states and one excited state, whereas in the Ξ-system the levels are aligned in a ladder structure.

tion 2.2.2. Since optical bistability is so closely related to cavity QED, nonlinear effects arising from this theory will be discussed in more detail below. Another type of nonlinearity stems from the interaction of the light with more than one electronic transition. One example is electromagnetically induced transparency (EIT), a phenomenon which can occur in three-level Λ-type systems (see Fig. 3.5 for an illustration). EIT can be used to slow down the group velocity of light pulses passing through a medium [101]. Finally, also in free space multiphoton transitions can be driven in Ξ-type systems, used for example for two-photon absorption spectroscopy. Due to the analogy of this kind of spectroscopy to the spectroscopy performed on the Jaynes-Cummings system, this nonlinearity will also be discussed in more detail in the following section.

### Nonlinearities in the optical bistability theory

In section 2.2.2, optical bistability was introduced as a theory which describes the interaction of a classical light field with a quantized medium. Nonlinearities in this system are solely due to the fact that the atom, as a two-level particle, can saturate and thus the absorption of an impinging light field is bleached. Inside a resonator, the back-action of the atom on the field can, under certain conditions, lead to two stable states: either the atom is saturated, resulting in low absorption and a high field intensity (this state is labeled *upper branch*), or the atom is mostly in the ground state, in which case the light field inside the resonator is suppressed (*lower branch*). The numerical analysis of this effect and an illustration were already provided in section 2.2.2 and Fig. 2.5(a). Single-atom bistability has not been observed yet, although it is predicted by theory [79, 80] for parameter regimes of small field fluctuations. Since here the interest lies in a parameter regime of very low photon numbers and small detunings, this condition is not fulfilled, and bistability is not expected to hold. Still, it is instructive to review the intensity response predicted by this theory for the vertical scan proposed in section 3.2. At this point, it is useful to introduce a notation which allows to characterize the intensity response of the system: a development of the intracavity photon number $\left\langle a^\dagger a\right\rangle_{OB}$ as a power series of a parameter $I \equiv \eta^2$ which characterizes the impinging intensity:

$$\left\langle a^\dagger a\right\rangle_{OB} = \beta_1 I + \beta_2 I^2 + \beta_3 I^3 + \ldots \tag{3.5}$$

Of course, this approximation is only allowed as long as the nonlinearity is small, i.e. if one stays on the lower branch. As long as the intensity is low, only the first-order term is relevant and terms proportional to higher orders can be neglected. In this case, the classical limit of the normal-mode resonances is recovered, which is why the parameter $\beta_1$ is identical to the low-intensity limit: $\beta_1 = 1/(|\tilde{\Delta}_c|^2|1-\nu|^2)$ (cp. Eq. 2.27 with the saturation parameter $s_0 = 0$). At slightly higher input intensities, the coefficient $\beta_2$ starts to become relevant. It can be calculated from perturbation theory:

$$\beta_2 = \frac{4|\nu|\left(|1-\nu|^2 - \mathrm{Re}(1-\nu)\right)}{|\tilde{\Delta}_a||\tilde{\Delta}_c|^3|1-\nu|^6} \tag{3.6}$$

where $\mathrm{Re}(\cdot)$ denotes the real part. This coefficient shows resonances only at the positions of the normal modes. Following up on the vertical scan idea presented in section 3.2, which proposes a scan direction avoiding the normal modes, it is clear that the bistability theory does not provide a resonance nor a strong nonlinear response for the proposed scan parameters. In fact, spectra calculated for the parameters from Fig. 3.2(b) only show a small deviation between the semiclassical optical bistability theory and the spectrum expected from the classical theory (Fig. 3.6(a)). The intensity response in this region consequently deviates only slowly from the classical linear function (Fig. 3.6(b)) at the position where quantum theory predicts the two-photon resonance ($\Delta_a = 0, \Delta_c = g$). The nonlinearity can be quantified by approximating $\beta_1, \beta_2$ for these parameters in the limit ($g \gg \gamma, \kappa$):

$$\left\langle a^\dagger a\right\rangle_{OB} \overset{\Delta_a=0,\Delta_c=g}{\approx} \left(\frac{\gamma}{g}\right)^2\left(\frac{\eta}{g}\right)^2 + \left(\frac{2\gamma}{g}\right)^2\left(\frac{\eta}{g}\right)^4 \tag{3.7}$$

As long as the pump strength satisfies $\eta \ll g$, only the first term, which is linear in the intensity, is significant. This is expected since for the chosen parameters the excitation probability of the atom remains low ($< 0.1$), therefore the system remains on the lower branch of optical bistability theory. Consequently, resonances and strong nonlinearities observed in this parameter region are not based on saturation effects and optical bistability.

### Nonlinearities connected to multiphoton transitions

From the viewpoint of quantum theory, the higher-order resonances are accessed by multiphoton transitions. Intuitively, one would assume that the probability of driving a two-photon transition rises with the square of the input intensity, as it is a second-order process which requires two absorptions. In contrast, the probability of a first-order transition from the vacuum to one of the normal modes is linear in the input intensity, as is confirmed by the calculated transition probability in the classical limit (Eq. 2.23a). In the following, the intensity dependence for the excitation of the second doublet will be analyzed.

Spectroscopy of the Jaynes-Cummings system has parallels to the spectroscopy of other multilevel systems, and this experiment can profit from insights obtained in other fields. Actually, a good analogy for the process of two-photon excitations in the

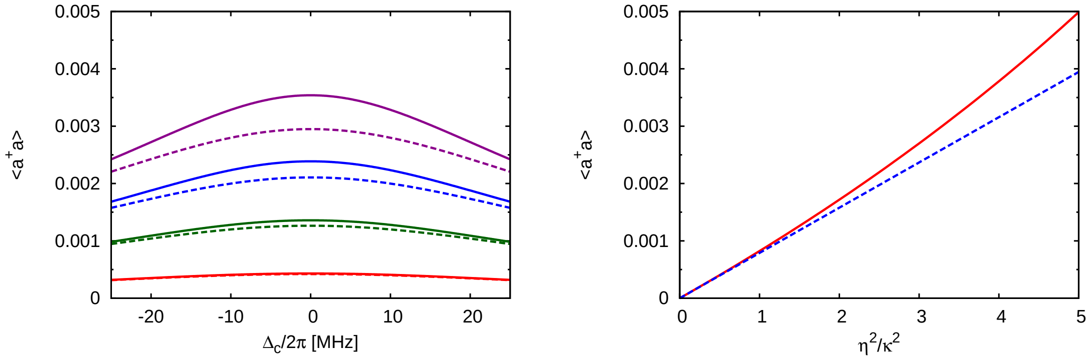

(a) Vertical spectra for $\Delta_a = 0$

(b) Intensity response

**Figure 3.6: Vertical spectra in the bistability theory. (a)** The spectra calculated with the theory of optical bistability for a vertical scan along $\Delta_a = 0$ (solid lines) closely resemble the spectra obtained from the classical limit (dashed lines) for all chosen input powers. The parameters are identical to the ones used for Fig. 3.2(b). **(b)** The dependence of the cavity transmission on the impinging power at the position of the expected two-photon resonance ($\Delta_c = -2\pi \times 11.2$ MHz, solid curve) is only slightly nonlinear in the chosen intensity range and also stays close to the classical limit (dashed line).

atom-cavity system is provided by a two-photon absorption process in a free-space atom with three anharmonically spaced levels in a $\Xi$-configuration (see Fig. 3.5). The three relevant levels would then, for example, be the levels ($|g,0\rangle$,$|1,-\rangle$,$|2,-\rangle$). Due to the strong coupling, the levels $|1,+\rangle$ and $|2,+\rangle$ are far enough detuned as to be neglected, as are states from higher doublets at the moment. The dependence of two-photon absorptions in free-space atoms on the properties of the light field has been investigated thoroughly. It is found that the intensity dependence of the transition probability is governed by the photon statistics of the impinging light[1] [102]:

$$P_{2ph} \propto G^2(0) \tag{3.8}$$

The photon statistics are expressed here by the second-order non-normalized intensity correlation function $G^2(\tau)$ at time $\tau = 0$. Generally it is defined as

$$G^2(\tau) = \left\langle a_p^\dagger(t) a_p^\dagger(t+\tau) a_p(t+\tau) a_p(t) \right\rangle \tag{3.9}$$

where $a_p^\dagger$ and $a_p$ are the creation and annihilation operators for photons in the mode of the impinging light field. $G^2(\tau)$ gives the probability of detecting a photon at time $t+\tau$ if a first photon has been detected at time $t$. This allows an intuitive interpretation of Eq. 3.8: the probability of a two-photon absorption process is proportional to the probability of having two photons arrive at the same time, just as the single-photon transition probability is proportional to the probability of having one photon arrive; the latter is given by the averaged light intensity.

---

[1] This relation is valid as long as the bandwidth of the impinging light is much smaller than the linewidth of the transition and saturation effects are negligible

In Eq. 2.9b, which defines the Hamiltonian describing the pumping of the system, the probe light was modeled as a coherent field. In this case, the correlation function factorizes:

$$G^2_{coherent}(0) = \left\langle a_p^\dagger(0) a_p(0) \right\rangle^2 \propto \langle I \rangle^2 \tag{3.10}$$

This relation confirms that the amplitude of a two-photon resonance in a spectrum should scale with the square of the input intensity. Note that this relation is expected to change if light with a different photon statistics is used: for example, for squeezed light the transition rate should asymptotically become a linear function in the limit of low intensity [103], an effect which was actually observed in the two-photon absorption rate of a cold atom cloud [104]. For a coherent field, deviations from the quadratic dependency of transmitted versus input intensity can arise from saturation, or if other transitions are excited off-resonantly. While in the vertical spectra (Fig. 3.2(b)) saturation is small, the off-resonant excitation from single- and three-photon transitions will influence the intensity dependence on the two-photon resonance. This can again be explained in the development:

$$\left\langle a^\dagger a \right\rangle = \zeta_1 I + \zeta_2 I^2 + \zeta_3 I^3 + \ldots \tag{3.11}$$

$\zeta_1$ describes the off-resonant excitation of the normal modes, given by the low-intensity limit just as in the case of the optical bistability theory (Eq. 3.5) $\zeta_1 = \beta_1$. This process dominates the intensity dependence at the position of the two-photon resonance for very low intensities (for illustration, imagine Fig. 3.3 extrapolated to lower pump intensities). $\zeta_2$ describes the two-photon process, and differs radically from the coefficient obtained for optical bistability $\zeta_2 \neq \beta_2$ [2]. This transition dominates at medium intensities. Higher orders of $\zeta$ take into account the higher multiphoton transitions. The intensity response on the two- and three-photon resonances are depicted in Fig. 3.7. The deviation from the linear classical limit as well as the nonlinear character of the curves is obvious. On the two-photon transition, the intensity dependence is almost quadratic, and it is more than quadratic on the three-photon resonance.

Fig. 3.8 shows the excitation probability of the atom for the same parameters as used in Fig. 3.7. Here, the difference from the classical limit remains small, and the overall excitation stays well below 10%, in spite of the fact that the field intensity in the resonator is strongly enhanced as compared to the classical case. This shows that the additional excitation is predominantly stored in the field and not in the atom; the role of the atom is mainly to mediate the nonlinear response of the field. At this point, the analogy to a free-space two-photon absorption process fails, because there the excitation can only be stored in the atom.

Concluding, one can say that the nonlinearity on the two-photon resonance is a purely quantum effect which appears only for a single atom and a small photon number, since it relies on the anharmonicity of the strongly-coupled atom-cavity system. It can be observed in a regime where the atomic excitation probability is kept small, and thus is fundamentally different from saturation nonlinearities which

---

[2] The analytical form of $\zeta_2$ is difficult to obtain and has not yet been calculated.

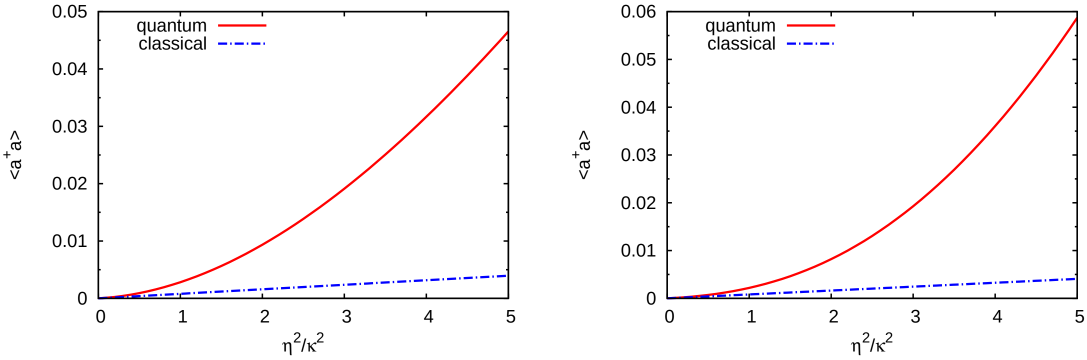

(a) Two-photon resonance

(b) Three-photon resonance

**Figure 3.7: Intensity response in the quantum theory.** Accounting for the quantization of the light field, theory predicts a mainly quadratic intensity response at the position of the two-photon resonance ($\Delta_a = 0, \Delta_c = -2\pi \times 11.2$ MHz) **(a)** and a more than quadratic intensity response on the three-photon resonance ($\Delta_a = 0, \Delta_c = -2\pi \times 7.9$ MHz) **(b)**, with the signal strongly exceeding the classical expectation. For other parameters, see Fig. 3.1.

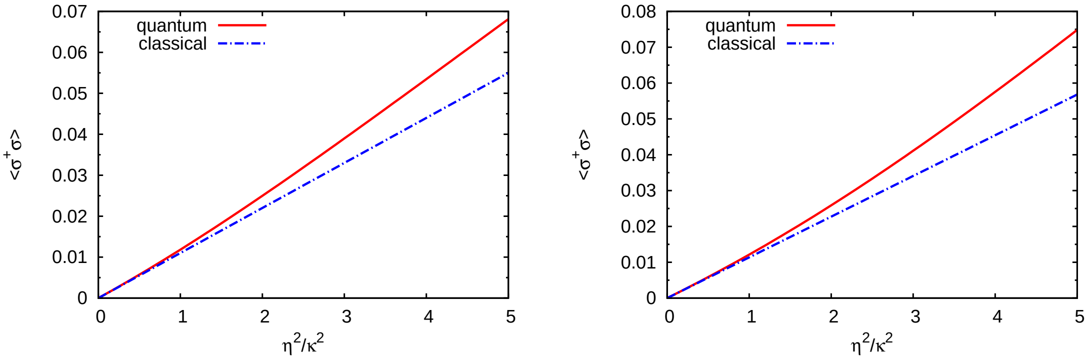

(a) Two-photon resonance

(b) Three-photon resonance

**Figure 3.8: Excitation probability.** The excitation probability of the single atom is calculated for a quantized field (solid lines) and for the classical limit (dashed lines), for parameters matching the two- and the three-photon resonance. The difference between the two theories remains quite small, showing that the excitation of a multiphoton resonance does not necessarily coincide with saturation of the atomic transition. For parameters, see Fig. 3.7.

have been recently observed in other atom-cavity systems [96, 82] at low photon numbers. This nonlinearity could be used to implement a two-photon gateway: only photons which arrive in pairs can be transmitted by the system, while single photons are blocked. Such a feature would be obvious in the photon statistics of the transmitted light: the probability of photons arriving pairwise should be enhanced. This is the topic of the next section.

### 3.2.3 Remarks on the photon statistics

One way of gaining knowledge about the structure of a system is to analyze its spectrum as described in the previous section; a complementary way of obtaining insight is the analysis of the photon statistics of light emitted by the system. Experiments which analyze the correlation of light emitted from a cavity were already discussed in section 3.1.2; especially it was mentioned that light stemming from the excitation of one of the normal-mode resonances in the strong-coupling regime shows anti-bunching because during the time the system needs to decay from the first excited doublet to the ground state, a second excitation with the same frequency is blocked. A similar effect is observed for light emitted by single atoms in free space [105], where also no higher levels are accessible. However, when populating the second doublet, anti-bunching should reverse to bunching, as now two quanta of excitation can be lost from the system within a timescale given by the decay rates; only the emission of a third photon should be suppressed.
In quantum theory, the normalized second order correlation function of light emitted by the cavity is given by

$$g^2(\tau) = \frac{\langle a^\dagger(t)a^\dagger(t+\tau)a(t+\tau)a(t)\rangle}{\langle a^\dagger(t)a(t)\rangle^2} = \frac{G^2(\tau)}{\langle a^\dagger(t)a(t)\rangle^2} \tag{3.12}$$

This corresponds to Eq. 3.1, where the same quantity was expressed with detection probabilities; notice that detection efficiencies below unity do not influence this quantity. $g^2(\tau)$ is displayed for different intensities and scan directions in Fig. 3.9. In a diagonal spectrum (Fig. 3.9(a)), the difference between slight anti-bunching in the region of the normal modes and strong bunching in the region of the multiphoton transitions is clearly visible. A vertical spectrum (Fig. 3.9(b)) shows bunching across the whole scanning range. Generally, bunching as well as anti-bunching reduces as the input intensity is increased; this is unfortunate for experiments, since the measurement time is inversely proportional to the square of the mean transmitted intensity. Observing these correlations was proposed as a means to see higher-order transitions in conventional atom-cavity systems [24], and recently also in condensed-matter atom-cavity systems [27].

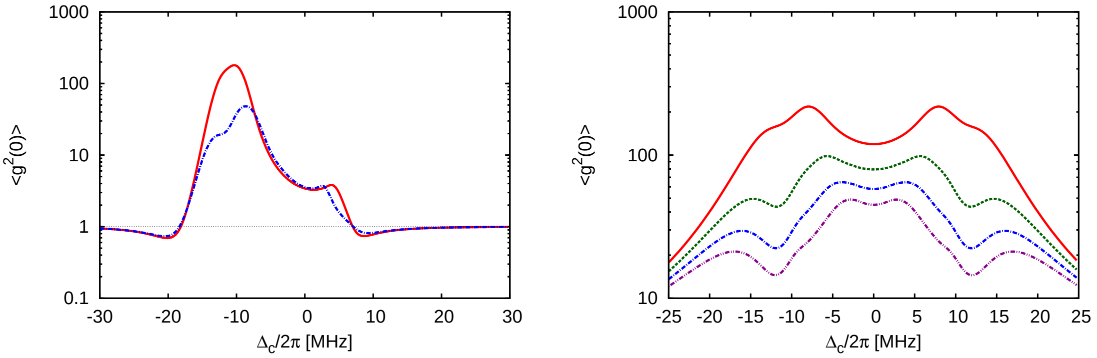
(a) Diagonal autocorrelation spectrum

(b) Vertical autocorrelation spectrum

**Figure 3.9: Autocorrelation spectra of the transmitted light. (a)** A spectrum of the autocorrelation of the transmitted light for an asymmetric diagonal scan reveals anti-bunching close to the normal modes, and bunching in the region of multiphoton transitions. The pump power was $\eta^2 = 0.5\kappa^2$ (solid line) and $\eta^2 = 2.5\kappa^2$ (dashed line). For other parameters, see Fig. 3.1(b). **(b)** A vertical spectrum for $\Delta_a = 0$ only reveals bunching, which is strongest for the lowest input intensity. For parameters, see Fig. 3.2(b).

# Chapter 4

# Motional dynamics in the system

In the previous chapters, the theory of the atom-cavity system was introduced under the simplifying assumption that the position of the atom within the mode is fixed. In the experiment, an intracavity dipole trap confines the atom in a region of strong coupling. The atom oscillates inside the trap, so that there are variations in the coupling and Stark shift. The transmission signal obtained by spectroscopy of a single atom inside the cavity therefore heavily depends on its individual trajectory. A complete spectrum is recorded by averaging over a sufficiently large sample of such trajectories and postselecting on the atoms which were adequately well-coupled (see section 5.2.3).

As it is not straightforward to reconcile this experimental situation with a static theory, another approach is followed: a sample of individual atomic trajectories is calculated in a Monte-Carlo type simulation. Care is taken to imitate the measurement conditions as well as the evaluation procedure as closely as possible.

In the following chapter, the theory which is necessary to implement this simulation is presented. The first step is a discussion of the intracavity dipole trap and its inclusion into the Hamiltonian of the system. The second step comprises the calculation and interpretation of the different forces which follow from this Hamiltonian and the corresponding master equation and which govern the motion of the atom. The calculations were done in the frame of all three cavity-QED models which were introduced in chapter 2. At last, an algorithm is presented which is used to simulate trajectories on the basis of these forces. The results of the simulations are compared to the measurements in chapter 6.

## 4.1 Dipole trap

In a classical picture, the dipole trap relies on the attractive potential on the atomic dipole which is exerted by a far-red detuned strong light field [106]. It exploits the fact that the scattering rate of photons from the field vanishes quadratically with the detuning, whereas the force exerted by the field decreases only linearly. Choosing a large detuning from the atomic transition and a standing-wave intensity pattern thus results in a nearly conservative trap with a potentially long storage time and a small trapping volume.

The intracavity dipole trap [47] is created by resonantly exciting a red-detuned $\mathrm{TEM}_{00}$ mode with the spatial modefunction $\psi_{dip}(\boldsymbol{r})$. Its trapping potential for an atom in the ground state is given by the imposed ac Stark shift on that state:

$$U_g(\boldsymbol{r}) = -\hbar S(\boldsymbol{r}) = -\hbar S_0 |\psi_{dip}(\boldsymbol{r})|^2 \tag{4.1}$$

$S_0$ denotes the Stark shift at an antinode, where $\psi_{dip}(\boldsymbol{r})$ is normalized to reach 1. The Stark shift can be calculated from Eq. 2.7 in the limit of far detuning ($\omega_a \gg \Delta_{dip} \gg g, \Delta_c = 0$):

$$S_0 = -\frac{g_{dip}^2\, n}{\Delta_{dip}} \tag{4.2}$$

Here, $g_{dip}$ is the maximal coupling between the dipole mode and the atom, $n$ is the number of photons occupying the mode, and $\Delta_{dip}$ is the detuning between the dipole field and the atom. The excited state of the atom experiences a Stark shift of the same size as the ground state shift, but in the opposite direction ($U_e(\boldsymbol{r}) = -U_g(\boldsymbol{r})$). Thus, the atomic transition frequency $\omega_a$ is shifted by a total of $2S(\boldsymbol{r})$.

This short theory description of the dipole trap is valid for a two-level atom. An atom effectively behaves as a two-level atom if other transitions can be neglected due to even farther detuning or due to selection rules in the addressed dipole transition. The description of dipole traps which do not fulfill these approximations is more involved, but these traps allow for interesting configurations like a magic-wavelength trap, which is characterized by identical Stark shifts of ground and excited state and thus does not alter the atomic transition frequency. Avoiding the Stark shift completely at the trap center is possible by implementing a blue-detuned intracavity dipole trap [20], where the atoms are stored at a node of the field. These traps are discussed in appendix B.

## 4.2 Hamiltonian and force operators

### 4.2.1 Hamiltonian including the dipole trap

The position dependence of the atomic ground state potential and resonance frequency needs to be included in the description of its interaction with the near-resonant mode. Therefore, the Hamiltonian of the coupled system (Eq. 2.9a in a frame rotating with the probe frequency $\omega_l$) is adapted accordingly:

$$\begin{aligned} H_{JC,kin}(\boldsymbol{r}) &= \frac{\mathbf{P}^2}{2m} + H_{JCP}(\boldsymbol{r}) && (4.3a) \\ H_{JCP}(\boldsymbol{r}) &= -\hbar\Delta_c a^\dagger a - \hbar\Delta_a(\boldsymbol{r})\sigma^\dagger\sigma + \hbar g(\boldsymbol{r})(a^\dagger\sigma + \sigma^\dagger a) + \\ &+ \hbar\eta(a^\dagger + a) - \hbar S(\boldsymbol{r}) && (4.3b) \end{aligned}$$

The kinetic energy of the atom, which has been ignored before, is now explicitly noted in terms of the momentum operator $\mathbf{P}$ and the atomic mass $m$. The atom detuning $\Delta_a(\boldsymbol{r})$ includes the Stark shift, and the coupling constant $g(\boldsymbol{r})$ depends on the probe mode function $\psi(\boldsymbol{r})$:

$$\begin{aligned} \Delta_a(\boldsymbol{r}) &\equiv \omega_l - \omega_a - 2S_0|\psi_{dip}(\boldsymbol{r})|^2 & (4.4) \\ g(\boldsymbol{r}) &\equiv g_0\psi(\boldsymbol{r}) & (4.5) \end{aligned}$$

The spatial variation in the ground state potential $U_g(\boldsymbol{r}) = -\hbar S(\boldsymbol{r})$ is also considered. The eigenstates of the internal energy of the system including the dipole trap can be calculated from $H_{JCP}(\boldsymbol{r})$, and the steady-state expectation values of the system operators calculated in chapter 2 are obtained by the replacement $\Delta_a \rightarrow \Delta_a(\boldsymbol{r})$. Moreover, this Hamiltonian includes all necessary terms for the calculation of forces acting on the atom in the resonator.

### 4.2.2 Force operator

Generally, the force operator is the time derivative of the momentum operator $\mathbf{P} = -i\hbar\nabla$, which is governed by the dual Liouvillian superoperator (see appendix, Eq. A.11):

$$\mathbf{F} = \dot{\mathbf{P}} = \tilde{\mathcal{L}}\mathbf{P} \tag{4.6}$$

This force operator can be divided into two parts: its expectation value and fluctuations around this value:

$$\mathbf{F} = \langle\mathbf{F}\rangle + \Delta\mathbf{F} \tag{4.7}$$

The first term leads to a directed force, and the second term will describe momentum diffusion.

## 4.3 Forces and diffusion in the different theory models

The following section contains an overview over the physical origin and the calculation of the forces acting on the atom in the combined cavity-trap system. At first, some general assumptions are discussed which allow to simplify the calculations.

### 4.3.1 General assumptions on the motion

The motion of the atom is governed by the trapping potential, the probe-field potential and cavity-induced dissipative forces. For the theoretical description of the influence of the cavity fields on the atomic position, some reasonable assumptions are made: First, the total momentum of the atom should be much larger than the momentum transferred during one spontaneous emission. Also, the interaction time between the atom and the field is assumed to exceed the lifetime of the atomic excited state and the decay time of the cavity field by far, so that an average over many emission cycles is possible. Thus, the random character of the diffusion processes causes a stochastic spreading of the atomic momentum distribution, which can be described by diffusion constants. Moreover, the atomic wavepacket is assumed to be very small as compared to the wavelength of the light fields, so that forces can be approximated to act on the barycenter of the atom. Consequently, it is possible to describe the atom as a point-like particle, treating its motion classically by applying Ehrenfest's theorem to the position $\boldsymbol{r}$ and velocity $\boldsymbol{v}$. These external variables evolve under the influence of forces, friction and diffusion coefficients whose values are in turn determined by the evolution of the atom's internal degrees of freedom, and which thus have to be calculated according to the underlying theory model [1] [107]. In the following, $\boldsymbol{r}$ and $\boldsymbol{v}$ will appear as parameters in the calculation of the internal state of the system.

### 4.3.2 Dipole force

Using the Hamiltonian (Eq. 4.3b) in the unitary part of the master equation, the force operator takes the form

$$\mathbf{F} = -\hbar\nabla g(\boldsymbol{r})(a^\dagger\sigma + \sigma^\dagger a) - \hbar\nabla S(\boldsymbol{r})\left(2(\sigma^\dagger\sigma) - 1\right) \tag{4.8}$$

The first term describes the dipole forces exerted by the near-resonant probe light on the atom, while the second term describes effects of the dipole trap. This expression implicitly contains the atom's velocity. For calculations, a development in orders of velocity has to be made. The zeroth and the first order are discussed in the following sections. Higher orders are expected to be small and are thus neglected.

### 4.3.3 Dipole force on an atom at rest

For an atom at rest, the expectation value of the force is obtained by replacing the system operators in Eq. 4.8 by their steady-state expectation value $\langle\cdot\rangle_0$:

$$\langle\mathbf{F}\rangle_0 = -\hbar\nabla g(\boldsymbol{r})\langle a^\dagger\sigma + \sigma^\dagger a\rangle_0 - \hbar\nabla S(\boldsymbol{r})\left(2\langle\sigma^\dagger\sigma\rangle_0 - 1\right) \tag{4.9}$$

The first term describes the dipole interaction between atom and probe light; it attracts the atom to regions of high intensity in the case of red detuning and repels the atom from such regions in case of blue detuning, as long as the atom is in the ground state. The force exerted by the dipole trap (second term in Eq. 4.9) has the same characteristics; it is in fact the formal limit of the first term for large detunings, and adapted to the parameters of the dipole trap mode. However, notice that the expression $(2\langle\sigma^\dagger\sigma\rangle - 1) = \langle\sigma_z\rangle$ in the trap force term is equal to the atomic inversion and thus influenced by the near-resonant light, which is the main cause of atomic excitation. It describes the fact that the (red) trap confines only atoms in the ground state, whereas atoms in the excited state are expelled for reasons of the

---

[1] This approach of separating the evolution of the external and internal variables, and, if applicable, quantizing only the internal variables, is often referred to as 'semiclassical'. In this context, this term refers to the classical treatment of atomic position and velocity, while the atom and the field are fully quantized. It should not be confused with the 'semiclassical' bistability theory of the fixed-atom cavity system introduced in chapter 2, which treats the light field classically.

inverted Stark shift. This is why a high atomic excitation probability reduces the effective trap depth.

In the classical [42, 108] and bistable [69] limit, the steady-state dipole force can be calculated analytically by separating the mixed operator products of the form $\left\langle a^\dagger\sigma\right\rangle$ and inserting the respective single-operator expectation values as calculated in section 2.2. The quantum model requires a numerical calculation of the operator products (for implementation, see appendix A.1).

### 4.3.4 Velocity-dependent forces and cavity cooling

If the atom is at rest inside the cavity, there is sufficient time for the system to evolve into its steady state, which is assumed on a timescale of $(\gamma, \kappa)^{-1}$ after a disruption of the system as caused, for example, by the emission of a photon. If the atom moves inside the mode, the system is not able to reach the steady state for the current atomic position, but lags slightly behind. Consequently, the system acquires a hysteresis, which leads to a velocity-dependent ('friction') force. The sign of this force depends on the respective atom and cavity detunings. It can cause very efficient damping of the atomic motion (cavity-cooling, [46]) but can also accelerate the atom.

As long as the velocity of the atom is small enough such that it travels only a fraction of a wavelength within the relaxation time of the system ($\boldsymbol{kv} \ll (\kappa, \gamma)$, where $\boldsymbol{k}$ is the wavevector of the field), the friction force can be calculated with perturbation theory to first order in the atomic velocity. Then, the total force can be expanded into orders of velocity, thus defining a friction tensor $\bar{\beta}$:

$$\langle \mathbf{F} \rangle = \langle \mathbf{F} \rangle_0 + \langle \mathbf{F} \rangle_1 := \langle \mathbf{F} \rangle_0 - \bar{\beta}\boldsymbol{v} \tag{4.10}$$

#### Classical and semiclassical calculation

Calculation of the friction tensor in the classical [42] and semiclassical [69] case is lengthy but conceptually simple, again due to the advantage of separating operator products. The procedure [109] is sketched here: At first, the relevant system operators ($(a, a^\dagger, \sigma, \sigma^\dagger, [\sigma_z])$ for the [semi]classical case) are expanded in orders of velocity:

$$\langle \hat{o} \rangle = \langle \hat{o} \rangle_0 + \langle \hat{o} \rangle_1 + \ldots \tag{4.11}$$

Then the operator products in $\langle \mathbf{F} \rangle$ are separated and the force operator is expanded, retaining only terms in first order of the velocity:

$$\begin{aligned} \langle \mathbf{F} \rangle_1 &= -\hbar\nabla g(\boldsymbol{r}) \left( \langle a \rangle_0^* \langle \sigma \rangle_1 + \langle a \rangle_1^* \langle \sigma \rangle_0 \right) + c.c. \\ &- 2\hbar\nabla S(\boldsymbol{r}) \left( \langle \sigma \rangle_0^* \langle \sigma \rangle_1 + \langle \sigma \rangle_0 \langle \sigma \rangle_1^* \right) \end{aligned} \tag{4.12}$$

Next, the expectation value of these operators is calculated with perturbation theory to the first order in velocity, using the Heisenberg equations of motion (Eq. 2.19). To this end, the total time-derivative on the left-hand side of these equations is expanded:

$$\langle \dot{\hat{o}} \rangle = \frac{\partial}{\partial t} \langle \hat{o} \rangle + \boldsymbol{v}\nabla \langle \hat{o} \rangle \approx \boldsymbol{v}\nabla \langle \hat{o} \rangle_0 + O(\boldsymbol{v}^2) \tag{4.13}$$

Since the Hamiltonian contains no explicit time dependence, the partial derivative is dropped. The operators on the right-hand side of Eqns. 2.19 are also expanded. This leaves a coupled set of 2 (classical) or 5 (bistable) equations of terms linear in the velocity, which can then be solved.
The lengthy analytical result for the classical calculation including the dipole trap can be found in [108]. An expansion of this expression to a three-dimensional trap lattice configuration can be found in [54]. The friction coefficient in the semiclassical model was reduced to matrix form and then calculated numerically.

### Quantum calculation

In the quantum model, the calculation of the friction tensor is more involved. It was originally performed in [107] for an atom moving in a free-space field, yielding a result which is analogous to classically derived friction tensors. It states that the friction tensor $\beta_{i,j}$ ($\{i,j\}$ refer to Cartesian coordinates {x,y,z}) can be expressed in terms of two-time correlations of the Cartesian components of the force operator $\mathbf{F}$:

$$\beta_{ij} = \frac{1}{\hbar}\,\mathrm{Im}\left(\int_0^\infty d\tau\;\tau\;\langle F_i(t)F_j(t-\tau) - F_j(t-\tau)F_i(t)\rangle_0\right) \tag{4.14}$$

Owing to its generality, this expression is also applicable for an atom inside a resonator. It reproduces the friction tensors deduced in the frame of the classical and semiclassical cavity QED models as described in the previous section, and it can be evaluated numerically for the case of the quantized atom-cavity system (see appendix A.1).

## 4.3.5 Momentum diffusion

Random changes in the atomic momentum $\Delta P_i = P_i - \langle P_i\rangle$ lead to a spread in its expectation value. The linear order of this spread is characterized by a diffusion tensor $\bar{D}$:

$$2D_{ij} = \frac{d}{dt}\,\langle \Delta P_i \Delta P_j\rangle \tag{4.15}$$

Diffusion in the atom-cavity system is caused by two different processes: spontaneous emission and dipole force fluctuations.

$$\bar{D} = \bar{D}_{sp} + \bar{D}_{dp} \tag{4.16}$$

### Spontaneous emission

Each spontaneous emission of a photon is accompanied by a recoil kick on the atom. Since the emission direction is random, this results in diffusion. The diffusion tensor is given by the square of the momentum transferred to the atom during an emission process $(\hbar k)^2$ times the emission rate, which is the product of the decay rate $2\gamma$ and the excitation probability $\langle\sigma^\dagger\sigma\rangle$:

$$2D_{sp,ij} = \hbar^2 k^2 \epsilon_{ij}\; 2\gamma\langle\sigma^\dagger\sigma\rangle \tag{4.17}$$

The tensor $\epsilon_{ij}$ describes the spatial distribution of the photon emission, which is determined by the orientation of the dipole moment with respect to the polarization of the probe light field. For $\sigma_+$-transitions, induced by circularly polarized probe light exciting an atomic dipole which is oriented along the cavity axis, the dipole emission characteristics is given by $\{\epsilon_{xx} = 2/5, \epsilon_{yy} = \epsilon_{zz} = 3/10, \epsilon_{i \neq j} = 0\}$ [110].

### Dipole force fluctuations

Fluctuations of the dipole force around its mean value (cp. Eq. 4.7) also lead to a spread in the expectation value of the atomic momentum, which can be expressed in terms of correlations of the force fluctuations. This can be seen by formally integrating $\Delta F_i = d(\Delta P_i)/dt$

$$\Delta P_i(t) = \int_0^\infty \Delta F_i(t-\tau) d\tau + \Delta P_i(0) \tag{4.18}$$

Inserting the result into Eq. 4.15 yields

$$2D_{dp,ij} = \mathrm{Re}\left( \int_0^\infty d\tau \, \langle \Delta F_i(t) \Delta F_j(t-\tau) + \Delta F_j(t-\tau) \Delta F_i(t) \rangle_0 \right) \tag{4.19}$$

This expression is the quantum analogue of the classical diffusion tensor appearing in the theory of Brownian motion; it is also obtained in a more rigorous derivation [107]. To determine its value in the frame of the different cavity QED models, the correlations have to be evaluated as discussed in section 4.3.4.

In the limit of low intensity, it is possible to recast the trace of the diffusion tensor $\bar{D}_{dp}$ into a universal form which is reminiscent of the coupled harmonic oscillator model [45]:

$$2D_{dp} = |\hbar \nabla \langle \sigma \rangle|^2 \cdot 2\gamma + |\hbar \nabla \langle a \rangle|^2 \cdot 2\kappa \tag{4.20}$$

The first term describes a fluctuating dipole coupled to classical field, and is also valid for an atom in a free-space laser field [111]. The cavity setting gives rise to the second term, which describes a fluctuating field coupled to a classical dipole. This expression can be evaluated analytically [42, 108].

## 4.4 Monte-Carlo simulations

The comparison of measurement results to simulations has a longstanding tradition in this group [112, 18], and the simulations have been of great assistance in understanding the details of measurements, as, for example, the complex impacts of different heating mechanisms on the system [113]. The main goal of the simulations presented here is to point out the deviations in transmission spectra which are expected from the different theory models if the low-saturation limit is lifted. The following section presents the basic algorithms of the simulations; an extensive discussion can be found in [100].

### 4.4.1 Algorithm

The atomic trajectory is calculated by numerically integrating the coupled set of three-dimensional Langevin equations of motion for a classical, point-like particle with position $\boldsymbol{r}$ and momentum $\boldsymbol{p}$:

$$\begin{aligned} \dot{\boldsymbol{r}} &= \frac{\boldsymbol{p}}{m} && (4.21a) \\ \dot{\boldsymbol{p}} &= \mathbf{F}(\boldsymbol{r},\boldsymbol{p}) = \langle \mathbf{F} \rangle_0 - \bar{\beta}\frac{\boldsymbol{p}}{m} + \delta\dot{\boldsymbol{p}}_{sp} + \delta\dot{\boldsymbol{p}}_{dp} && (4.21b) \end{aligned}$$

We assume that the internal atomic variables reach their steady state on a timescale much faster than the motion. The change in momentum is then determined by the steady-state expectation value of the dipole force at the given atomic position and the friction tensor in first order of velocity. Only these forces are considered when performing a time step in the integration. Diffusion due to spontaneous emission and dipole force fluctuations is implemented by adding random momentum kicks $\delta\boldsymbol{p}_{sp}, \delta\boldsymbol{p}_{dp}$ to the total momentum after each time step $\delta t$. The average size of these kicks is a function of the respective diffusion tensors, chosen such that the averaged spread in each direction fulfills Eq. 4.15

$$\left\langle \delta p_{ii}^2 \right\rangle = 2 D_{ii} \delta t \tag{4.22}$$

For the spontaneous emission, the momentum kicks are allotted by choosing random, uniformly distributed vectors out of an ellipsoid. The main axes of the ellipsoid are given by $p_{sp,ii}^{max} = \sqrt{10 D_{sp,ii}\delta t}$; the deviation from a sphere reflects the dipole-emission pattern. For the diffusion due to dipole force fluctuations, only the component along the cavity axis $D_{dp,xx}$ is considered, as the other components are small. This diffusion is simulated by choosing a random momentum kick out of an interval $[-p_{dp}^{max}, p_{dp}^{max}]$ with $p_{dp}^{max} = \sqrt{6 D_{dp,xx}\delta t}$. This procedure reproduces the first momentum of the stochastic spreading of the velocity distribution.

### 4.4.2 Simulation run

In the experiment, the atoms are injected into the dipole trap from an atomic fountain (see chapter 5). This is simulated by starting with an atom which is located at a distance of $y_0 = -2w_0$ below the cavity center, and moves towards the cavity with an initial velocity of $v_y = 0.1$ m/s. The initial position in the $(x, z)$-plane is randomized over the area $x_0 \in [-20\lambda, +20\lambda]$, $z \in [-0.4w_0, +0.4w_0]$, and the atom possesses a random initial velocity of maximally three recoil-velocities $v_z \in [-3v_{rec}, +3v_{rec}]$ in the direction perpendicular to the cavity axis and the injection direction.
Starting from this configuration, the integration algorithm is executed with a time step of $\delta t = 10$ ns. During the run, the experiment is imitated as closely as possible, by copying the trigger mechanism for the trapping of an atom in the dipole trap and the subsequent measurement sequence. After each time step, the intracavity photon number and the excitation of the atom are noted. The simulation run is continued

until an atom escapes the cavity volume either in radial direction ($y^2 + z^2 > (2w_0)^2$) or by hitting a mirror ($|x| > 75\lambda$). The photon number and excitation are then averaged over different intervals determined by the measurement sequence and the result is entered into a database, together with other key results of each run such as the atom's position at the triggering of the trap or the storage time of an atom. The recorded data include the set of information obtained from a run of the experiment, therefore the evaluation can be done analogously.

### 4.4.3 Numerical methods and computational effort

The integration routine is based on the multistep algorithm by Adams, Bashforth and Moulder [114, 115], which requires only one calculation of forces, friction and diffusion constants per time step. For implementation of the stochastic processes, the 'Mersenne Twister', a highly equidistributed uniform pseudorandom number generator [116], is used.

As mentioned in the previous section, the implementation of the force and diffusion calculations depends on the model. Each model requires different computational effort:

- **Coupled harmonic oscillator model:** All required expressions are available as analytical formulas, allowing for fast computation.
- **Model of optical bistability:** The numerical calculations are fast. In this model, two solutions are possible in the bistable regions. If such a case is encountered, the value closest to the one from the last iteration is chosen, corresponding to the physical principle of hysteresis.
- **Quantum model:** The numerical effort for calculations rises quickly with the number of Fock states $N$ used for the basis, as the number of coupled differential equations scales as $N^2$. Therefore, $N$ had to be limited to three ($|0\rangle$,$|1\rangle$,$|2\rangle$), fully including only the dressed states up to the second doublet. Comparison to fixed-atom theory shows that this is sufficient to describe most of the measurements. Only some measurements performed at higher intensities are expected to be influenced noticeably by the presence of the third doublet, and thus associated simulations require an inclusion of this doublet. This was done in a hybrid model: Four Fock states were used for the calculation of the intracavity photon number during every 20th time step, and only these intervals were used for the evaluation of the average transmission. In this way, population of the third doublet is included in the transmission spectrum, although it has no influence on the propagation of the atom. With these type of simulations, the calculation of a single spectrum requires about 50 hours on 30 nodes of a computer cluster.

### 4.4.4 Trap depth fluctuations

Although the intensity and frequency of the laser used for the dipole trap are stabilized via a feedback loop in the experiment, fluctuations of the trap depth cannot be completely avoided. Such fluctuations transfer to the Stark shift and thus bear influence on the trajectory. They are included into the simulations by randomly choosing a value from a Gaussian distribution centered around the intended trapdepth. The rms width of the distribution is set to 7% of the average value, which is an upper limit for the fluctuations measured in the experiment. The simulated fluctuations are uncorrelated, i.e. they correspond to white noise. Therefore they are not able to reproduce parametric heating, which occurs if the spectral noise density has sizable components at twice the trap frequency of the dipole trap [117]. This may be a reason for storage time deviations between simulation and experiment. Implementation of fluctuations with a more realistic spectral noise density is under way [100].

# Chapter 5

# Technical realization of the experiment

The history of the experiment being reported on here dates back about a decade; it became fully operational in 1999 with the observation of single atoms transiting through the high-finesse resonator after being launched from an atomic fountain [37]. Since this time, the fountain and the resonator remained basically unchanged. Major improvements in the laser system and computer control and especially the addition of an intracavity dipole trap, which allows to store the atom inside the resonator, provided the basis for spectroscopy of the strongly coupled atom-cavity system. In the first section of the following chapter, an overview on the physical properties of the resonator and the technical implementation of the experiment is provided; a more extensive description can be found in earlier works [118, 108, 98]. The second section details the measurement procedure and the data evaluation for the spectroscopy measurements which resulted in the observation of multiphoton transitions in this system; the obtained spectra are discussed in chapter 6.

## 5.1 Setup

A simplified sketch of the setup is shown in Fig. 5.1. The heart of the experiment is the high-finesse resonator (section 5.1.2). Two $\mathrm{TEM}_{00}$ modes, separated longitudinally by two free spectral ranges (FSR), can be independently excited by two different laser beams (section 5.1.3): one beam, the probe laser, is near-resonant to the D2-transition of $^{85}$Rb at a wavelength of 780.2 nm. The second laser, with a wavelength of 785.2 nm, provides the red-detuned intracavity standing-wave dipole trap. It is also used to continuously stabilize the cavity length. Note that the antinodes of probe field and dipole trap overlap at the center of the cavity, and only single atoms entering the cavity in this region are trapped (section 5.2.1). The atoms are prepared as a cold atomic cloud in a magneto-optical trap (MOT) below the resonator and launched towards the resonator by means of an atomic fountain (section 5.1.1). The presence of an atom in the mode changes the transmission of the probe field, which is monitored by two single-photon counting modules (SPCM) in a Hanbury-Brown-Twiss configuration. The dipole trap light is detected separately by a photomultiplier module; the two light fields are separated behind the resonator with the help of a grating (section 5.1.4).

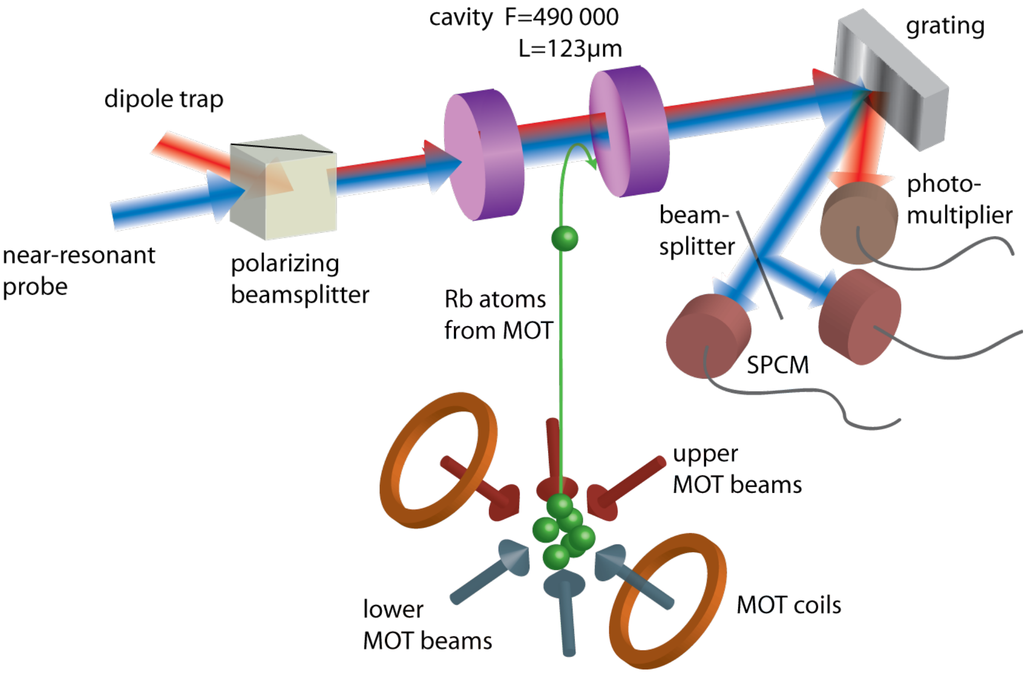

**Figure 5.1: Schematic of the experimental setup.** Cold atoms are prepared in a MOT below the resonator, injected into the resonator by means of an atomic fountain and trapped in an intracavity dipole trap (red). The presence of the atoms is detected by monitoring the transmission of the near-resonant probe laser (blue), which is separated from the trap light with a grating.

### 5.1.1 Magneto-optical trap and atomic fountain

Rubidium atoms can be released into the lower part of the vacuum chamber (Fig. 5.2), which is connected to the main part of the chamber by a differential pumping tube, by running current through a dispenser (SAES Getter). These atoms are loaded into the MOT, which is a standard means to prepare a cold atom cloud [119]. The MOT consists of six pairwise counter-propagating beams which intersect at the zero point of a magnetic field produced by a pair of coils in anti-Helmholtz configuration (see Fig. 5.1). These six beams are created from two initial beams, each of which double-passes through an acousto-optic modulator (AOM) for frequency tuning. Behind the AOM, each beam is split into three beams, providing the lower respectively upper MOT beams. Initially, the detuning is set to a value of $\Delta = -2\pi \times 45$ MHz below the MOT transition ${}^5S_{1/2}F = 3 \rightarrow {}^5P_{3/2}F' = 4$ of ${}^{85}$Rb. By adding a molasses cooling phase after the loading phase, the atom cloud can be cooled to a temperature of $\approx 5\ \mu$K. Then, the lower MOT beams are gradually detuned to a frequency of

$-2\pi \times 41.8$ MHz in order to accelerate the atom cloud upwards ('atomic fountain'). The atoms perform ballistic trajectories towards the cavity, which is situated at the turning point, 25 cm above the MOT, in the main part of the vacuum chamber. In this way, slow atoms from the diluted cloud enter the cavity after a time of flight of $\approx 210$ ms, and can be trapped with the intracavity dipole trap (see section 5.2.1).

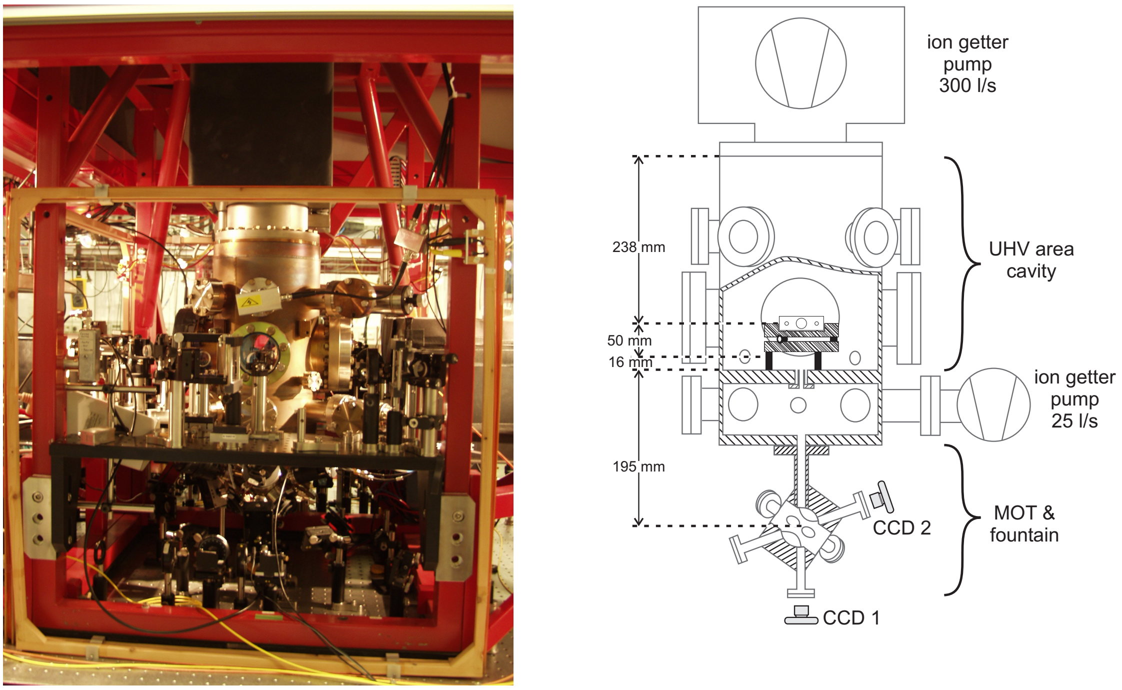
(a) Picture of the vacuum chamber

(b) Schematic of the vacuum chamber

**Figure 5.2: Picture and schematic of the vacuum chamber.** The lower part of the vacuum chamber is used for the MOT; it is attached to the main part of the chamber, which holds the cavity on a vibration isolation setup, via a differential pumping tube. The chamber is suspended from an ion getter pump, which is attached to a metal rack. The pressure in the main chamber is below $10^{-10}$ mbar. The wooden frames visible in the left picture hold coils used for compensating the earth's magnetic field.

### 5.1.2 High-finesse cavity

The cavity consists of a pair of mirrors with a diameter of 7.75 mm and a radius of curvature of 200 mm (see Fig. 5.3(a)). The dielectric coating of the mirrors is characterized by very low transmission and loss coefficients ($\mathcal{T} = 2.8$ ppm, $\mathcal{L} = 4.5$ ppm). The mirrors are glued to aluminum holders, which are mounted on a piezo-ceramic tube used for fine-tuning the cavity length (Fig. 5.3(b)). Holes drilled in the piezo tube enable the atoms to enter the resonator. The mirrors and piezo tube are clamped within a Teflon block so that the piezo-tube is able to elongate. The Teflon block is placed upon a two-stage vibration isolation consisting of copper disks separated by Viton tubes; this setup shields the cavity from acoustic noise [120].

The FSR of the cavity was measured to $2\pi \times 1.21$ THz. This amounts to a cavity length of $L = 2\pi c/(2\text{FSR}) = 123\ \mu$m. The cavity length is actively stabilized (see section 5.1.3). The linewidth (HWHM) of the cavity is $\kappa = 2\pi \times 1.25$ MHz. From this, the finesse of the cavity can be calculated to be $\mathcal{F} = \text{FSR}/2\kappa = 490000$. An average intracavity photon number of 1 leads to an average transmission of 0.9 pW. The waist of the TEM$_{00}$ mode of the cavity is $w_0 = 29.1\ \mu$m. The mode volume of this near-planar cavity is given by $V = \pi w_0^2 L/4$ and determines the value of the coupling constant between atom and light field, together with the atomic dipole transition matrix element (Eq. 2.2). Since the probe light is right circularly polarized ($\sigma_+$) and a weak magnetic field along the cavity axis defines the quantization axis, the atoms are rapidly pumped to the closed transition $^5S_{1/2}F = 3, m_f = 3 \rightarrow {}^5P_{3/2}F' = 4, m_f' = 4$ of $^{85}$Rb. With these settings, the coupling at an antinode of the standing wave field amounts to $g_0 = 2\pi \times 16$ MHz.

(a) Mirrors

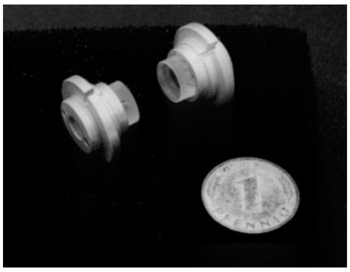

(b) Mounting of the high-finesse mirrors

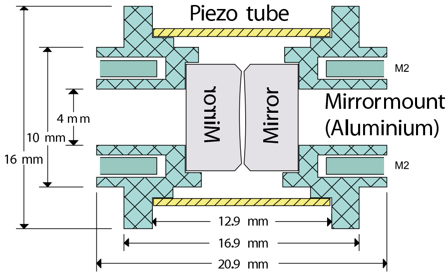

(c) Mirror holder and vibration isolation

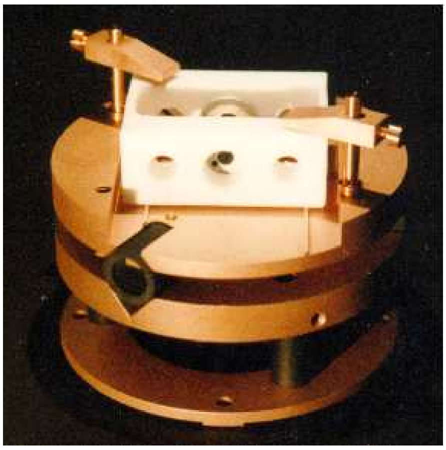

**Figure 5.3: High-finesse resonator. (a)** Picture of the cavity mirrors glued to aluminum holders. **(b)** Schematic of the mounted mirrors separated by a piezo tube. **(c)** Picture of the vibration isolation stage with the mirrors placed on top inside a Teflon holder.

### 5.1.3 Laser system and length stabilization of the science cavity

For the measurements presented in this thesis, three different lasers are required. The first laser, a Titanium-Sapphire laser (Coherent model MBR110), is tuned to

emit light at 780.2 nm. This laser is stabilized onto a Rb vapor cell via Doppler-free saturation spectroscopy. Apart from the stabilization path, the light is divided into four more beams: two beams ('upper and lower MOT beams') are needed to operate the MOT and the atomic fountain, while the third beam ('probe beam') is used to probe the atom-cavity system. The intensity of each of these beams is stabilized by feedback onto an AOM set up in double-pass configuration, which at the same time allows to adjust the frequencies. The last beam is used to create a reference for the length stabilization of a transfer cavity. This cavity, with a FSR of $2\pi \times 300$ MHz and a linewidth of $2\pi \times 150$ kHz, is needed in turn to provide a stable reference for the frequency locking of the dipole laser.
The dipole laser is a diode laser set up in Littrow configuration (Toptica model DL100), which produces light at 785.2 nm. It is stabilized onto a mode of the transfer cavity at a frequency lying close to a resonance of the high-finesse science cavity, two FSR red detuned from the mode excited by the probe light. The beam of the dipole laser which is directed onto the science cavity ('dipole beam') can be frequency tuned by an AOM in order to reach resonance conditions. This light serves as a reference for stabilizing the length of the science cavity, via a feedback on the piezo tube. Changing the detuning of the dipole laser via the AOM then in turn allows to adjust the cavity length. At the same time, this light is used to create an intracavity dipole trap for the atoms. The light intensity and thus the trap depth are controlled by feedback on the AOM. A change in the trap depth would normally lead to a change of the amplitude of the error signal which is used for the length stabilization. To avoid this, the error signal is normalized onto the input intensity with an electronic divider [108].
Two additional lasers (one Titan-Sapphire laser at 772 nm and one diode laser at 775 nm), which are also stabilized onto the transfer cavity, provide the possibility to create a blue-detuned intracavity dipole trap. This kind of trap has not been used for the measurements presented here, but will be shortly introduced in appendix B.1.
For operation of the MOT, one more laser is required to repump atoms from the state $^5S_{1/2}F = 2$ to the state $^5S_{1/2}F = 3$ (see Fig. A.1). This laser (a Toptica model DL100-diode laser) is stabilized onto a Rb vapor cell on the repump transition $^5S_{1/2}F = 2 \rightarrow {}^5P_{3/2}F' = 3$ and overlapped with the lower MOT beam.

### 5.1.4 Detection of probe and trap light

Probe light and dipole light are emitted by the cavity into the same polarization and almost identical spatial modes, but with an intensity difference as big as $\approx 10^5$. In order to allow for independent detection of the weak probe light (which typically has a power between a few fW and several pW), the two frequencies need to be separated efficiently. This is done with a holographic reflection grating (American Holographics) with 2300 lines/mm, which reflects vertically polarized light with an efficiency of 90%. To obtain polarization-independent reflection, the circularly polarized light is divided into two components of linear polarization with a polarizing beam cube (PBC), the horizontally polarized part is rotated with a half-wave plate (HWP) and the two components are directed separately onto the grating. After

reflection, horizontal polarization of the second component is restored with another HWP and the components are recombined on a second PBC. Now the spatial separation between the probe light and the dipole light is sufficient to allow to direct the beams onto different mirrors. Residual dipole light in the path of the probe beam is filtered out by a narrow-band (1 nm) interference filter (Nano layers) with a peak transmission of 80%. Behind this filter, the dipole light is suppressed by about 80dB. The probe light is split up by a non-polarizing beam splitter and directed onto two single-photon-counting modules (SPCM AQR-13, Perkin&Elmer), which detect photons with a quantum efficiency of about 50 %, a dead time of about 50 ns and a dark count rate of about 250 Hz. The two SPCMs form a Hanbury-Brown–Twiss configuration [121] to allow for correlation measurements. The overall detection efficiency for photons transmitted by the cavity is about 30%. A photon detection of each SPCM is recorded as a time stamp with a resolution of 1 ns on one channel of a time-digitizer card (P7888 by FASTComtec).
The dipole light is detected by a photomultiplier module (H6780-20, Hamamatsu), amplified with a low-noise transimpedance amplifier (FEMTO current amplifier, gain 500 kΩ, bandwidth 4 MHz) and recorded by a transient recorder card (SPECTRUM PCI.248). The detection setup also includes the possibility of independently detecting dipole light from the optional blue-detuned dipole trap (see [98]).

### 5.1.5 Computer control of measurement sequence

The experiment is computer-controlled by a program written in C++, which allows for automatized control of all relevant settings like intensities and detunings of the probe, dipole and MOT beams. These parameters are calibrated regularly in separate gauge measurements. Complex timing sequences are executed by a programmable timer card (NI PCI-6025E) which is controlled by the measurement program. The raw data of photon arrival times and dipole power during a measurement are directly stored on a hard disc, whereas the measurement parameters as well as key results of the measurement are entered into a relational database (PostgreSQL), which greatly simplifies statistical data evaluation.

## 5.2 Measurement and data evaluation

The main goal of this thesis is to explore multiphoton transitions by measuring spectra of the system along two different directions in the ($\Delta_a$,$\Delta_c$)-parameter plane and at varying probe intensities. In the following section, a short overview over the protocol used for trapping slow atoms in the intracavity dipole trap and for measuring the spectrum of the atom-cavity system will be given. In order to ensure constant strong coupling, postselection of the measured data is required; the data evaluation and postselection process is discussed briefly. More details can be found in [98, 108], where a similar protocol was used to measure the normal-mode spectrum of the system.

### 5.2.1 General information

#### Loading of the dipole trap

Slow atoms from the MOT are injected into the cavity by means of the atomic fountain. In order to trap these atoms in the conservative potential of the red intracavity dipole trap, the potential depth has to be increased as soon as the atoms are located inside the trap. At the beginning of the sequence, a trap power of 80 nW is used to guide the atoms into the antinodes of the trap. The arrival of the atoms is monitored by observing the transmission of probe light resonant to the cavity, which shows a sharp dip as an atom enters a region of strong coupling. A deep drop in transmission is only caused by atoms arriving at the center of the cavity, where antinodes of probe light and dipole trap overlap. Upon detection of such a large dip, a trigger is activated which causes the trap power to rapidly increase to 140 nW, thereby trapping the atom. The trapping efficiency is above 95% and the lifetime of undisturbed atoms in the trap is on the order of several 10 ms. The triggering mechanism is enabled only 210 ms after launch of the atom cloud from the MOT. At this time, the center of the cloud has passed the resonator and single atoms arrive with a velocity $\leq 10$ cm$/s$. Therefore, the probability of accidentally trapping more than one atom is small. The probe light which is used to detect the atomic transit is slightly blue-detuned from the atomic resonance frequency. Therefore it cools the axial motion of the atom via cavity cooling [46].

#### Idea of scanning and postselection mechanism

Measuring a spectrum of the system entails detuning of the probe light from the cavity resonance $\Delta_c \neq 0$, away from cavity-cooling conditions. To ensure that the atom remains strongly coupled during the measurement, the desired measurement parameters (probe and cavity detunings and probe power) are set only for a short interval of 100 $\mu$s, labelled 'probe interval'. Before and after each probe interval, the cavity detuning $\Delta_c$ is reset to 0 and the probe power is set to 0.3 pW for an interval of 500 $\mu$s duration, the 'check interval'. In the check interval, the atom is axially cooled and its localization is apparent from the cavity transmission. A measurement cycle consists of a series of 20 to 30 pairs of probe and check intervals and finishes with a check on the stabilization of all lasers and the cavity. After the measurement has been completed, the transmission during each check interval is evaluated to obtain information on the localization of the atom. Only the probe intervals for which both surrounding check intervals show a coupling of at least a certain fraction of $g_0$ (usually 60%) are postselected for further evaluation, leaving a subset of probe intervals that fulfill the condition of sufficiently strong coupling. This postselection criterion is independent of the history of the system and allows to combine probe intervals from many different trapping events. Averaging the transmission detected during these probe intervals then gives the spectrum of the system.

### A single trapping event

As an illustration of the measurement sequence, a sample trace is shown in Fig. 5.4. Here, an atom arrives 223.5 ms after the launch of the atom cloud and triggers the switching of the dipole trap power. Upon the trigger, the sequence of probe and check intervals is started. The two kinds of intervals are easily distinguishable due to the different powers of the impinging probe light[1] (high during the probe interval and low during the check interval). The probe intervals are additionally marked with boxes. After the trigger, transmission of the probe light is mostly suppressed by the strongly coupled atom during the check intervals and sometimes vanishes completely, whereas transmission does occur during the probe intervals. After the atom gets lost from the trap at about 234.5 ms, the check intervals show a high transmission whereas almost no photons arrive during the probe intervals. These probe intervals are filtered out by the postselection process. The postselection criterion for the probe intervals in this case requires that less than 5 photons are detected during each of the neighboring check intervals, which corresponds to an average coupling $g$ of better than 60% of the maximal possible value ($g > 0.6g_0$). All probe intervals which fulfill this condition are marked by a shaded background.

More details on the technical implementation of the measurement sequence, statistics of the measured data and the postselection process will be given in the rest of the chapter.

### Intensity switching

Whereas possibly high intensities have to be set during the probe intervals, it is not expedient to use a high intensity during the check interval: cavity cooling works efficiently at low intensities and higher intensities would only enhance radial heating, which cannot be counteracted in the present setup and thus reduces the storage times. Therefore, the probe intensity has to be switched rapidly from 0.3 to maximally 3.5 pW. The necessary gain is too high for the servo loop which normally controls the probe power. Therefore, during the probe and check cycle the control of the RF-intensity on the AOM which determines the probe power is transferred to a function generator. The voltage resulting in the correct probe power depends on the probe detuning because of the frequency-dependent efficiency of the AOM; because of this, the correct voltage is determined in a separate gauge measurement directly before each atom trapping event. This setup achieves a switching time below 2 $\mu$s. Photons arriving during this time are ignored in the evaluation of the data. The repeatability of the probe power settings is discussed separately for the different types of measured spectra in the following subsections (see also Figs. 5.6 and 5.8).

---

[1] For reasons of simplicity, the power of the impinging probe light is defined as the transmission which would be measured on resonance of the empty cavity. The part of the impinging light which is reflected because of non-perfect geometrical mode matching and impedance mismatch as well as light scattered by the cavity mirrors is not considered.

(a) Sample trace

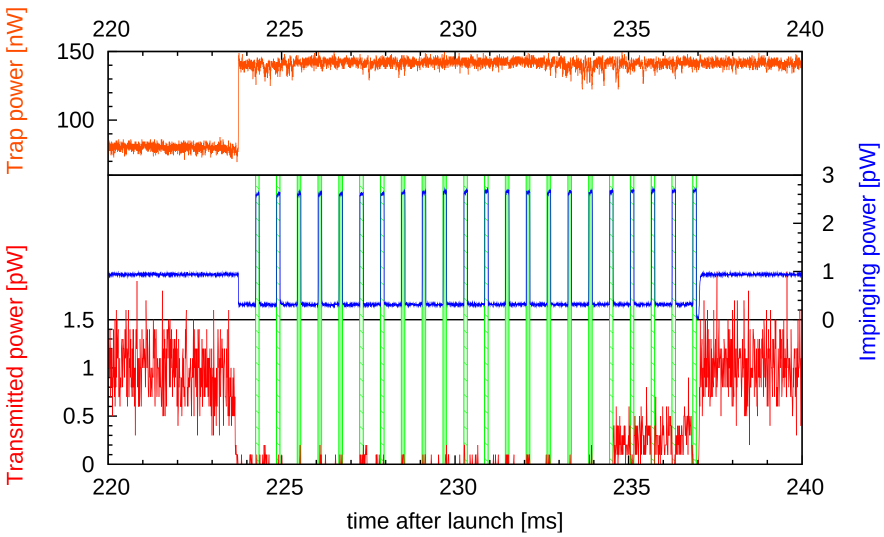

(b) Zoom of (a)

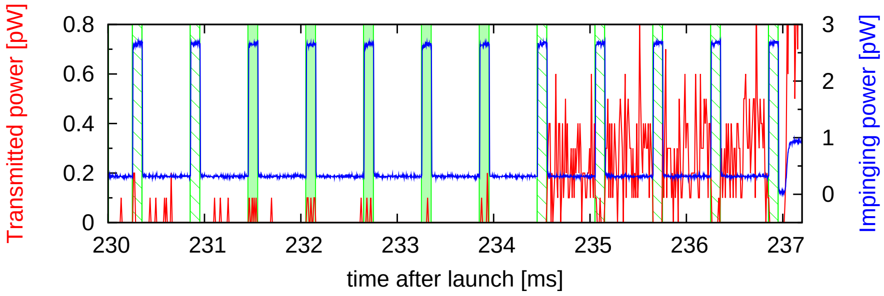

**Figure 5.4: Sample trace** to illustrate the measurement sequence. **(a)** The power of the dipole trap laser (upper panel), the impinging probe power (central panel) and the transmitted probe power (lower panel) are shown. A single slow atom arrives inside the mode at 223.75 ms after launch of the atom cloud, leading to a sharp drop in the transmitted probe light. Detection of this drop triggers an increase of the dipole trap power, trapping the atom. Simultaneously, the measurement cycle is started with a check interval (impinging probe intensity reduced from 1 pW to 0.3 pW). After 500 $\mu$s, the probe intensity is increased to 2.6 pW and $\Delta_c$ is switched from 0 to $-2\pi \times 22$ MHz for 100 $\mu$s. The sequence of probe and check intervals is repeated. The probe intervals are additionally marked by hatched boxes. At 234.5 ms, the atom leaves the trap, visible in the increased transmission during the check intervals. **(b)** A zoom of the transmitted power shows that, if the atom is well-coupled (postselection criterion: $g < 0.6 g_0$), more photons arrive during the probe intervals (which then coincide with a normal-mode resonance). The intervals postselected for further evaluation are shaded.

### 5.2.2 Diagonal scan

The first type of spectrum, which is supposed to show the location of multiphoton transitions with respect to the normal modes of the system, requires a diagonal scan in the ($\Delta_a$,$\Delta_c$)-plane (see Fig. 3.1). The sequence starts with the parameters $(\Delta_{a,0}, \Delta_c) = 2\pi \times (35, 0)$ MHz. In the dipole trap, the atomic transition is Stark shifted, so that $\Delta_a < \Delta_{a,0}$; the exact value depends on the location of the atom in the trap. The average Stark shift $2S$ as a function of the trap depth is calibrated by the position of the normal-mode peaks in the spectrum (see section 6.1.2); it is about $2\pi \times 0.14$ MHz/ nW. For a trap depth of 170 nW, the atom detuning is therefore shifted to $\Delta_a \approx 2\pi \times 11$ MHz. To measure along a diagonal line in the ($\Delta_a$,$\Delta_c$)-plane, the probe frequency $\omega_l$ is modified during the probe intervals, which in turn changes $\Delta_a$ and $\Delta_c$ in parallel (see Fig. 5.5(a)). Technically, detuning $\omega_l$ only requires a change in the frequency of one AOM and is therefore done fast. During all check intervals, $\omega_l$ is reset to the initial value. Accordingly, the postselection criterion on how many atoms are maximally allowed during a check interval is uniform across the whole spectrum. For a complete spectrum, many individual measurements need to be combined. These measurements provide a large set of data, and thus require statistical evaluation. As an example, we choose data from a spectrum which is analyzed in detail in section 6.1.2 (taken for a probe power of 1.4 pW and a trap depth of 170 nW). This data set contains 400 000 probe intervals stemming from $\approx$ 13 000 trigger events in total, and between 5 000 and 25 000 probe intervals for each individual probe detuning. A statistical analysis of this data set is shown in Fig. 5.6, where histograms of the distribution of the impinging probe light, as well as the transmitted probe light before and after the postselection are given for the probe intervals (Fig. 5.6(a)) and the check intervals (Fig. 5.6(b)). The impinging power (first panels in Fig. 5.6) shows a Gaussian distribution around central values of 1.45 pW (probe interval) and 0.3 pW (check interval) with a standard deviation of 5%. The transmitted power clearly shows a bimodal distribution during the check intervals (central panel in Fig. 5.6(b)), representing two types of events: the first set shows a transmission of $\approx$ 300 fW, which matches the impinging power; these events indicate there was no atom inside the cavity. For the second data set, the transmission drops to a low value, indicating the atom was present. These two sets are clearly separated; in about 93% of all check intervals the transmitted power was either larger than 230 fW or smaller than 50 fW. For two regions of detunings ($-20$ MHz $< \Delta_c/2\pi < -10$ MHz and 2 MHz $< \Delta_c/2\pi <$ 10 MHz), only few strongly coupled atoms exist. These are the regions of strong cavity heating near the normal-mode resonances.

With regard to the probe intervals of this data set, the most apparent feature is the Lorentzian transmission peak of the empty-cavity resonance centered at $\Delta_c = 0$, which reaches a maximum of $\approx$ 1400 fW, equivalent to the impinging power. The base of this peak is shown in the central panel of Fig. 5.6(a). Only a small subset of events is visible at small intensities below the empty-cavity peak. With the help of the postselection procedure, this peak can be almost totally suppressed; the remaining probe intervals show the double-peak structure of the normal modes (lower

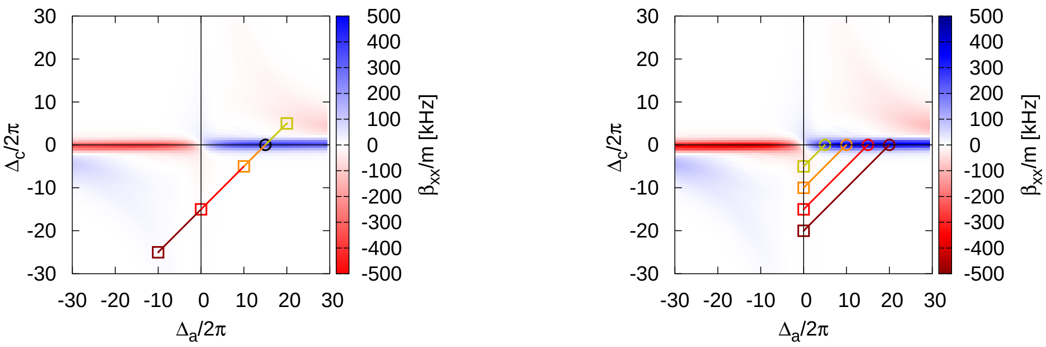
(a) Diagonal scan

(b) Vertical scan

**Figure 5.5: Illustration of scanning procedures.** The detunings during a check interval (circles) and during a probe interval (squares) are shown for four points out of a diagonal and a vertical scan in the ($\Delta_a$,$\Delta_c$)-plane. Notice that only $\omega_l$ can be switched rapidly; this corresponds to diagonal jumps between probe and check intervals in this frame of reference. **(a)** For all points on a diagonal scan, the check intervals are performed at identical parameters; only the detunings during the probe intervals differ. **(b)** In a vertical scan, each scanning point has its own combination of probe and check detunings. The underlying illustration shows the position of cooling regions (blue) and heating regions (red), expressed in terms of the friction coefficient $\beta_{xx}$ (cp. Eq. 4.14), which was averaged over the interval $[-0.24\lambda, 0.24\lambda]$ along the cavity axis. Care has to be taken that the check interval coincides with a cooling region.

panel in Fig. 5.6(a)). The postselection process keeps only those probe intervals for which the surrounding check intervals fall below 9.5 fW, which is equivalent to $0.6g_0$ for the measurement parameters (lower panel in Fig. 5.6(b)).

### Postselection

Different postselection criteria and the resulting averaged spectra are shown in Fig. 5.7. Using the postselection process to select only intervals without atoms present ($0 < g < 0.1g_0$), the Lorentzian transmission curve is obtained. Already a postselection criterion of $g > 0.2$ reduces the averaged probe interval transmission by almost one order of magnitude at $\Delta_c = 0$, and the double-peaked normal-mode structure appears. For a more restrictive postselection, the distance between the normal-mode peaks increases and the two-photon peak becomes better visible, as less well localized atoms are more and more eliminated at the cost of increasing statistical errors.

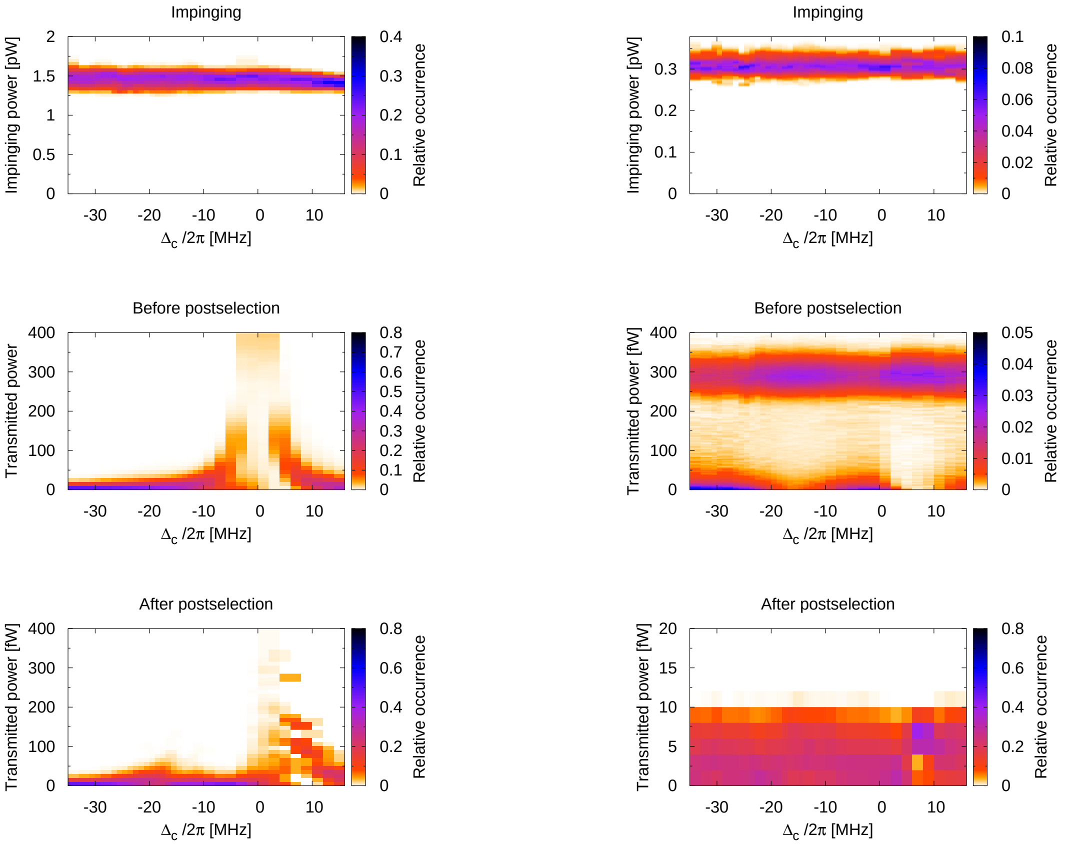

(a) Histogram on probe intervals

(b) Histogram on check intervals

**Figure 5.6: Diagonal scan histograms.** Histogram of the measured impinging probe power and transmitted probe power before and after postselection for the probe intervals **(a)** and the check intervals **(b)**, as a function of the cavity detuning $\Delta_c$. The power distribution is normalized separately for each detuning $\Delta_c$. While the impinging powers are constant for both interval types, the transmitted power during the probe intervals predominantly shows the empty-cavity Lorentzian before postselection; after postselection, this peak is suppressed and a new structure is revealed. The transmitted intensity during the check intervals shows a bimodal distribution with a high transmission level for badly localized or absent atoms and a low transmission level for well localized atoms, the latter intervals being retained during postselection.

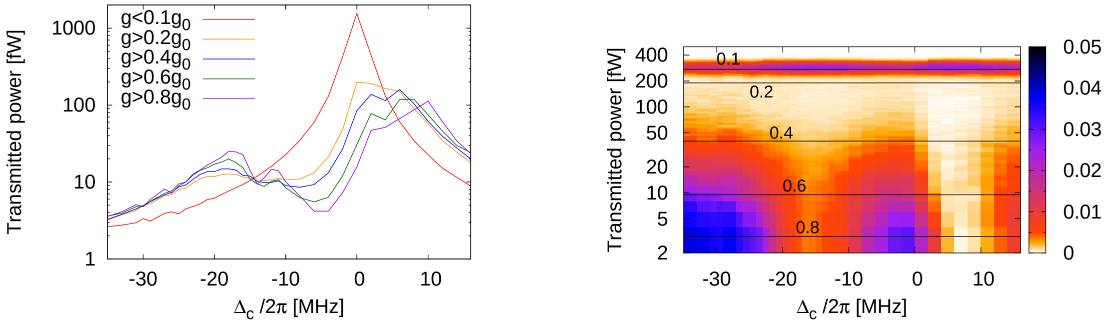
(a) Spectrum for different postselection levels

(b) Postselection levels and check interval histogram

**Figure 5.7: Postselection levels for diagonal scan.** The spectrum obtained from averaging over the transmission during the probe intervals **(a)** strongly depends on the postselection criterion applied to the check intervals **(b)**. For $g < 0.1g_0$, the cavity is predominantly empty and the spectrum accordingly shows the typical Lorentzian resonance centered at $\Delta_c = 0$. For increasing postselection levels $g > (0.2, 0.4, 0.6, 0.8)g_0$, the cavity resonance is more and more suppressed; several different peaks (the normal modes at $\Delta_c = 2\pi \times (-18, 7)$ MHz and a two-photon resonance at $\Delta_c = 2\pi \times (-11)$ MHz) appear.

## 5.2.3 Vertical scan

The second type of spectrum is taken along the direction $\Delta_a = 0$, showing multi-photon transitions while avoiding the normal modes. The intuitive scan parameter for this 'vertical' direction in Fig. 3.2 is the cavity frequency $\omega_c$. However, $\omega_c$ is a function of the cavity length, which cannot be changed quickly due to the inertia of the cavity mirrors. Therefore, switching $\omega_c$ between probe and check intervals is not an option. Instead, for each point in the spectrum a different initial cavity length is chosen, from $\omega_c = \omega_a$ to $\omega_c = \omega_a + 2\pi \times 25$ MHz. For trapping the atom and during the check intervals, $\omega_l$ is then set to $\omega_c$ ($\Delta_c = 0$), whereas during the probe intervals $\omega_l$ is switched such that $\Delta_a = 0$. This method assumes that $\omega_a$, i.e. the average Stark shift, is known, which is true only to a certain extent since this depends on the quality of the localization of the atom in the trap. It follows that the resulting $\Delta_a$ can deviate from 0 by about $\pm 2\pi \times 2$ MHz and thus has to be treated as a fit parameter for comparison to theory. Notice that measurements for $\Delta_c > \Delta_a$ are not possible with this method, since this would lead to strong heating during the check intervals with $\Delta_a < 0$ (see Fig. 5.5(b)).

In Fig. 5.8, the data set for a vertical scan measurement (impinging probe power 3.4 pW, trap depth 140 nW, expected Stark shift $2\pi \times 21$ MHz) is visualized. This data set contains 244 000 probe intervals from 11 600 atoms. As in the previous section for the diagonal measurement, histograms on the distribution of the impinging and transmitted probe power before and after the postselection are shown (probe intervals in Fig. 5.8(a), check intervals in Fig. 5.8(b)). While the impinging power is independent of the cavity detuning for the probe intervals (upper panel in Fig. 5.8(a)), it shows a slight variation in the check intervals (upper panel in Fig. 5.8(b)), which repeats itself in the transmitted intensity (central panel in Fig. 5.8(b)). This is due to a systematic error in the gauge of the input intensity. Before postselection, the transmitted intensity during the probe intervals clearly shows the empty-cavity Lorentzian (central panel in Fig. 5.8(a)), which is suppressed after postselection with the criterion $g_{max} < 0.6g_0$ (lower panel in Fig. 5.8(a)). A systematic increase of the transmission near $\Delta_c = 0$ is present, although hardly visible; in this context, also notice the nonlinear progression of the postselection border in the check intervals (lower panel of Fig. 5.8(b)), which drops to 0 at $\Delta_c = -2\pi \times 3$ MHz. This will be explained in the next paragraph.

#### Postselection

In each point of the vertical scan a different atom detuning $\Delta_a$ is set during the check intervals. This has to be accounted for in the postselection procedure, since the drop in transmission is not only a function of $g$, but also of $\Delta_a$ (cp. Eq. 2.23a). The allowed number of photons during a check interval has to be adapted accordingly. For example, while for a coupling of $0.5g_0$ and a detuning of $\Delta_a = 2\pi \times 25$ MHz ($\Delta_c = 0$), one expects 27 photons on average during one check interval, for $\Delta_a = 0$ the expected photon number is only 0.5. Considering shot noise in the photon detection, this means that this postselection mechanism is not suitable to distinguish between 'strong' and 'very strong' coupling near $\Delta_a = 0$, exactly in the region where the empty-cavity resonance is met during the probe intervals. This leads to a systematic increase in the observed spectra for probe interval detunings $|\Delta_c| < 2\pi \times 3$ MHz, where couplings below $0.5g_0$ cannot be distinguished anymore. This could be remedied by increasing the power during the check intervals, but with the disadvantage of higher heating rates.

In Fig. 5.9, different postselection levels and the resulting averaged probe transmission are shown[2]. The Lorentzian empty-cavity spectrum is obtained for a postselection level of $g < 0.1g_0$. The spectrum obtained for $g > 0.6g_0$ is further evaluated in section 6.1.3.

### 5.2.4 Photon statistics

As mentioned in section 5.1.4, the photons emitted by the cavity are detected by two SPCMs in a Hanbury-Brown–Twiss configuration, and the photon arrival times are recorded by a fast two-channel time-digitizer card. This setup allows to evaluate the photon statistics of the light by correlating the photon arrival times of the two detectors: we evaluate the count rate $R_{12}(\tau, \delta t)$ of photons arriving at the two detectors with a time lag of $\tau$ by dividing each probe interval of length $\Delta t$ into short time bins $\delta t_i$ with start time $t_i$ and duration $\delta t$. Then, for each click of detector 1 in time bin $\delta t_i$ we count the coincident clicks of detector 2 in time bin $\delta t_i + \tau$ ($\tau$ has to be an integer multiple of $\delta t$). The coincidences coming from all possible start

---

[2] These postselection criteria are calculated under the assumption that the average Stark shift due to the dipole trap is $2S = 2\pi \times 19$ MHz.

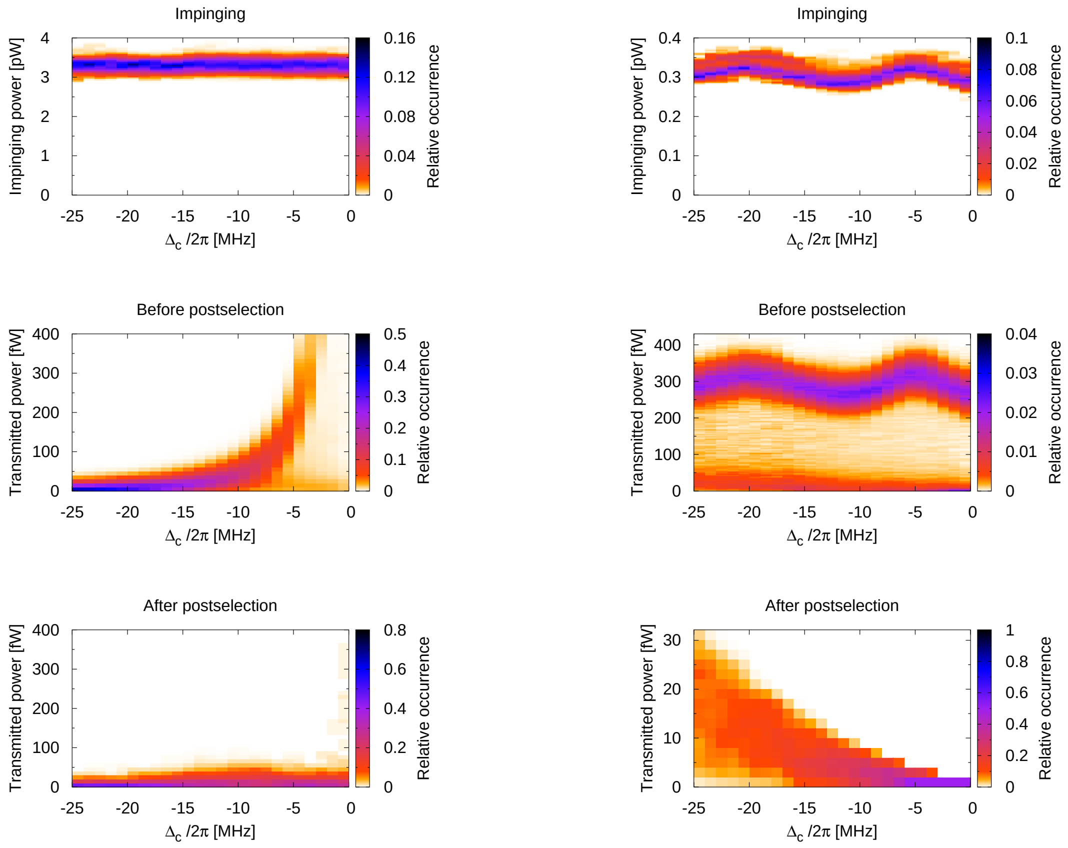

(a) Histogram on probe intervals

(b) Histogram on check intervals

**Figure 5.8: Vertical scan histograms.** Histogram of the impinging and transmitted probe power before and after postselection for the probe intervals **(a)** and the check intervals **(b)**, as a function of the probe-interval cavity-detuning $\Delta_c$. The power distributions are normalized separately for each detuning $\Delta_c$. While the impinging powers are largely constant for both interval types (the slight modulation in the upper panel of (b) can be ascribed to a systematic error in the power gauge), the transmitted power during the probe intervals predominantly shows the empty-cavity resonance before postselection. After postselection, a new, smaller resonance appears. The transmitted intensity during the check intervals shows a bimodal distribution with a high transmission level for badly localized or absent atoms, which are removed during the postselection process, and a low transmission level for well localized atoms. Notice that for a vertical scan, a level of constant coupling is associated with decreasing transmission as the cavity detuning approaches zero (see also Fig. 5.9(b)).

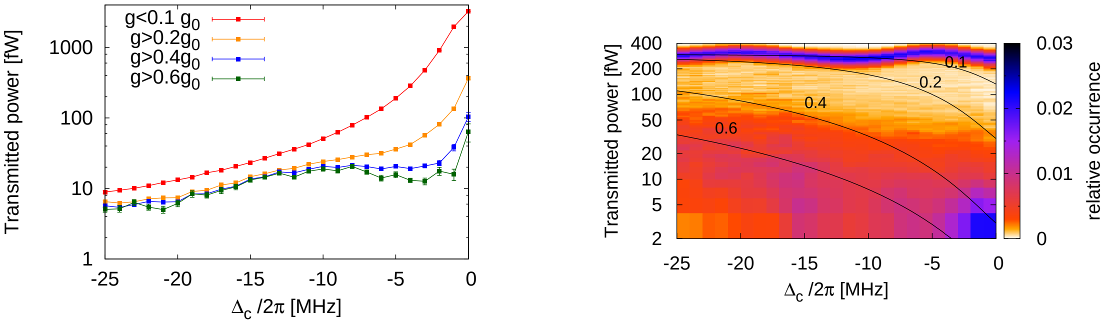

(a) Spectrum for different postselection levels

(b) Postselection levels and check interval histogram

**Figure 5.9: Postselection levels for vertical scan.** Averaged probe interval transmission **(a)** for different postselection critera **(b)**. For this scan direction, the postselection intensity (i.e. the transmitted intensity during a check interval for which $g \gtrless xg_0$) is a nonlinear function of the detuning $\Delta_c$. For $g < 0.1g_0$, the resonance of the empty cavity is observed. For increasing postselection levels $g > (0.2, 0.4, 0.6)g_0$, the cavity resonance is more and more suppressed and the remaining signal is due to the broad multiphoton resonance.

time bins $\delta t_i$ of all probe intervals in the sample are summed, and normalized to the total number of time bins in all probe intervals:

$$R_{12}(\tau, \delta t) = w(\tau) \frac{\sum_{\text{probe intervals}} \sum_i \text{Coinc}(\delta t_i, \tau)}{\sum_{\text{probe intervals}} \Delta t / \delta t} \tag{5.1}$$

Additionally, one must consider that it is less probable to see coincidences for larger correlation times $\tau$, since fewer suitable pairs of time bins exist within one probe interval due to its finite length. This is taken into account by the weighting factor [112]

$$w(\tau) = \frac{1}{1 - |\tau| / \Delta t} \tag{5.2}$$

With the independent count rates of each detector $D_j, (j \in \{1, 2\})$

$$R_j(\delta t) = \frac{\sum_{\text{probe intervals}} \sum_i \text{Clicks } \mathrm{D}_j(\delta t_i)}{\sum_{\text{probe intervals}} \Delta t / \delta t} \tag{5.3}$$

the normalized intensity correlation function can be calculated:

$$g^2(\tau) = \frac{R_{12}(\tau, \delta t)}{R_1(\delta t) R_2(\delta t)} \tag{5.4}$$

This normalization is only valid for a sample of probe intervals which are measured under the same conditions, i.e. the same detuning and the same probe intensity.

# Chapter 6

# Observation of multiphoton transitions

This chapter concentrates on the presentation and discussion of the measurement results. The transmission spectrum of the strongly-coupled atom-cavity system is analyzed for different intensities and scan directions, and the intensity correlation of the spectroscopy data is briefly discussed.

## 6.1 Spectroscopy of the coupled atom-cavity system

As the benchmark of strong coupling is the occurrence of the normal-mode splitting, the spectroscopic observation of this single-photon effect is recapitulated first. Next, the spectroscopy of the system is extended to additionally reveal evidence of multiphoton transitions in a diagonal scan which allows to see a single- and a two-photon transition side by side, and in a vertical scan in which higher-order transitions are excited almost exclusively. The data is compared to the different cavity-QED theories which have been introduced in detail in chapters 2, 3 and 4.

### 6.1.1 Normal modes

The normal-mode spectrum of the atom-cavity system is a consequence of the avoided crossing of cavity and atomic resonance which occurs if the atom is strongly coupled to the light mode. Thus, the resonances change their character from cavity-like to atom-like or vice versa if the atom-cavity detuning $\Delta_{ac}$ is modified. In this system, only the cavity mode is pumped as well as probed; therefore the amplitude of a normal-mode resonance mirrors the projection of the corresponding eigenstate onto the cavity-like contribution, leading to an unbalanced height of the two normal modes if atom and cavity are non-degenerate. This is visible in Fig. 6.1(a), where the avoided crossing appears in the expectation value of the intracavity photon number of the pumped atom-cavity system (cp. Eq. 2.23a) as a function of the detunings $\Delta_a$ and $\Delta_c$. Fig. 6.1(b) shows a measured scan across the normal modes (data points) for four different atom-cavity detunings around $\Delta_a = \Delta_c$. The interchange between the atom-like and the cavity-like character of the normal-mode peaks is clearly visible. The atom-cavity detuning $\Delta_{ac}$ is modified by changing the depth of the dipole trap and consequently the Stark shift of the atomic resonance frequency. The solid lines are the results of numerical simulations based on the single-photon limit (cp. chapter 4). This limit is valid for the low pump power (0.3 pW) which has been used in these measurements. More details on these measurements and simulations can be found in [18, 108].

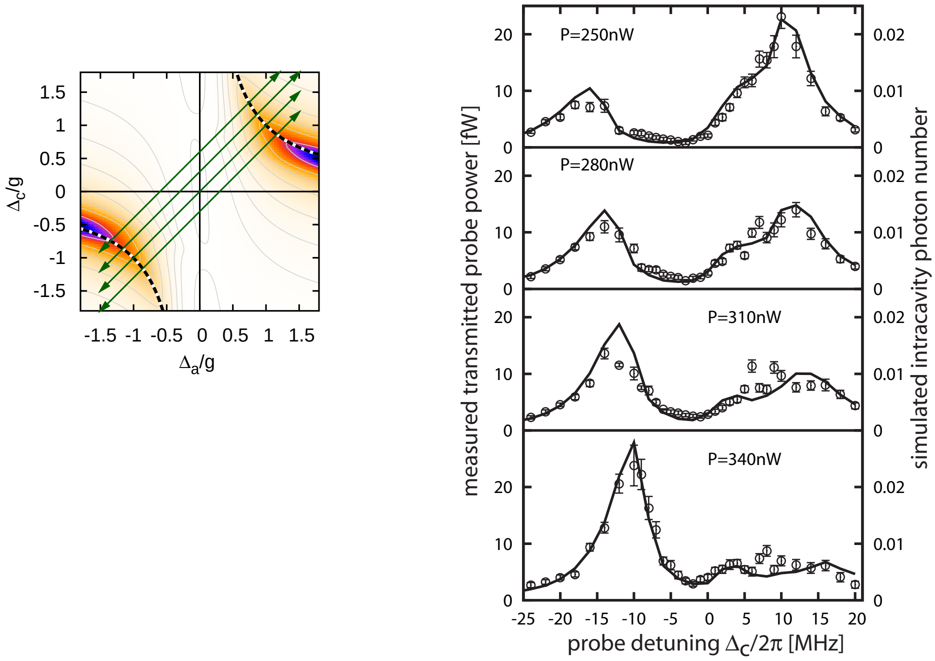
(a) Avoided crossing

(b) Normal-mode resonances

**Figure 6.1: Avoided Crossing for low intensities and normal-mode spectra.** **(a)** shows the avoided crossing between the atom- and cavity resonance as a function of $\Delta_c$ and $\Delta_a$, for a pump power $P_{pump} = 0.3$ pW. The contours are isolines for transmitted powers of $(0.1, 0.5, 1, 2, 5, 10, 20, 50)$ fW. The diagonal arrows indicate the scan direction for the normal-mode spectra shown in **(b)**. The solid lines in **(b)** are the result of numerical simulations.

### 6.1.2 Normal modes and multiphoton transitions

In order to resolve the state $|2,-\rangle$ in addition to the normal modes in the spectrum of the coupled atom-cavity system, measurements have been done at higher intensities and for an atom-cavity detuning $\Delta_{ac} \approx g$, where the distance between the resonances of states $|1,-\rangle$ and $|2,-\rangle$ surpasses their individual widths (cp. Fig. 3.1(b)).

### First observation of the two-photon transition

Diagonal spectra of the atom-cavity system (cp. sections 3.2, 5.2.2) were taken for two different trap depths with two different probe powers each. In detail, the parameters were

- Parameter set (*i*):

$$\Delta_{a,0} = 2\pi \times 35 \text{ MHz}; \; P_{dip} = 140 \text{ nW}; \; P_{pump} = (0.5, 2.5) \text{ pW}$$

- Parameter set (*ii*):

$$\Delta_{a,0} = 2\pi \times 35 \text{ MHz}; \; P_{dip} = 170 \text{ nW}; \; P_{pump} = (0.5, 1.5) \text{ pW}$$

The resulting spectra are shown in Fig. 6.2. In a 2D-plot above the measured data, the location of the scan parameters in the ($\Delta_a$,$\Delta_c$)-plane is indicated with respect to the position of the single-, two- and three-photon resonances. Both scans are in the regime $\Delta_a \gg \Delta_c$, since the Stark shift induced by these trap depths is not enough to compensate for the bare-atom detuning of $\Delta_{a,0} = 2\pi \times 35$ MHz. For the parameter set (*i*), the effective detuning $\Delta_a$ is larger and thus the asymmetry is more pronounced. This is visible in the low-intensity scans of each parameter set, with normal-mode spectra consisting of a small atom-like resonance (state $|1,-\rangle$) on the left and a higher cavity-like resonance (state $|1,+\rangle$) on the right. The peak of the latter resonance is not shown due to poor statistics in this region, where the heating rates are high (cp. Fig. 6.3). For an increased pump intensity, an additional peak on the right of state $|1,-\rangle$ appears in both spectra (upper scans in Fig. 6.2). Two immediate remarks about these new peaks can be made when comparing the two spectra: first, the distance between the atom-like normal mode and the new peak decreases with reduced asymmetry of the spectrum; second, the height of the new peak increases (notice the higher pump intensity in parameter set (*i*)). This behavior is expected for the resonance $|2,-\rangle$ and is a good indication that this peak is indeed the first direct observation of a two-photon resonance. A quantitative evaluation of the spectra follows in the rest of this section, after a short discussion on the spectra of loss rates.

### Loss rates

Scanning across a resonance involves changes of forces and diffusion coefficients. The velocity-dependent force may change from cooling to heating or vice versa, the rate of spontaneous photon emission by an atom increases in parallel to its excitation probability on a peak in the spectrum, and also diffusion due to fluctuations of the atomic polarization or the cavity field are enhanced. All these effects influence the heating rate which the atom experiences in the trap and thus influence the storage time. Fig. 6.3 displays the loss rates of atoms from the trap during the measurement of the spectra in Fig. 6.2. The loss rates are greatly enhanced in the area of the normal modes, which is mostly due to an increase in the diffusion

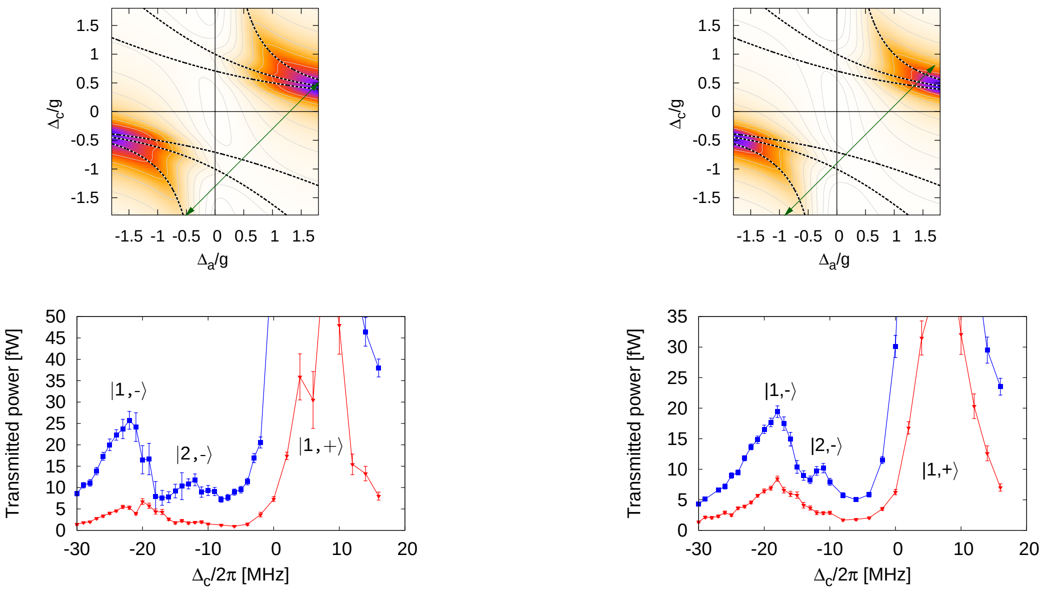
(a) Parameter set ($i$)

(b) Parameter set ($ii$)

**Figure 6.2: Diagonal scan spectra for two different parameter sets**. The scan direction of parameter sets ($i$,$ii$) is indicated and the resulting measured spectra are displayed. The lower-intensity spectra of each parameter set show a distinct normal-mode splitting (states $|1,-\rangle$ and $|1,+\rangle$). In both higher-intensity scans, an additional resonance appears in the space between the normal-mode peaks; this is the first signature of a two-photon transition to the state $|2,-\rangle$.

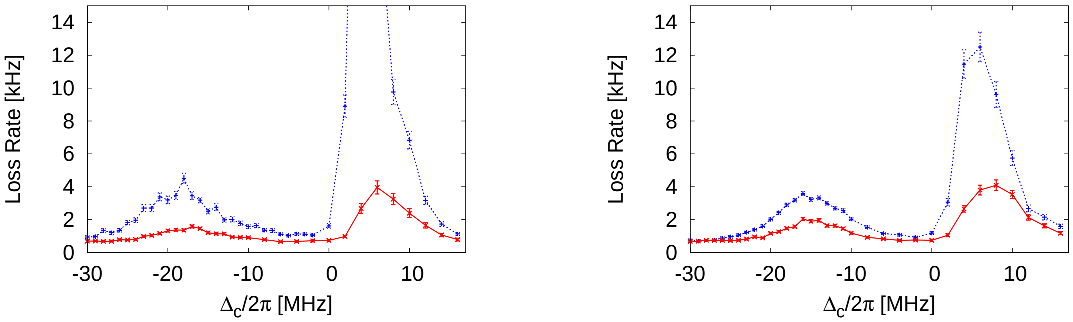
(a) Parameter set ($i$)

(b) Parameter set ($ii$)

**Figure 6.3: Loss rates.** The rate at which an atom got lost from the trap during a probe interval while measuring the spectra in Fig. 6.2 also reveals a normal-mode like structure due to the frequency-dependent friction and diffusion coefficients. Owing to the width of the resonances, single- and two-photon effects cannot be resolved separately.

coefficient due to dipole force fluctuations, as shown in [18, 113]. Especially, the loss rates on the cavity-like normal-mode peak are very high (with atoms being trapped for less than one probe interval on average for the high-intensity spectra), which is why data-collecting on these resonances is extremely difficult, and statistics in the transmission spectra are low. The resonance of the atom-like normal-mode peak in the loss spectrum is so broad that contributions of higher-order transitions cannot be resolved here.

### Comparison of the transmission spectra to a fixed-atom theory

In a basic model of the atom-cavity system, the atom is assumed to be fixed at a specific location, ideally at an antinode of the mode. This model was described in detail in chapter 2. The assumption of an immobile atom is not justified in this setup due to residual oscillations of the atom in the trap. Moreover, the probe mode and the dipole trap mode dephase along the cavity axis, so that the antinodes of the dipole light, where the atoms are localized, do not necessarily coincide with antinodes of the probe light. Still, the fixed-atom theory can be used to approximate the system if the coupling $g$ and the atom detuning $\Delta_a$ (as function of the Stark shift) are taken as independent fit values to incorporate these delocalization effects. At first, the fixed-atom multiphoton theory (section 2.2.3) is used to fit the spectra of Fig. 6.2. The resulting curves are shown in Fig. 6.4 for all four measured spectra, and the fit results are listed in table 6.1. In addition, the fixed-atom single-photon theory (2.2.1) is plotted for the same parameters in order to visualize the influence of multiphoton transitions on the theory spectra. This influence is small as long as the probe power is low. Only for the higher-intensity spectra both theories deviate, and the multiphoton theory describes the measured data more successfully. A detailed discussion for both parameter sets follows.

**Parameter set $(i)$:** Both the low- and high-intensity spectrum of parameter set $(i)$ are reasonably well approximated by the fixed-atom theory. Especially, the position of the resonance $|2,-\rangle$ with respect to the position of the normal-mode resonances is reproduced. However, notice that the fit values $(g, \Delta_a)$ are not identical for the two intensities. For an input power of 0.5 pW, the fitted coupling corresponds to 72% of the maximal possible value ($g = 0.72 g_0$) and the fitted ac Stark shift amounts to $2S = 2\pi \times 22$ MHz or $S = 0.75 S_0$. For the higher-intensity scan, the fit values correspond to $g = 0.7 g_0$ and also $S = 0.7 S_0$[1]. Both average coupling and average Stark shift are reduced for the higher-intensity scan, which leads to the assumption that the atom is more delocalized due to stronger heating (notice that the probe intensity differs by a factor of 5 between the two scans). This is consistent with the fact that the storage time of the atoms in the trap is reduced for higher probe intensities (see Fig. 6.3).

---

[1] Since the atom is localized in the dipole trap, the average coupling to the dipole mode $g_{dip}$ (see sec. 4.1) always exceeds the average coupling to the probe mode $g$. However, notice that the coupling to the dipole mode enters into the Stark shift quadratically ($S \propto g_{dip}^2$), so that $S/S_0 < g/g_0$ is possible.

**Parameter set (*ii*):** For this parameter set, matching the multiphoton fixed-atom theory to the shape of the measured spectra is more difficult; the best match to both low- and high-intensity spectra occurs for an average coupling and ac Stark shift of $(g = 0.7g_0, S = 0.7S_0)$. Here, one set of fit parameters describes the peak positions of both intensities. This might be due the fact that the probe power is only increased by a factor of 3, which means that the heating rates differ less than in the first parameter set. Again, the position of the additional resonance $|2,-\rangle$ is well approximated by the fit. However, the most striking disagreement in this fit lies in the peak height of the normal-mode $|1,-\rangle$, which is severely overestimated by the fixed-atom theory in both high- and low-intensity spectra, whereas the amplitude of the two-photon resonance is underestimated. While this tendency is also visible for parameter set (*i*), it is much more pronounced here. Per se, the fact that the strongest disagreement between fixed-atom theory and data occurs on the normal-mode peak is not surprising, since here the heating rate reaches a local maximum (see Fig. 6.3) and therefore effects of motion are also strong. One should keep in mind that due to the variation of heating rates across the spectrum, the coupling and ac Stark shift of a set of atoms can take different average values for each detuning, and to use only one set of $(g, \Delta_a)$ to describe the entire spectrum is a simplification. By assuming a reduced coupling on the normal mode, the decreased peak height would be explained; moreover the normal-mode resonance would broaden on the right slope, since a reduced $g$ also reduces the splitting between the two normal modes and thus shifts this peak to the right. This can cause an offset in the region of the two-photon transition which raises the spectrum and thus lets the two-photon peak appear higher. However, a reduction in $g$ generally coincides with a reduced ac Stark shift, moving the normal-mode peak to the left. Therefore, a qualitative interpretation of the details of the measured spectra is hard. Instead, numerical simulations which include the motion of the atom are performed to explain the shape of these spectra.

### Numerical simulations of the transmission spectra

The simulations which are used to numerically model atomic trajectories under the given experimental conditions were introduced in chapter 4. For each individual trajectory, the steady-state expectation value of the intracavity photon number $\langle a^\dagger a \rangle$ is calculated repeatedly and then averaged over each probe and check interval. This information is used to apply the same postselection procedure as in the experiment; also statistical fluctuations of the detected photon number due to shot noise are taken into account for the qualification process.

Numerical simulations of the spectra of parameter set (*ii*) have been performed on the basis of the classical, semiclassical and quantum cavity-QED models. Before the simulation results are presented, a few general remarks applying to all simulations in this chapter are given:

**Choice of simulation parameters:** Consistently for all simulations, the correspondence (1 intracavity photon $\equiv$ 1 pW transmitted power) is used for both probe

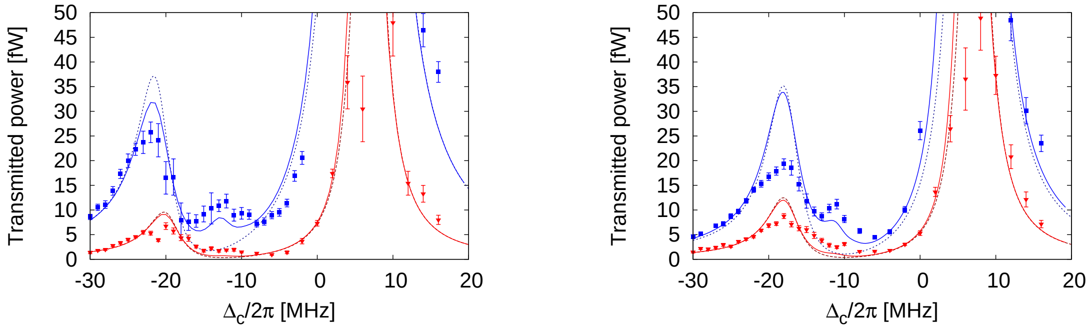

(a) Parameter set (*i*)

(b) Parameter set (*ii*)

**Figure 6.4: Comparison to fixed-atom theories.** Diagonal scan results (data points) compared to the fixed-atom theory including only single-photon transitions (dashed lines) and including higher-order transitions (solid lines). The normal-mode peaks can be described by both theories, the additional peaks are predicted only by a multiphoton theory. For parameters, see table 6.1.

| Parameter set | (i) | | (ii) |
|---|---|---|---|
| $P_{dip}$ | 140 nW | | 170 nW |
| $P_{pump}$ | 0.5 pW | 2.5 pW | 0.5 pW / 1.5 pW |
| $g/(2\pi$ MHz$)$ | 11.5 | 11.2 | 11.2 |
| $\Delta_a/(2\pi$ MHz$)$ | 13 | 15 | 10.5 |
| Freq$(\lvert 1,-\rangle)/(2\pi$ MHz$)$ | -19.7 | -21.0 | -17.6 |
| Freq$(\lvert 2,-\rangle)/(2\pi$ MHz$)$ | -12.0 | -12.5 | -11.0 |
| Freq$(\lvert 2,+\rangle)/(2\pi$ MHz$)$ | 5.5 | 5.0 | 5.7 |
| Freq$(\lvert 1,+\rangle)/(2\pi$ MHz$)$ | 6.7 | 6.0 | 7.1 |

**Table 6.1: Fit results for diagonal spectra.** Results of a parameter fit of the fixed-atom multiphoton theory to the scan data, see Fig. 6.4, and resulting positions of the resonances according to Eq. 3.2. Notice that contrary to parameter set (*ii*), for parameter set (*i*) no common fit parameters can be found which simultaneously describe the position of the resonances for both probe intensities. This is probably due to the larger difference in the localization, resulting from a larger difference in the heating rates between the low- and high-intensity scan (cp. Fig. 6.3). Reasonable fits are obtained within a band of ($g \pm \delta_g$, $\delta_g/2\pi \approx 0.3$ MHz, $\Delta_a \pm \delta_a$, $\delta_a/2\pi \approx 1$ MHz.)

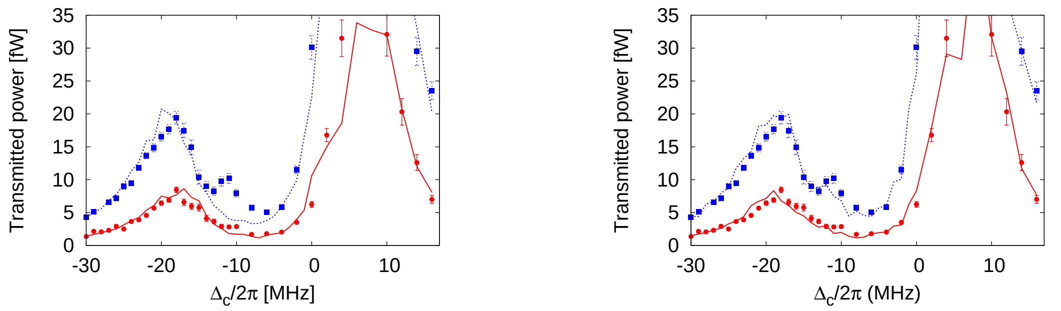
(a) Single-photon transitions

(c) Multiphoton transitions

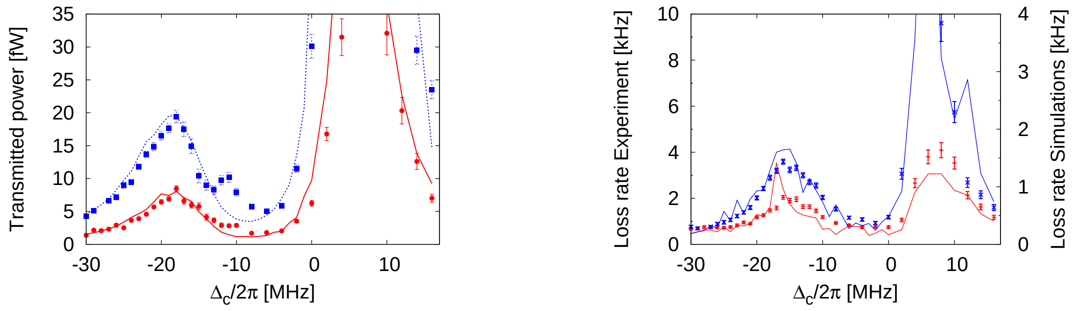
(b) Optical bistability theory

(d) Loss rates - multiphoton transitions

**Figure 6.5: Measured spectra compared to moving-atom simulations based on different theory models.** In **(a)**, the spectra of parameter set ($ii$) are compared to simulations based on a theory including only single-photon transitions, in **(b)** the data are compared to simulations based on the semiclassical theory of optical bistability. Both theories reproduce the normal mode peaks, but clearly disagree with the data in the region of the two-photon peak. This peak is only reproduced with the quantum multiphoton theory, displayed in **(c)**. The simulations were done with (a) 170 000, (b) 160 000, and (c) 165 000 photons in the dipole trap mode.
In **(d)**, the measured loss spectra (points) are compared to the loss rates obtained from the multiphoton simulations (lines). Globally, the loss rates predicted by the simulations are too small by a factor of about 2.5 (see left and right scale); however, the shapes of the spectra are reasonably well reproduced by the simulations. The loss rates obtained from the other types of simulations look similar and are not shown here.

light and dipole trap light. This gives good agreement with the measurements and comes close to the experimentally determined value of 0.9 photons/pW (which is the gauge used for the fixed-atom theory). The origin of the discrepancy is not clear; it might be due to an asymmetric loss coefficient of the two cavity mirrors. The position of the normal modes in the simulated spectra is very sensitive to the exact number of photons in the trap; already a change of 3% in the trap depth leads to a noticeable displacement of the normal modes. It is found that for each theory, a slightly different trap depth was needed to reproduce the obtained position of the normal modes, which is explained by the different forces and thus different localizations in each theory. The trap depth is the only parameter which was fine-tuned separately for each theory to optimize the agreement between simulations and experiment, and the finally used trap depths lie within a band of (±5%) of each other. Notice that each set of low- and high-intensity spectra was simulated with exactly the same parameters, with the natural exception of the probe power $P_{pump}$. The other slight adjustment which is made from experiment to simulations is the choice of the postselection level. It is found that simulated spectra with a postselection level of ($g > 0.5g_0$) match the measured spectra with a postselection level of ($g > 0.6g_0$). This indicates that in overall, the atoms are better localized in the simulation than in the experiment, perhaps because technical heating present in the experiment is not included in the simulations. The fact that the dipole trap storage times of simulated atoms always exceed the measured ones (see Fig. 6.5(d)) supports this assumption. In general, the simulations show consistently good agreement with the experiment, with minor deviations between simulation parameters and parameters of the experiment.

**Discussion of the results:** The simulated spectra are compared to the experiment in Fig. 6.5. The classical simulations including only the single-photon transitions were done for a trap depth corresponding to 170 000 trap photons and are displayed in Fig 6.5(a). Both normal modes in the low- and high intensity scan are well reproduced by these simulations. This proves that the difference in peak height between the measured normal modes and the fitted fixed-atom theory (Fig. 6.4) is a consequence of the atomic motion. The major disagreement between this simulation and the data lies, as expected, in the additional resonance which is experimentally observed in the high-intensity scan but not present in the simulation. The spectra obtained from the semiclassical theory (Fig. 6.5(b)), done with a trap photon number of 160 000, closely resemble the single-photon spectra and also lack any signal in the region of the two-photon transition. Only if the quantization of the light field is taken into account together with the quantization of the atom (simulations done with 165 000 photons in the trap), not only the normal modes but also the additional resonance is reproduced (Fig. 6.5(c)). This proves that this resonance is indeed caused by a two-photon transition.

These spectra allow to verify position of the multiphoton resonance with respect to the normal modes, but they show the quantum two-photon resonance as a small feature in close proximity to the essentially classical normal-mode resonance. While it is possible to better separate these resonances by increasing the atom-cavity detuning $\Delta_{ac}$ and thus increasing the asymmetry of the spectra, this also leads to a further decrease in the amplitude of the quantum resonance as its character becomes more atom-like, and thus it can be pumped less efficiently via the cavity. To further evaluate the multiphoton transitions, we therefore switch to the vertical scan direction.

### 6.1.3 Exclusive excitation of multiphoton transitions

By changing the scan direction from diagonal to vertical in the ($\Delta_a$,$\Delta_c$)-plane (section 3.2), the normal modes can be suppressed. If the cavity detuning is scanned from negative values $\Delta_c \ll 0$ to $\Delta_c \cong 0$ while the atom detuning is kept constant at a value $\Delta_a \gtrsim 0$, the normal modes are avoided; at the same time, the higher states are sufficiently cavity-like in order to be pumped reasonably well. In this way, a spectrum is obtained in a parameter regime where all theories based on a classical field predict only a small, off-resonant background while all observed resonances are explained by a quantized system.

Again, series of scans were performed with two different parameter sets, labeled (*iii*) and (*iv*). The scan procedure was presented in chapter 5.2.3. The initial atom detuning $\Delta_{a,0}$ and the trap depth were chosen such that the resulting Stark-shifted atom detuning $\Delta_a$ is expected to lie close to zero, with the Stark shift caused by the trap being known from the previous measurements. Since the amplitude of the multiphoton resonances is expected to rise with intensity, four different input powers $P_{pump}$ were used. In detail, the parameters were:

- Parameter set (*iii*):

  $$\Delta_{a,0} = 2\pi \times 21 \text{ MHz};\ P_{dip} = 170 \text{ nW};\ P_{pump} = (0.5,\ 1.5,\ 2.4,\ 3.3) \text{ pW}$$

- Parameter set (*iv*):

  $$\Delta_{a,0} = 2\pi \times 21 \text{ MHz};\ P_{dip} = 140 \text{ nW};\ P_{pump} = (0.5,\ 1.5,\ 2.4,\ 3.3) \text{ pW}$$

The resulting spectra are shown in Fig. 6.6, together with transmission curves obtained from the different fixed-atom theories.

### Transmission spectra and fit to fixed-atom theory

In both series of spectra in Fig. 6.6, the transmission signal of the lowest-intensity scans is nearly flat as compared to the higher-intensity scans, where a peak appears and grows as the input power is increased. As indicated in the upper panels, this is the region where resonances of the states $|2,-\rangle$ and $|3,-\rangle$ are expected. Comparing the scans of both parameter sets, it is found that for parameter set (*iii*) the resonance appears farther to the right, and with a higher amplitude. This is consistent with the fact that the dipole trap power is higher for these scans and thus the atom detuning $\Delta_a$ is smaller.

As a first approach, the match between these spectra and a fixed-atom theory is investigated. Since for a classical light field no resonances are predicted in this parameter regime, only the quantum multiphoton theory is considered. The fit values are the coupling $g$ and the atom-detuning $\Delta_a$, which are assumed to be independent of the input power within one parameter set. We find that in order to obtain a good agreement between data and theory, a third fit parameter is required: an offset which depends on the input power but not on the detuning. The origin of this additional offset lies in the atomic motion, as will be shown later. All fit parameters for both parameter sets (*iii*) and (*iv*) are summarized in table 6.2. For parameter set (*iii*), the fitted coupling amounts to $g = 0.7g_0$, and the effective Stark

| Parameter set | (iii) | | | | (iv) | | | |
|---|---|---|---|---|---|---|---|---|
| $P_{dip}$/ nW | 170 | | | | 140 | | | |
| $P_{pump}$/ pW | 0.5 | 1.5 | 2.5 | 3.5 | 0.5 | 1.5 | 2.5 | 3.5 |
| $g/(2\pi$ MHz) | 11.2 | | | | 11.5 | | | |
| $\Delta_a/(2\pi$ MHz) | $-1$ | | | | $+1$ | | | |
| offset/fW | 1.8 | 3 | 3 | 3 | 0.8 | 1.5 | 2 | 2.5 |
| Freq($\|2,-\rangle$)/($2\pi$ MHz) | $-10.7$ | | | | $-12.0$ | | | |
| Freq($\|3,-\rangle$)/($2\pi$ MHz) | $-7.7$ | | | | $-8.4$ | | | |

**Table 6.2: Fit results for vertical spectra.** Results of the parameter fit of the fixed-atom multiphoton theory to the scan data, see Fig. 6.6, and resulting position of the resonances according to Eq. 3.2. Reasonable fits are obtained within a band of ($g \pm \delta_g, \delta_g/2\pi \approx 0.3$ MHz, $\Delta_a \pm \delta_a, \delta_a/2\pi \approx 1$ MHz.)

shift is $2S = 2\pi \times 22$ MHz or $S \equiv 0.62 S_0$, leading to $\Delta_a = -2\pi \times 1$ MHz.[2] For parameter set (*iv*), the fit values are $(g, \Delta_a) = (0.72 g_0, 2\pi \times 1 \text{ MHz})$ or $(S = 0.69 S_0)$. We find that the parameter set with higher absolute transmission shows smaller coupling and Stark shift, which indicates a higher heating rate (see Fig. 6.7). The fitted offset lies in the range of 0.8 to 3 fW, small with respect to the peak heights in the high-power spectra.

In general, the observed peak heights and widths match the prediction of the fixed-atom theory for the given fit parameters. The largest deviation between data and theory is found at small detunings $|\Delta_c| < 2\pi \times 3$ MHz, where the transmission increases due to a systematic error in the postselection procedure, as explained in section 5.2.3. From this theory, it is apparent that the observed resonances are mainly caused by an excitation of the state $|2,-\rangle$. The state $|3,-\rangle$ has a minor contribution which starts to grow at higher intensities, leading to the two-peak structure of the theory spectra. The closeness of the two- and three-photon resonance prevents their separate resolution in the measurement. Contributions of even higher states would appear still closer to the state $|3,-\rangle$, raising transmission around this peak, but are expected to be small for the chosen input powers.

Fitting of the measured spectra to theories with a classical light field does not yield a reasonable result, since no peak is expected in these theories. However, for illustration of the difference between the theories, the respective spectra have been calculated with the fit parameters obtained from the quantized theory (including the phenomenological offset), and are presented together with the data and the multiphoton theory in Fig. 6.6.

### Loss spectra

The loss spectra for the measurements of parameter sets (*iii*) and (*iv*) are shown in Fig. 6.7. For both series of spectra, the loss rate is uniform across all measured detun-

---

[2] Since $\Delta_a$ is slightly negative, a single-photon resonance can occur, in contrast to the stated aim of suppressing this leading order. However, this resonance is expected to appear at a detuning of $\Delta_c < -2\pi \times 100$ MHz, far out of the scanning range used for this measurement

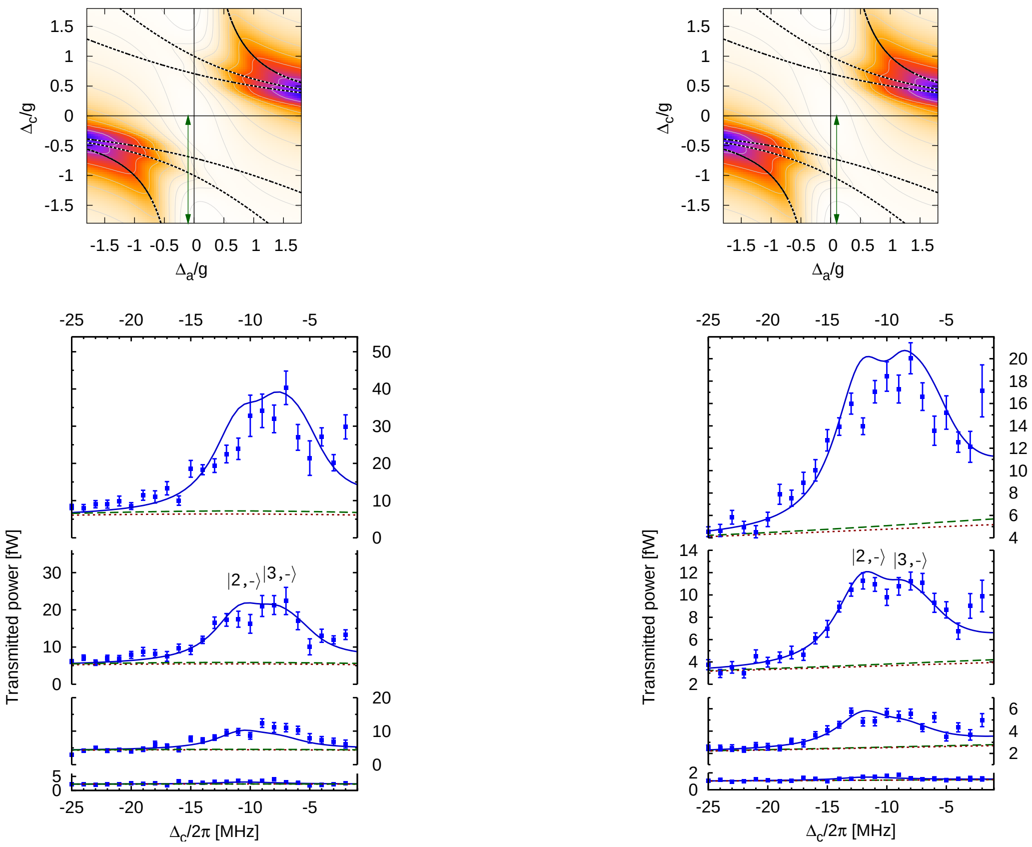

(a) Parameter set (*iii*)

(b) Parameter set (*iv*)

**Figure 6.6: Vertical scan results compared to the fixed-atom quantum theory.** The measurement results for two series of vertical scans for the parameter sets (*iii,iv*) (data points) reveal a resonance which rises with growing input intensity. The data are well described by a fit to the fixed-atom multiphoton theory (solid lines), whereas the fixed-atom single-photon theory (dotted lines) and bistability theory (dashed lines) do not predict a resonance (for fit parameters, see table 6.2).

ings as long as the input power $P_{pump}$ is low. As the input power increases, the loss rate grows only slowly for large detunings $\Delta_c/2\pi < -15$ MHz, but faster for a band of frequencies around the multiphoton resonances $-15$ MHz $< \Delta_c/2\pi < -3$ MHz. For both parameter sets, these resonances appear at approximately the same position as the resonances in the transmission spectra, and also with approximately the same width. Notice that the loss rates are generally higher for parameter set (*iii*), which also shows higher transmission than parameter set (*iv*) (see Fig. 6.6). In the spectrum for the highest input power of $P_{pump} = 3.3$ pW of this parameter set, a relatively narrow peak is visible at about $\Delta_c/2\pi = -6$ MHz (Fig. 6.7(a)), which might be caused by friction and diffusion forces in connection with state $|3,-\rangle$. Of all parameters in the spectra, here this state is occupied most. The expectation value of the atomic excitation probability also reaches its maximum of only 6% at this detuning, according to the fixed-atom theory.

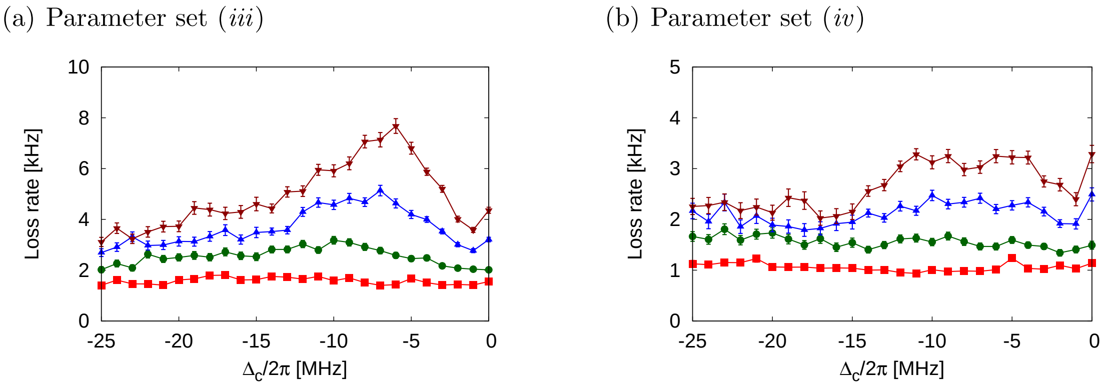
(a) Parameter set (*iii*)

(b) Parameter set (*iv*)

**Figure 6.7: Loss rates.** The spectra of loss rates for the measurements of parameter set (*iii*) and (*iv*) are displayed for increasing pump powers $P_{pump}$ (from bottom to top). For growing $P_{pump}$, a peak in the loss rate appears at the frequency of the multiphoton transitions $|2,-\rangle$ and $|3,-\rangle$, indicating enhanced diffusion.

## Numerical simulations

Numerical simulations based on the three previously discussed theories were performed for parameter set (*iv*) to investigate the influence of atomic motion on the spectra. Details regarding performance and technical implementation of the simulation routines were described earlier, therefore only the details specific to this run are discussed here. For all simulation runs shown in Fig. 6.8, the photon number in the dipole trap was set to 140 000 and the bare-atom detuning was set to $\Delta_{a,0} = 2\pi \times 22$ MHz. With respect to the multiphoton quantum theory, it is evident from the analysis of the fixed-atom theory that the state $|3,-\rangle$ contributes to the high-intensity spectra. Therefore at least the four Fock states ($|0\rangle$,$|1\rangle$,$|2\rangle$,$|3\rangle$) need to be included in the simulation to obtain a realistic transmission spectrum. However, permanently calculating all relevant parameters for four Fock states was not possible due to lack of computational power. As a workaround, the atom was propagated within the mode for 20 integration steps using a basis of only three Fock states, assuming the contribution of the fourth Fock state to the total forces acting on the atom would be small. After these steps, a single intermediate step was performed which included the fourth Fock state. The transmission spectrum was then calculated only on the basis of these intermediate steps. In this way, the transmission spectra show signatures of the state $|3,-\rangle$, whereas its contribution to the loss spectra is suppressed; the loss rates are therefore not compared to the simulation.

Fig. 6.8(a) shows the transmission data compared to the results of simulations based on single-photon and multiphoton transitions. The multiphoton simulation is able to reproduce the measured spectra for all intensities. The largest deviation lies in the region of the three-photon transition, where the simulation slightly underestimates the signal. This might be due to the absence of the state $|3,-\rangle$ in the calculation of the force and diffusion coefficients, or from the disregard of contributions from the states $|4,-\rangle$ and higher. Apart from this region, the multiphoton simulations correctly predict the signal height across the whole spectrum, without the need of an additional offset which had to be added phenomenologically to the fixed-atom theory. This confirms that this offset is a consequence of atomic motion in the trap.

As expected, the single-photon simulations do not predict any peak for this parameter region, but they do fit the data in the off-resonant region $-25$ MHz $\leq \Delta_c/2\pi \leq -20$ MHz, where contributions of the multiphoton transitions to the spectra are small. This indicates that the single-photon theory is able to reproduce the frequency-independent offset, and that this offset therefore stems from a background of single-photon transitions which is enhanced by motion-induced fluctuations of coupling and Stark shift. Also notice that both types of simulations reproduce the rise of the transmission for $|\Delta_c|/2\pi < 3$ MHz, but only if shot noise is considered in the postselection procedure. This proves that this rise is due to a systematic shot-noise limitation in the postselection procedure, as discussed in section 5.2.3.

The third type of simulations is based on the bistability state equations and shown in Fig. 6.8(b). These simulations are unable to explain the observed resonances in the transmission signal. However, they show an enhanced transmission as compared to the single-photon simulations, especially for the highest-intensity scan. These simulations are more sensitive to variations in the coupling and trap depth, since bistability predicts larger gradients in the transmission as the distance to a normal-mode resonance is reduced. In very rare events, fluctuations can be so large that a bistable region is reached for the highest input intensity, resulting in the small bulge visible in this calculated spectrum. Yet even changing the initial parameters of the simulation considerably, no parameter set was found which could reproduce the measured data. Summarizing, the simulations verify that the observed resonances are multiphoton transitions which can only be explained by quantizing both atom and light field.

## 6.2 Nonlinear intensity response

On a two-photon resonance, quantum theory predicts a mainly quadratic response of the transmission to a change in input intensity, as a consequence of the system's ability to accept only photon pairs (see sec. 3.2.2). Stated differently, the single atom is able to mediate a nonlinear interaction between two photons: the presence of one photon in the input port decides over the transmission or reflection of the second photon.

To see this effect, the following analysis concentrates on the spectra of parameter set (*iv*), where, as compared to parameter set (*iii*), the states $|2,-\rangle$ and $|3,-\rangle$ are better separated and the contribution of the state $|3,-\rangle$ is smaller. The data of parameter set (*iv*) are averaged over two bands of frequencies for each intensity. The first

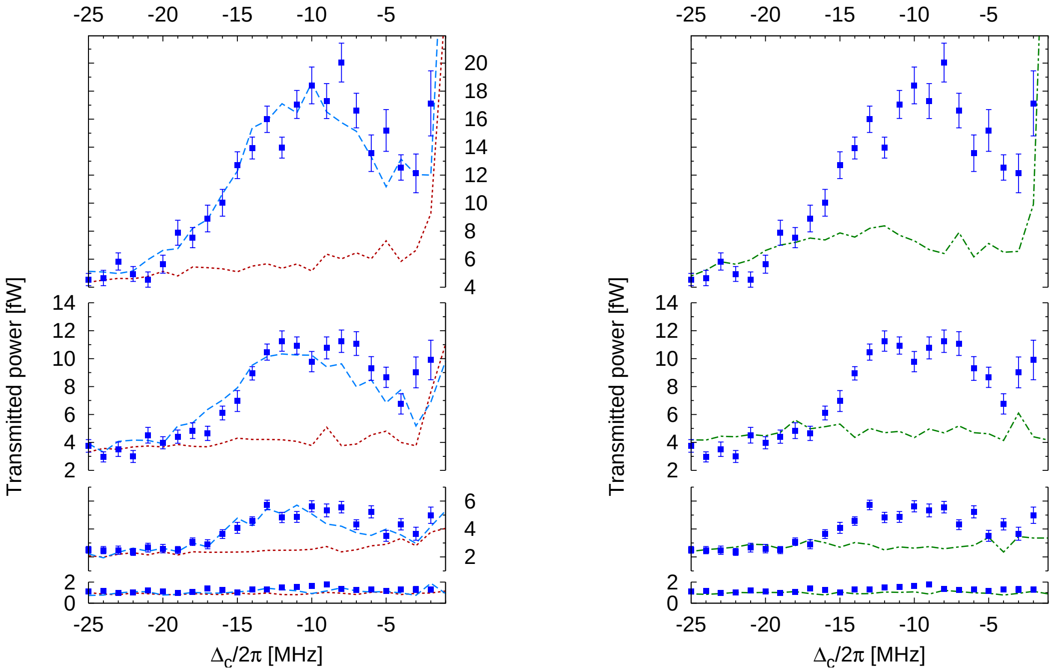
(a) Single-photon and multiphoton theory

(b) Theory of optical bistability

**Figure 6.8: Measured spectra compared to moving-atom simulations based on different models. (a)** The data of parameter set (*iv*) (data points) are only reproduced by simulations which include atomic motion and account for multiphoton transitions (dashed lines), whereas simulations based on single-photon transitions (dotted lines) fail to describe the data. **(b)** Also, simulations based on the theory of optical bistability do not match the measured data. All simulations were done with 140 000 photons in the dipole trap.

frequency band is the region of the two-photon transition, $-15$ MHz $\leq \Delta_c/2\pi \leq -10$ MHz, while the second band $-25$ MHz $\leq \Delta_c/2\pi \leq -20$ MHz serves as a reference for the contribution of single-photon transitions to the signal. The averaged intensities of both bands are plotted in Fig. 6.9(a); obviously the on-resonance transmission increases faster than the off-resonant transmission. The difference between both bands is taken in order to obtain the transmission due to the two-photon resonance. In Fig. 6.9(b), this two-photon transmission is plotted together with an analytical fit function of the form $f(x) = bx^a$, with $x$ in units of [pW]. The fit results are $a = 1.74 \pm 0.08, b = 1.3 \pm 0.1$ fW/ pW. The fit parameter $a$ shows that the dependency of output vs. input power is almost quadratic. In Fig. 6.9(c), the same data are compared to the fixed-atom multiphoton and bistability theory. These theory curves were obtained in the same way as the data points, namely by averaging the theoretically expected transmission of the on- and off-resonance band for different input powers and subtracting the results. The parameters ($g = 2\pi \times 11.5$ MHz) and ($\Delta_a = 2\pi \times 1$ MHz) needed for the calculation were taken from Fig. 6.6(b). The fixed-atom multiphoton theory describes the data well, with the exception of the last data point, which is slightly over-estimated by the theory curve. This deviation

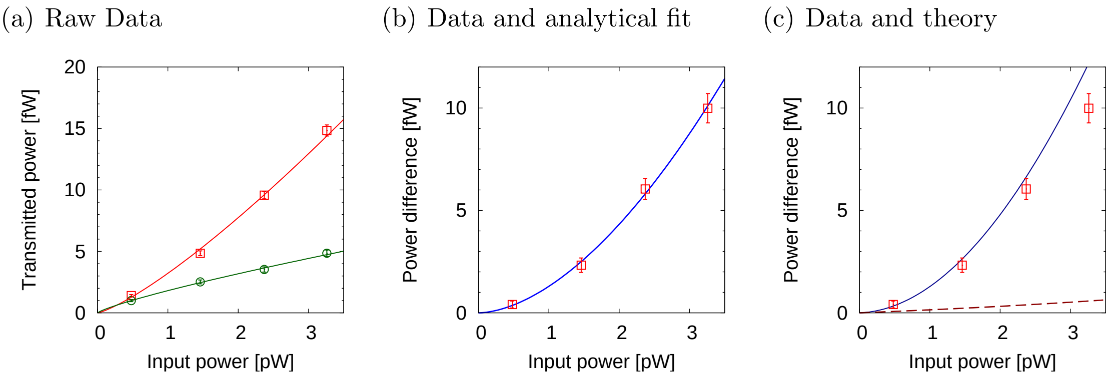
(a) Raw Data

(b) Data and analytical fit

(c) Data and theory

**Figure 6.9: Nonlinear intensity response. (a)** For each input power, the transmission data of parameter set (*iv*) are averaged over two frequency bands, the off-resonant region (circles) and the region of the two-photon transition (squares). The curves are guides to the eye. **(b)** The difference of both bands is compared to an analytical power law fit, showing that output vs. input power scales with an exponent of $(1.74 \pm 0.08)$. **(c)** The data difference is compared to the fixed-atom multiphoton theory (solid line) and bistability theory (dashed line) taken from Fig. 6.6.

is likely to be caused by effects of the motion, which dampen the resonance; this might be remedied by implementing a more efficient cooling protocol [53].
In comparison, the bistability theory shows only a small nonlinearity, as saturation of the atom is low for the chosen parameters: The excitation probability of the atom remains below 5% according to multiphoton fixed-atom theory or 7% according to the multiphoton simulations. Clearly, bistability cannot explain the observed nonlinearity.

## 6.3 Correlation signal

As a last item in the evaluation of the data, the intensity correlation function for different regions in the observed spectra is briefly studied. The extraction of the correlation signal from the measured data was discussed in section 5.2.4; here the focus lies on the discussion of the observed features. In general, there are two fundamentally different reasons for observing structure in the time-resolved correlation function: the first is a consequence of mechanical motion of the atom in the dipole trap, the second stems from the internal structure of the atom-cavity system. These two items are shortly highlighted in the next subsections.

### 6.3.1 Signature of atomic motion

The atom, being localized in the cavity by means of the intracavity dipole trap, performs oscillations within the trap well. Due to the large aspect ratio of the well, the trap frequencies in axial and radial direction differ by a factor of about 70; the axial frequency lies in the range of 300 kHz, the radial frequency on the order of 4 kHz. In the case of moderately large oscillation amplitudes, for example caused by insufficient postselection of well-coupled atoms, these oscillations lead to a periodic variation in the coupling which is large enough to be visible in the transmission signal. The corresponding frequencies then appear in a correlation measurement, leading to strong bunching as shown in Fig. 6.10. The data underlying this figure were taken at high input powers for detunings $\Delta_a \approx \Delta_c = 0$, where the postselection procedure is known to fail (see section 5.2.3). The motion of the atoms is clearly visible in the correlation signal, leading on the one hand to an oscillation on a short timescale, which corresponds to the axial motion, and on the other hand to a decay of the correlation signal on the timescale of the probe interval length, which corresponds to the radial oscillation. A systematic study of these oscillations can be found in [108]. They are suppressed in regions with more reliable postselection.

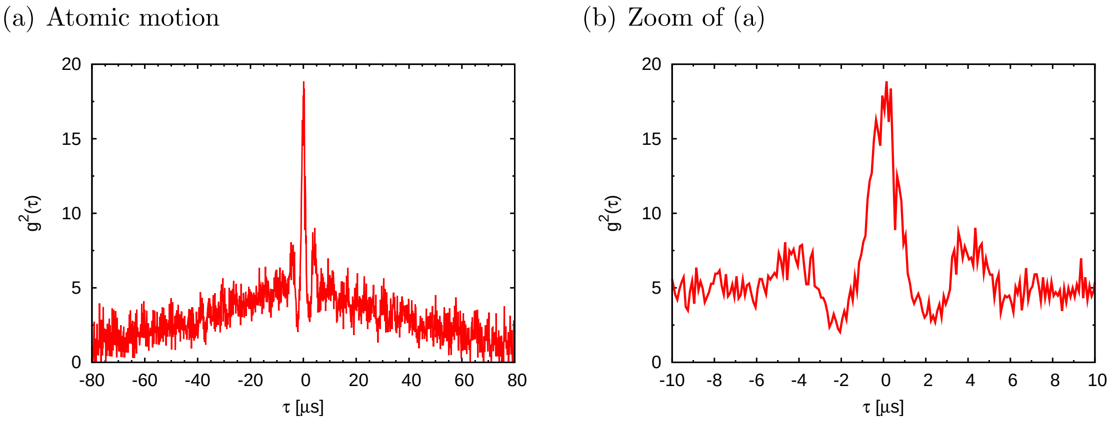
(a) Atomic motion

(b) Zoom of (a)

**Figure 6.10: Trap frequencies.** The correlation signal of the data from parameter set (*iii*) for detuning $\Delta_c = 0$, input power $P_{pump} = 2.4$ pW and a qualification of $g_{min}$=0.3 shows modulation on two timescales: a fast oscillation with a frequency of 250 kHz, which originates from the axial oscillation of the atom in the trap, and a slow decay of the signal on a timescale larger than the probe interval length, which stems from the radial oscillation of the atom in the trap.

### 6.3.2 Signature of photon bunching

A conceptually different source of modulations in the correlation signal is the internal structure of the atom-cavity system: as explained in section 3.2.3, the transmitted photons should be weakly anti-bunched on the normal-mode resonances for our cavity parameters, but strongly bunched in regions where multiphoton transitions can be excited. This behavior can be found in a diagonal scan. Fig. 6.11(a) shows the averaged correlation signal for three bands of detunings in parameter set (*ii*): On the left side of the normal modes ($-25$ MHz $\leq \Delta_c/2\pi \leq -20$ MHz) and near the empty-cavity resonance ($-4$ MHz $\leq \Delta_c/2\pi \leq -2$ MHz), the correlation signal is flat, while a sharp peak at $\tau = 0$ is visible for detunings near the two-photon resonance ($-13$ MHz $\leq \Delta_c/2\pi \leq -6$ MHz). A similar, but better resolved peak occurs when averaging over a band of detunings of ($-8$ MHz $\leq \Delta_c/2\pi \leq -4$ MHz)

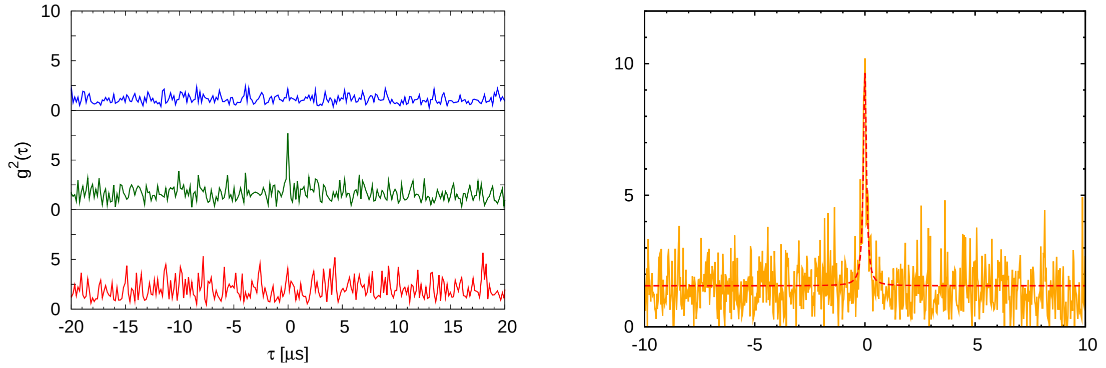

(a) Correlations in a diagonal scan

(b) Correlations in a vertical scan

**Figure 6.11: Photon bunching. (a)** The transmission signal from the measurements of parameter set (*ii*) is evaluated for correlations. Data from different input intensities $P_{pump} = (0.5, 1.5, 2.4, 3.3)$ pW and three bands of detunings $\Delta_c/2\pi$ from $-25$ to $-20$ MHz (upper panel), from $-13$ to $-6$ MHz (central panel), and from $-4$ to $-2$ MHz (lower panel) are gathered. The normalized correlation functions for each subset of detunings and intensities were calculated separately and averaged in the end. Bunching is visible only in the central frequency band, which covers the region of the two-photon transition. **(b)**: Bunching is also pronounced on the three-photon resonance of parameter set (*iii*) for $P_{pump} = 3.3$ pW, averaged over detunings $\Delta_c/2\pi$ from $-4$ to $-8$ MHz. A Lorentzian fit yields a width (HWHM) of $(90 \pm 10)$ ns.

in the parameter set (*iii*) for an input power of $P_{pump} = 3.3$ pW (Fig. 6.11(b)). The height of the peak is in qualitative agreement with the theoretical prediction (Fig. 3.9(b)).

Due to better statistics, the signal-to-noise ratio is sufficient to determine the peak width: By fitting a Lorentzian, a width (HWHM) of $(90 \pm 10)$ ns is obtained, which is on the order of the photon decay time $t_c = (2\kappa)^{-1} \approx 64$ ns and much narrower than the motion-induced bunching discussed in the previous section. Further measurements are required for a more detailed study of these structural correlations.

# Chapter 7

# Outlook

The measurements presented here constitute the first conclusive observation of a two-photon resonance in a single-atom-cavity spectroscopy experiment, confirming theoretical predictions on its characteristic energy and its nonlinear dependence on the probe laser intensity [57, 58]. Simulations based on different theory models demonstrate that the measurements can only be explained within the framework of quantum theory, as these resonances are a unique consequence of the quantized interaction between matter and light. Having shown the accessibility of these resonances, further experiments on their properties as well as possible applications come into reach.

An immediate topic of attention is the analysis of the properties of the transmitted light on a multiphoton resonance. The spectrum of the emitted photons should contain lines of characteristic frequencies stemming from incoherent, step-wise decay via intermediate doublets [67], as well as sets of photons identical to those used for the excitation. Contrary to the normal modes, where anti-bunching of photons occurs, on a two-photon transition the photons should escape the cavity preferably in pairs, leading to strong bunching. First evidence for bunching was found here, inviting for a thorough analysis. The atom mediates a nonlinear interaction between two photons, extending nonlinear optics to the level of single quanta. Utilizing the system as an input filter, it can be set up to transmit only photon pairs of appropriate frequency, functioning as a two-photon gateway. The nonlinearity could moreover be employed to realize a single-photon transistor [122], where the presence or absence of a single 'gate' photon decides over transmission or reflection of a second 'signal' photon. Also, superposition states of transmitted or reflected photons seem possible, which could have applications in optical communication and computation [123, 124] or quantum information science [125, 126]. To assess the efficiency of such a process, the photon escape rate through each of the two possible loss channels - spontaneous emission by the atom or transmission through a mirror - needs to be characterized, and spontaneous emission needs to be minimized by tailoring the system parameters like relative detunings, coupling constant and cavity linewidth.

Besides, this experiment constitutes a step towards the regime of a single atom strongly coupled to a mesoscopic number of photons. Increasing the photon number, optical bistability on the single-atom level is predicted [79], as the system passes the boundary from quantum to semiclassical behavior [69, 127, 128]. This transition will highlight the role of quantum fluctuations and their impact on the evolution of the state, a topic closely related to the occurrence of squeezing [129, 130]. The system offers the chance to observe this boundary, also learning about the back action of measurements on an open quantum system [62, 131] which is conditioned by the measurement process [132]. This has implications for the implementation of quantum feedback protocols [12, 133, 134] as well.

Realizing experiments with mesoscopic intracavity photon numbers is hardly feasible in the present setup because the storage times of the atoms in the resonator are strongly reduced for the necessary pump intensities. This can be remedied by implementing cavity cooling in three dimensions with additional standing-wave dipole traps in directions transverse to the cavity axis [53], which promises storage times of several seconds. However, such a trap configuration cannot be realized at the moment due to the mirror geometry which restricts optical access from the side. Construction of a new cavity with improved optical access [135] has been brought under way in the course of this work, with the aim to replace the present cavity in the foreseeable future. The new cavity will also be suited for implementing a blue dipole trap at a magic wavelength (see appendix B.2), which avoids differential Stark shifts between the ground and excited state of selective Rb-transitions, helping to improve the stability of the system. This modernization of the setup will further increase the spectrum of possible measurements.

# Appendix A

# Background information

## A.1 Mathematical background for numerical calculations

### A.1.1 Solution of the master equation

The state of the atom-cavity system is described by its density matrix

$$\varrho = \sum_{j,k} \zeta_{jk} \left| b_j \right\rangle \left\langle b_k \right| \tag{A.1}$$

which can be expressed as a linear combination of basis vectors $b_j$ from the combined Hilbert space of the system $\mathcal{H}_s = \mathcal{H}_a \bigotimes \mathcal{H}_c = \{\{\left|g,i\right\rangle, \left|e,i\right\rangle\}, i \in \mathbb{N}_0\}$, where $\mathcal{H}_a = \{\left|g\right\rangle, \left|e\right\rangle\}$ is the two-dimensional Hilbert space of the atomic states and $\mathcal{H}_c = \{\left|i\right\rangle, i \in \mathbb{N}_0\}$ is the Hilbert space of the mode. For numerical calculations, this Hilbert space is truncated after a certain number of Fock states $N$, so that the dimension of a basis vector $\left|b_j\right\rangle$ is $2N$ and the dimension of the density matrix is $(2N)^2$. All operators $\hat{o}$ acting on states of the system can be expressed as matrices of the same dimension as the density matrix. In this basis, the master equation 2.14 is a linear matrix equation which has terms of the form $\hat{o}_1 \varrho \hat{o}_2$ stemming from the dissipative parts of the Liouvillian $\mathcal{L}_a, \mathcal{L}_\sigma$. Such a matrix equation can be 'flattened' into a vector equation by using the identity

$$\bar{\varrho} = \hat{o}_1 \varrho \hat{o}_2 \Leftrightarrow \mathrm{vec}(\bar{\varrho}) = (\hat{o}_2^T \otimes \hat{o}_1)\mathrm{vec}(\varrho) \tag{A.2}$$

Here, the sign $\otimes$ indicates the tensor product (also named Kronecker matrix product) of two matrices.[1] and $\mathrm{vec}(\varrho)$ is the vectorization[2] of the matrix $\varrho$. The $(2N)^2$

---

[1] The Kronecker product of two matrices $A = \begin{pmatrix} a_{11} & \cdots & a_{1n} \\ \vdots & \ddots & \vdots \\ a_{m1} & \cdots & a_{mn} \end{pmatrix}$, $B$ is defined as the block matrix $A \otimes B = \begin{pmatrix} a_{11}B & \cdots & a_{1n}B \\ \vdots & \ddots & \vdots \\ a_{m1}B & \cdots & a_{mn}B \end{pmatrix}$.

[2] The vectorization of a matrix is a linear transformation which converts the $m \times n$ matrix A to a column vector of dimension $(mn, 1)$: $vec(A) = (a_{11}, \cdots, a_{m1}, a_{12} \cdots, a_{m2}, \cdots, a_{1n}, \cdots, a_{mn})^T$

eigenvectors $\{\mathrm{vec}(\varrho_\Gamma)\}$ and eigenvalues $\{\Gamma\}$ of the resulting linear vector equation can be calculated by standard mathematical algorithms. The eigenstates $\{\varrho_\Gamma\}$ of the Liouvillian $\mathcal{L}$ are obtained by reshaping the eigenvectors into square matrices.

### A.1.2 Steady state and time evolution

#### Steady state

The steady state density matrix $\varrho_0$ is the solution of the master equation 2.14 for $\dot{\varrho} = 0$:

$$\mathcal{L}\varrho_0 = 0 \tag{A.3}$$

This is the eigenstate of $\mathcal{L}$ with the eigenvalue $\Gamma = 0$.
From this, the steady state expectation value of any system operator $\hat{o}$ is obtained:

$$\langle \hat{o} \rangle_0 = \mathrm{Tr}[\hat{o}\varrho_0] \tag{A.4}$$

#### Time evolution

The time evolution of the density matrix is given by the formal solution of the master equation:

$$\varrho(\tau) = e^{\mathcal{L}\tau}\varrho(0) \tag{A.5}$$

To calculate the time evolution, we follow ref. [64]. At first, we decompose the density matrix into a weighted sum of the eigenstates

$$\varrho(0) = \sum_\Gamma \tilde{c}_\Gamma \varrho_\Gamma \tag{A.6}$$

for which the time evolution is easily computed:

$$\varrho(\tau) = \sum_\Gamma e^{\Gamma\tau} \tilde{c}_\Gamma \varrho_\Gamma \tag{A.7}$$

To evaluate this equation numerically, the coefficients $\tilde{c}_\Gamma$ are also needed. They can be calculated from the 'dual eigenstates' $\tilde{\varrho}_\Gamma$, which obey the duality relation

$$\mathrm{Tr}[\tilde{\varrho}_\Gamma \varrho_{\Gamma'}] = \delta_{\Gamma,\Gamma'} \tag{A.8}$$

With this dual basis, the coefficients $\tilde{c}_\Gamma$ can be calculated:

$$\tilde{c}_\Gamma = \sum_{\Gamma'} \tilde{c}_\Gamma \mathrm{Tr}[\tilde{\varrho}_{\Gamma'} \varrho_\Gamma] = \mathrm{Tr}[\tilde{\varrho}_\Gamma \varrho(0)] \tag{A.9}$$

Notice that the dual eigenstates $\tilde{\varrho}_\Gamma$ are the eigenstates of the dual Liouvillian $\tilde{\mathcal{L}}$ with the same eigenvalues. $\tilde{\mathcal{L}}$ is defined by the relation

$$\mathrm{Tr}[\hat{o}(\mathcal{L}\varrho)] \equiv \mathrm{Tr}[(\tilde{\mathcal{L}}\hat{o})\varrho] \tag{A.10}$$

The dual basis can be considered as the set of left eigenstates of $\mathcal{L}$, whereas the normal basis consists of the right eigenstates. Explicitly, the dual operator $\tilde{\mathcal{L}}$ of the Liouvillian $\mathcal{L}$ from equation 2.14 acts on an operator $\hat{o}$ as

$$\tilde{\mathcal{L}}\hat{o} = \frac{i}{\hbar}[H,\hat{o}] + \kappa(2a^\dagger\hat{o}a - a^\dagger a\hat{o} - \hat{o}a^\dagger a) + \gamma(2\sigma^\dagger\hat{o}\sigma - \sigma^\dagger\sigma\hat{o} - \hat{o}\sigma^\dagger\sigma) \tag{A.11}$$

The dual basis $\{\tilde{\varrho}_\Gamma\}$ can be used to expand system operators similarly to equation A.6:

$$\begin{aligned} \hat{o} &= \sum_\Gamma c_\Gamma \tilde{\varrho}_\Gamma & \text{(A.12)} \\ c_\Gamma &= \mathrm{Tr}[\hat{o}\varrho_\Gamma] & \text{(A.13)} \end{aligned}$$

Now all necessary tools are available to calculate the expectation value of any system operator $\hat{o}(\tau)$ at any time $\tau > 0$. To this end, the time dependence of the operators is noted explicitly:

$$\begin{aligned} \langle\hat{o}(\tau)\rangle &= \mathrm{Tr}[\hat{o}\varrho(\tau)] \\ &= \sum_\Gamma e^{\Gamma\tau}\tilde{c}_\Gamma \mathrm{Tr}[\hat{o}\varrho_\Gamma] \\ &= \sum_\Gamma e^{\Gamma\tau}\tilde{c}_\Gamma c_\Gamma \end{aligned} \tag{A.14}$$

### A.1.3 Calculation of correlation integrals

Also, expectation values of correlations of any two system operators can be calculated from the master equation by invoking the quantum regression theorem [66], which links the time evolution of correlations to the evolution of the density matrix:

$$\begin{aligned} \langle\hat{o}_1(t+\tau)\hat{o}_2(t)\rangle &= \mathrm{Tr}[\hat{o}_1 e^{\mathcal{L}\tau}(\hat{o}_2\varrho(t))] & \text{(A.15a)} \\ \langle\hat{o}_1(t)\hat{o}_2(t+\tau)\rangle &= \mathrm{Tr}[\hat{o}_2 e^{\mathcal{L}\tau}(\varrho(t)\hat{o}_1)] & \text{(A.15b)} \end{aligned}$$

With the help of this theorem, the expectation value of correlations between operators can be reformulated:

$$\begin{aligned} \langle\hat{o}_1(t+\tau)\hat{o}_2(t)\rangle &= \sum_\Gamma e^{\Gamma\tau}\mathrm{Tr}[\hat{o}_1\varrho_\Gamma]\mathrm{Tr}[\hat{o}_2\varrho(t)\tilde{\varrho}_\Gamma] & \text{(A.16a)} \\ \langle\hat{o}_1(t)\hat{o}_2(t+\tau)\rangle &= \sum_\Gamma e^{\Gamma\tau}\mathrm{Tr}[\hat{o}_2\varrho_\Gamma]\mathrm{Tr}[\varrho(t)\hat{o}_1\tilde{\varrho}_\Gamma] & \text{(A.16b)} \end{aligned}$$

This can be used to calculate explicitly the integrals of correlations of the force operator $\mathbf{F} = (F_x, F_y, F_z)^T$ (Eq. 4.8) needed for the friction (Eq. 4.14) and diffusion (Eq. 4.19) tensors:

$$\beta_{ij} = -\,\mathrm{Im}\left(\sum_{\Gamma\neq 0}\frac{2\mathrm{Tr}[\varrho_\Gamma F_i]\mathrm{Tr}[F_j\varrho_0\tilde{\varrho}_\Gamma]}{\hbar\Gamma^2}\right) \tag{A.17}$$

$$D_{dp,ij} = -\operatorname{Re}\left(\sum_{\Gamma\neq 0}\frac{\mathrm{Tr}[\varrho_\Gamma F_i]\mathrm{Tr}[F_j\varrho_0\tilde{\varrho}_\Gamma]}{\Gamma}\right) \tag{A.18}$$

## A.2 Background information on the system

### A.2.1 Experimentally relevant hyperfine levels of rubidium

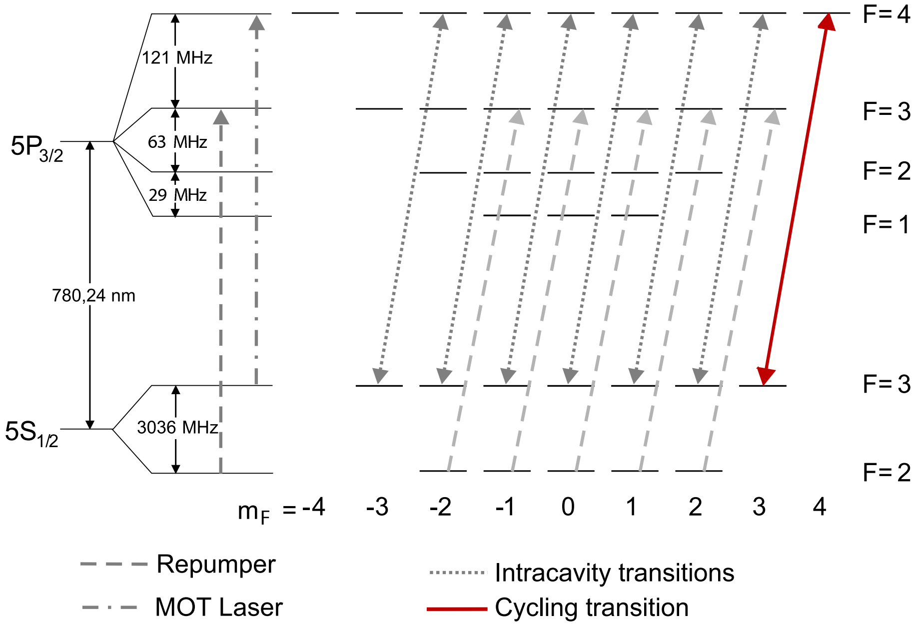

**Figure A.1: Relevant hyperfine levels of $^{85}$Rb.** Hyperfine splitting (*left*) and Zeeman sublevels (*right*) of the $^{85}$Rb levels $^5S_{1/2}$ and $^5P_{3/2}$, showing the MOT and the intracavity transitions. Inside the cavity, the atom is optically pumped into the cycling transition $F = 3,\ m_F = 3 \rightarrow F = 4,\ m_F = 4$.

### A.2.2 Birefringence of the cavity

In the theory of the atom-cavity system, the Rubidium atom is treated as a particle with two internal states. In reality, the fine- and hyperfine splitting (cp. Fig. A.1) of the levels has to be taken into account, and the two-state approximation is only valid if the atom is optically pumped into the cycling transition $^5S_{1/2}F = 3, m_F = 3 \rightarrow {}^5P_{3/2}F = 4', m_F = 4'$ by circularly polarized light. Initially circularly polarized light can become elliptically polarized due to birefringence of the cavity mirrors. Birefringence occurs if a material possesses different refractive indices for polarizations along two orthogonal main axes. Crossing the medium, orthogonal linear polarizations accumulate a phase shift and thus circular polarization is not preserved. This also means that the cycling transition is no longer closed and the atom can be pumped into other hyperfine levels. These levels would have to be considered in the atom-cavity theory. Moreover, if the atom is pumped into other than the outermost hyperfine levels, a decay channel into the $F = 2$ ground state is opened. After such a decay, the atom would no longer couple to the cavity mode and thus appear to be lost. Measuring the atomic loss rate in dependence of the

polarization of the probe light is therefore a way to estimate the degree of circular polarization ($DOCP$) of the probe light inside the resonator.
The polarization of the probe light is set by a quarter wave plate (QWP) in front of the cavity. If $\alpha$ is the angle between the linearly polarized input beam and the fast optical axis of the quarter wave plate, the polarization in front of the QWP is given by

$$\boldsymbol{E} = E_0 \begin{pmatrix} \cos\alpha \\ \sin\alpha \end{pmatrix} \tag{A.19}$$

and behind the QWP it has been transformed to

$$\boldsymbol{E'} = E_0 e^{i\pi/4} \begin{pmatrix} \cos\alpha \\ i\sin\alpha \end{pmatrix} \tag{A.20}$$

Projection on the circular polarization basis

$$\hat{\sigma}_+ = \frac{1}{\sqrt{2}} \begin{pmatrix} 1 \\ -i \end{pmatrix}, \hat{\sigma}_- = \frac{1}{\sqrt{2}} \begin{pmatrix} 1 \\ i \end{pmatrix} \tag{A.21}$$

gives the real coefficients $\mu_+(\alpha), \mu_-(\alpha)$ $(\mu_+(\alpha)^2 + \mu_-(\alpha)^2 = 1)$

$$\mu_+(\alpha) \equiv \langle \boldsymbol{E'}/E_0, \hat{\sigma}_+ \rangle = \frac{1}{\sqrt{2}} (\cos\alpha - \sin\alpha) \tag{A.22}$$

$$\mu_-(\alpha) \equiv \langle \boldsymbol{E'}/E_0, \hat{\sigma}_- \rangle = \frac{1}{\sqrt{2}} (\cos\alpha + \sin\alpha) \tag{A.23}$$

The common phase factor $e^{i\pi/4}$ introduced by the QWP has been neglected. Rotating the QWP allows to manually adjust these coefficients. Fig. A.2 shows a measurement of the loss rate of atoms which are being excited by probe light for different settings of $\alpha$. The loss rate increases quadratically with the coefficient $\mu_-(\alpha)$, i.e. linearly with the intensity of left circularly polarized light. A cross-check with the storage times in the dipole trap without illumination confirms that the enhanced loss rate is due to the change of polarization of the probe light and not due to the change of polarization of the dipole trap, which influences the loss rates only on a much longer timescale.
This measurement allows to estimate the maximal contribution of $\sigma_-$-polarized light in the cavity: Fitting the loss rate with a quadratic curve yields a coefficient $dl\mu \equiv d(loss)/d|\mu_-(\alpha)|^2 = 20.5$ kHz. The minimal loss rate for $\alpha = 0$ is $loss_0 = 0.42$ kHz. This loss rate will be mostly caused by loss mechanisms which are unrelated to the polarization of the light, like diffusion and parametric heating in the dipole trap. However, as a worst-case scenario, let us assume that this loss is totally due to $\sigma_-$-polarized light created by birefringence of the mirrors. In this case, an upper bound for the relative intensity in the wrong polarization mode is obtained:

$$|\mu_-|^2_{\max} = loss_0/dl\mu = 0.02 \tag{A.24}$$

The minimal $DOCP$ is therefore

$$DOCP = \mu_+^2 - \mu_-^2 \geq 0.96 \tag{A.25}$$

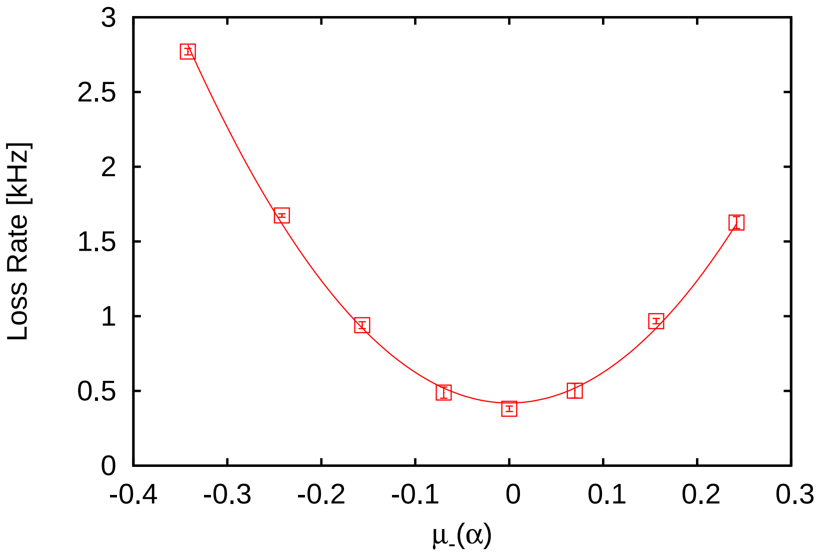

**Figure A.2: Birefringence** The loss rate of atoms illuminated with probe light (points) is a quadratic function (solid fit curve) of the polarization coefficient $\mu_{-}(\alpha)$. The enhanced losses for $\sigma_{-}$-polarized light are a consequence of atomic decay into the hyperfine state $F = 2$, from which atoms are not repumped.

Going back into the basis of light polarized linearly along the two main axes of the birefringent mirrors, one can calculate the frequency splitting between the two polarization modes that would follow from this $DOCP$. Assuming that the birefringence occurs only in the mirror substrate, no mode splitting can be observed since the optical path length within the cavity is identical for both polarization modes. If the birefringence occurs in the mirror coatings, a relative phase shift between the modes is picked up at every reflection. The total accumulated phase shift for $DOCP = 0.96$ is $\Delta\phi = 0.065\pi$, calculated with the relation $DOCP = (1 - |cos(2\Delta\phi)|)/2$. From this, the length of the cavity and the number of reflections which depends on the finesse of the cavity, $\#_r = \mathcal{F}/\pi$, the relative difference in the optical path length can be calculated. This leads to a splitting of $2\pi \times 0.5$ MHz for the polarization modes for the parameters $\mathcal{F} = 490000, L = 123$ $\mu$m. This splitting is smaller than the cavity linewidth $\kappa = 2\pi \times 1.25$ MHz.

Concluding, an upper estimate for the splitting of the polarization modes from an independent storage time experiment confirms that the polarization modes are degenerate well within the cavity linewidth, and that birefringence of the cavity mirrors can be neglected in the present setup.

# Appendix B

# Alternative dipole traps

The dipole trap used for the presented measurements (see section 4.1) is generated by the excitation of a far-red detuned cavity mode, which attracts atoms in the ground state towards a region of high intensity. This trap imposes a Stark shift of nearly equal magnitude but opposite sign on ground and excited state and thus changes the atomic transition frequency. Fluctuations in the trap depth lead to modulations in the resonance frequency of the atom, parametric heating and a broadening of the measured resonances; furthermore restrictions on the maximal size of the Stark shift limit the trap depth and the accessible parameter regimes, as regions of cavity-induced heating may not be crossed during the loading process. These difficulties can be avoided by choosing different trap configurations: in a blue-detuned dipole trap, the atom is stored at a position of vanishing light intensity, and in a 'magic wavelength' trap, ground state and excited state experience an identical Stark shift and so a differential light shift is avoided. The blue trap has already been realized in this setup [20] and is presented in the first section of this chapter; the second section concentrates on a discussion and a possible implementation of a magic-wavelength trap.

## B.1 Blue dipole trap

A blue dipole trap consists of a potential landscape with a point of vanishing light intensity, completely surrounded by blue-detuned light which repells the atom. Such a landscape can be generated in the cavity by combining modes of different longitudinal and transverse orders. The longitudinal confinement is provided by a $\mathrm{TEM}_{00}$ mode at 772 nm, detuned by 3 FSR from the near-resonant probe light; therefore a node of the dipole field coincides with an antinode of the probe field in the cavity center. Radial confinement is added by simultaneously exciting the two $\mathrm{TEM}_{10+01}$ modes of the longitudinal mode series which is two FSR blue detuned from the probe light, at 775 nm. These modes are split by an amount of 6 MHz due to imperfections of the cavity mirrors; by exciting both modes with two laser beams, a standing wave with an effective transverse donought pattern is formed. In the center of the cavity, these doughnuts are aligned with the nodal planes of the blue $\mathrm{TEM}_{00}$ mode, forming closed trap wells which overlap with regions of strong coupling to the probe mode. The alignment of the modes in the cavity center is a consequence of the cavity geometry and therefore inherently guaranteed by the setup. However, the trap wells open as the modes of different longitudinal order dephase further away from the cavity center.

In order to load an atom into a central trap well, the radial confinement has to be opened. A $\mathrm{TEM}_{10}$ mode with a vertically oriented nodal line is used to guide the atoms into the trap. A mode with the required orientation is formed by exciting both $\mathrm{TEM}_{10+01}$ modes with only one laser beam at a frequency between the two resonances. In combination with the blue $\mathrm{TEM}_{00}$ mode, funnels are formed to guide the atom. As the atom moves along the nodal line, it does not gain kinetic energy. When it has been detected via its influence on the transmission of the probe field, the trap is closed by actively switching to the doughnut pattern. Notice that in this configuration only the intensity of the radially confining modes has to be switched, reducing axial heating during the switching. Such heating can occur in the red dipole trap, where it then has to be counteracted by a period of cavity cooling. Atoms which do not manage to enter the blue funnel are rejected, as are further atoms which arrive after the trap containing the first atom has been closed.

The storage time of an atom in the blue trap is comparable to the storage time in the red trap, which is to be expected since the heating mechanisms are similar. In contrast to the red trap, the atom experiences only a minimal Stark shift; from the position of the normal-mode resonances, this residual Stark shift is measured to be on the order of the natural linewidth of the atom. The absence of the Stark shift enables measurements in the dispersive limit, where the presence of an atom can be detected while it scatters only one photon on average. More details on the setup of the blue trap and corresponding measurements can be found in [20, 98, 136].

## B.2 Traps at a magic wavelength

While a blue-detuned dipole trap avoids Stark shifts at the trap center, a differential Stark shift between ground and excited state is still expected if the atom moves. A modification of the transition frequency can only be avoided in a trap at a 'magic wavelength', which shifts ground and excited state by the same amount. This behavior has its origin in the multilevel structure of the atom, as the dipole laser connects the excited state to even higher-lying states. This can lead to an effective negative Stark shift which in certain cases can be tuned to match the Stark shift of the ground state. Such a trap is especially relevant in metrology experiments like atomic clocks at optical frequencies, where differential Stark shifts lead to systematic errors [137, 138, 139]. In a cavity-QED experiment with cesium, a magic wavelength at 935 nm has been used to build a state-insensitive red-detuned intracavity dipole trap [48]. Due to the different level structure in Rb, no red magic wavelength is available at frequencies in the vicinity of the D2-line. However, there are possibilities to implement a blue magic trap. The calculation of the relevant Stark shifts is discussed in the following section.

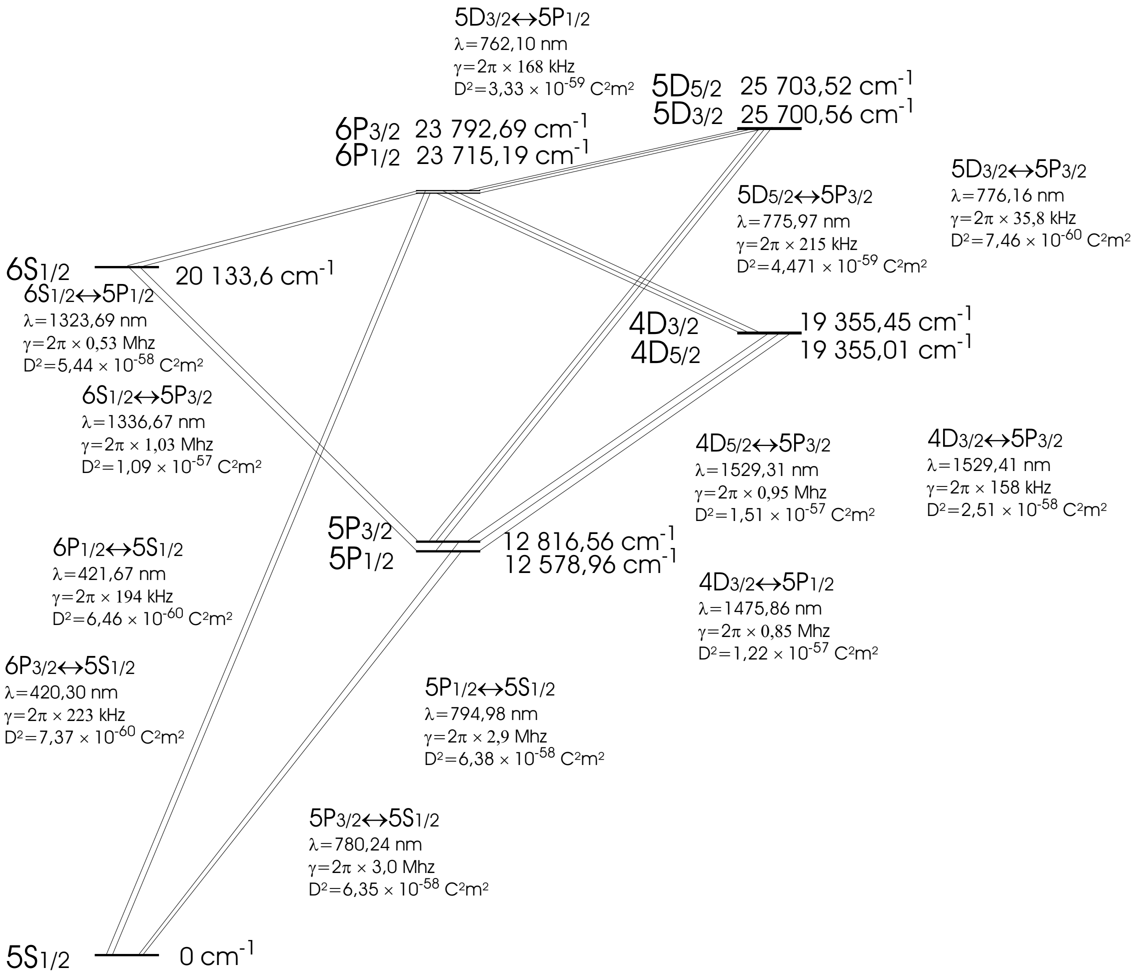

**Figure B.1: Rubidium level structure.** An overview over the most relevant Rb levels and transitions is shown.

Neglecting the hyperfine structure and the polarization of the impinging laser, the ac Stark shift caused by coupling the states $i$ and $j$ via a dipole-allowed transition can be calculated in second order perturbation theory [106]:

$$S_{ij} = \pm \frac{n\omega_l c}{V} \frac{6\pi c^2 \gamma_{ji}}{\omega_{ij}^2(\omega_{ij}^2 - \omega_l^2)} \tag{B.1}$$

where by convention the shift of the lower state is positive and the shift of the upper state is negative. $\omega_{ij}$ is the transition frequency and $\gamma_{ji}$ is the polarization decay rate from the upper state $j$ to the lower state $i$, which is often given in terms of the Einstein A coefficient ($A_{ji} = 4\pi\gamma_{ji}$). $n$ is the number of intracavity photons with the dipole laser frequency $\omega_l$; it can be converted to an intensity by the expression $I = n\hbar\omega_l c/V$, where $V$ is the mode volume of the cavity. The Stark shift is given at an antinode of the field; if required, the spatial dependence can be included by multiplying with the square of the dipole mode function $|\psi_{dip}(\boldsymbol{r})|^2$. Notice that Eq. B.1 goes beyond the rotating-wave approximation, allowing for

| No. | $\lambda$/ nm | $\gamma/(2\pi$ MHz) | transition | comment |
|---|---|---|---|---|
| 1 | 794.98 | 2.86 | $5S_{1/2} \leftrightarrow 5P_{1/2}$ | D1-line |
| 2 | 780.24 | 2.99 | $5S_{1/2} \leftrightarrow 5P_{3/2}$ | D2-line |
| 3 | 1529.3 | 0.166 | $5P_{3/2} \leftrightarrow 4D_{3/2}$ | |
| 4 | 1529.4 | 0.995 | $5P_{3/2} \leftrightarrow 4D_{5/2}$ | |
| 5 | 776.16 | 0.038 | $5P_{3/2} \leftrightarrow 5D_{3/2}$ | |
| 6 | 775.98 | 0.215 | $5P_{3/2} \leftrightarrow 5D_{5/2}$ | |
| 7 | 1366.7 | 1.04 | $5P_{3/2} \leftrightarrow 6S_{1/2}$ | |
| 8 | 630.10 | 0.0423 | $5P_{3/2} \leftrightarrow 6D_{3/2}$ | |
| 9 | 630.01 | 0.251 | $5P_{3/2} \leftrightarrow 6D_{5/2}$ | |
| 10 | 741.02 | 0.350 | $5P_{3/2} \leftrightarrow 7S_{1/2}$ | |
| 11 | 572.62 | 0.0316 | $5P_{3/2} \leftrightarrow 7D_{3/2}$ | |
| 12 | 572.57 | 0.196 | $5P_{3/2} \leftrightarrow 7D_{5/2}$ | |
| 13 | 616.13 | 0.0949 | $5P_{3/2} \leftrightarrow 8S_{1/2}$ | |
| 14 | 543.33 | 0.0226 | $5P_{3/2} \leftrightarrow 8D_{3/2}$ | |
| 15 | 543.30 | 0.132 | $5P_{3/2} \leftrightarrow 8D_{5/2}$ | |
| 16 | 565.53 | 0.0899 | $5P_{3/2} \leftrightarrow 9S_{1/2}$ | |

**Table B.1:** Table of the transitions used for the calculations of the Stark shift on the ground state $5S_{1/2}$ and the excited state $5P_{3/2}$ of the D2-line. The transmission line data have been taken from the data collection of Kuruzc [140].

detunings between dipole laser and atomic transition on the order of the atomic resonance frequency. In the RWA, Eq. B.1 converges to Eq. 4.2.

The hyperfine splitting and the polarization of the dipole laser impose additional selection rules on the dipole transition and influence the transition strength. The combination of the ground state angular momentum $F$ and its projection $m_f$ and the angular momentum of the absorbed photon yields a factor [141, 142]

$$\alpha_{ij} = (2F'+1)(2J'+1)(2F+1)\begin{pmatrix} F & 1 & F' \\ m_f & q & -m'_f \end{pmatrix}^2 \begin{Bmatrix} F' & I_k & J' \\ J & 1 & F \end{Bmatrix}^2 \tag{B.2}$$

where the quantum numbers of the energetically higher-lying state are primed. $q$ denotes the polarization of the light in a spherical basis ($q \in \{-1, 0, 1\}$ corresponds to $\{\sigma_-, \pi, \sigma_+\}$-polarization). The symbols $(\cdot)$ and $\{\cdot\}$ denote the Wigner 3J- respectively 6J-symbol. $I_k$ is the nuclear spin, equal to 5/2 for $^{85}$Rb. The selection rules require $m_f + q = m'_f$.

The total Stark shift of a state $l$ is given by the sum of the Stark shifts imposed by lower-lying and higher-lying states

$$S_l = \sum_{F,m_f}^{i<l} S_{il}\alpha_{il} + \sum_{F',m'_f}^{l<j} S_{lj}\alpha_{lj} \tag{B.3}$$

where the sum runs over the quantum numbers $\{F, m_f\}$ of all lower-lying levels $i$ respectively $\{F', m'_f\}$ of the higher-lying states $j$. The levels which were used for

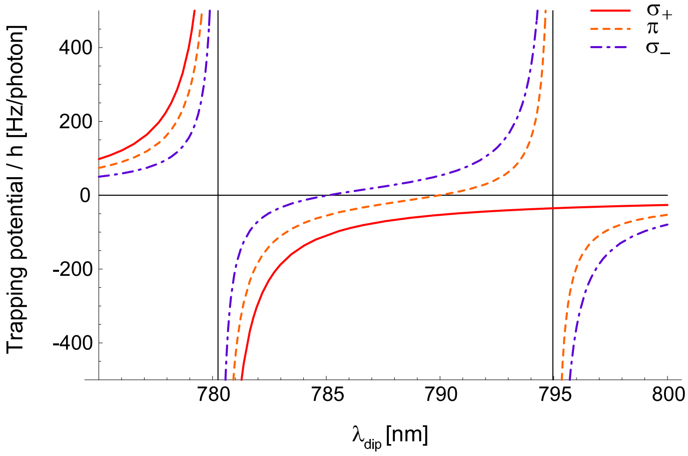

**Figure B.2: Trapping potential for different polarizations.** The trapping potential per trap photon $U_g/n$ for an atom in the ground state $5S_{1/2}F = 3, m_f = 3$ is displayed for different polarizations of the dipole laser. For $\sigma_-$- and $\pi$-polarized light, the potential switches sign between the resonances of the D2- and the D1-line. For $\sigma_+$-polarization, no resonance occurs at $\lambda = 795$ nm and the trapping potential remains negative.

the calculation are listed in table B.1. From the Stark shift, the trapping potential $U_l$ for an atom in state $l$ can be derived by

$$U_l = -\hbar S_l \tag{B.4}$$

For example, in general the ground state of Rb $5S_{1/2}$ couples to the states $5P_{1/2}$ and $5P_{3/2}$ (see Fig. B.1, the coupling to the states $6P_{1/2}$ and $6P_{3/2}$ is neglected due to their large detuning). The ground state is shifted downwards if the wavelength of the dipole laser is slightly larger than 780 nm, but shifted upwards as the wavelength approaches 795 nm. This is displayed in Fig. B.2 for an atom in the outermost hyperfine level $F = 3, m_f = 3$ interacting with trap light of different polarizations. Notice that if the dipole trap is $\sigma_+$-polarized, the selection rules forbid any coupling to the state $5P_{1/2}$, so the trapping potential remains negative for wavelengths near 795 nm.

The excited state $5P_{3/2}$ is repelled by its coupling to the ground state; its trapping potential is largely inverted as compared to the ground-state potential near the resonance of the D2-line (Fig. B.3). In addition, the excited state is Stark shifted if it couples to a higher state. The states $4D_{3/2}$ and $4D_{5/2}$ have the largest influence on trapping potentials for traps with wavelengths in the vicinity of the D2-line. In the context of this experiment, the Stark shift of the Zeeman level $5P_{3/2}F = 4,\ m_f = 4$ is most relevant, as it is the upper state of the intracavity cycling transition. For a $\sigma_+$-polarized dipole trap, as is used at the moment, this state only couples to the state $4D_{5/2}F' = 5,\ m'_f = 5$, which causes a resonance in the trapping potential at a wavelength of 776 nm (Fig. B.3(a)). A zoom into this resonance (Fig. B.3(b)) shows that the potentials of ground and excited state cross at a wavelength of $\lambda_{dip} = 775.8$ nm, providing a candidate for a blue magic wavelength which could

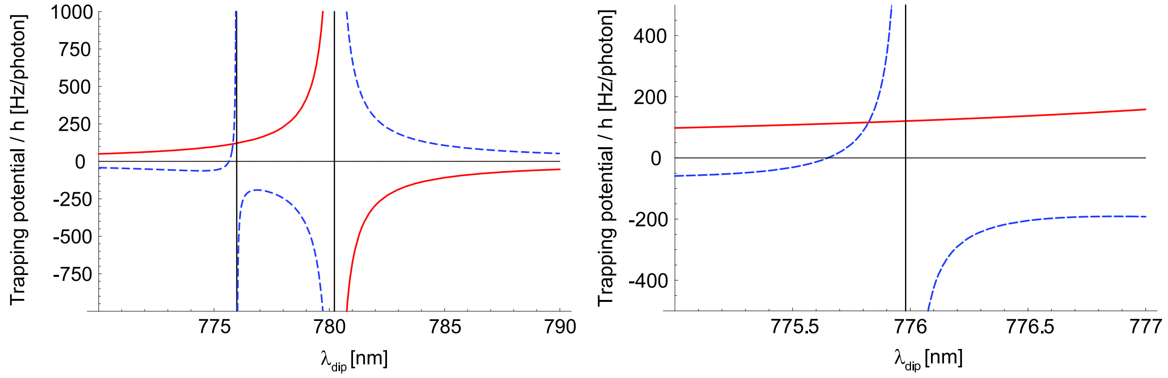
(a) Blue magic trap

(b) Zoom of (a)

**Figure B.3: Magic wavelength for circular polarization. (a)** The trapping potential per photon for an atom in the ground state $5S_{1/2}F = 3, m_f = 3$ (solid line) and in the excited state $5P_{3/2}F = 4, m_f = 4$ (dashed line) is displayed for a $\sigma_+$-polarized dipole laser. **(b)** A magic wavelength occurs at 775.8 nm, where the trapping potential is repulsive.

be used to implement longitudinal confinement in the blue trap configuration of section B.1.

In order to realize this configuration, the magic wavelength has to coincide with a cavity resonance. Therefore, the cavity length has to be carefully adjusted so that the dipole laser detuning is a multiple of the FSR. Due to the requirement that the cavity length has to be a multiple of half the wavelength of both probe light ($\lambda$) and dipole light ($\lambda_{dip}$) while the total cavity length should remain short, only distinct dipole wavelengths can be chosen. This might impede the implementation of an exactly magic trap. The maximal deviation of an allowed dipole wavelength from a desired one can be estimated: We assume that the cavity has a length of $M\lambda_{dip}/2 = (M - N)\lambda/2$, where $N$ is a small integer number describing the desired detuning $\lambda - \lambda_{dip}$ in units of the FSR. Reshaping gives $M = N\lambda/(\lambda - \lambda_{dip})$. If $M$ is integer, then the cavity length $(M - N)\lambda/2$ is resonant to both probe and dipole light. In general, $M$ will be non-integer. Then we have to choose between cavity lengths $(M'-N)\lambda/2$ or $(M'+1-N)\lambda/2$, where $M'$ is the integer which fulfills $M' < M < M'+1$, to guarantee resonance to the probe light. In this way, we enclose $\lambda_{dip}$ in an interval of the size $\delta\lambda_{dip}/\lambda = N/M' - N/(M'+1) \approx N/M^2$. For example, implementing the blue magic trap at $\lambda_{dip} = 775.8$ nm at $N = 1$ FSR detuning ($M = 177.3$) is possible within an interval of width $\delta\lambda_{dip} < 0.025$ nm for a cavity length of $L = 176\lambda/2 \approx 69$ $\mu$m. This still leads to a relatively large maximal deviation between the potentials of ground and excited state of $(U_e - U_g)/U_g \approx \pm 0.17$. This deviation can be reduced to $(U_e - U_g)/U_g \approx \pm 0.05$ if $N = 3$ is combined with a longer cavity $L = 529\lambda/2 \approx 206$ $\mu$m. The possibility of adapting the cavity length inside the vacuum chamber is provided in the recently developed new cavity setup [135]: One of the mirrors can be moved with a nm-resolution via a piezo step motor for coarse adjustment, and the second mirror is mounted on an additional piezo for

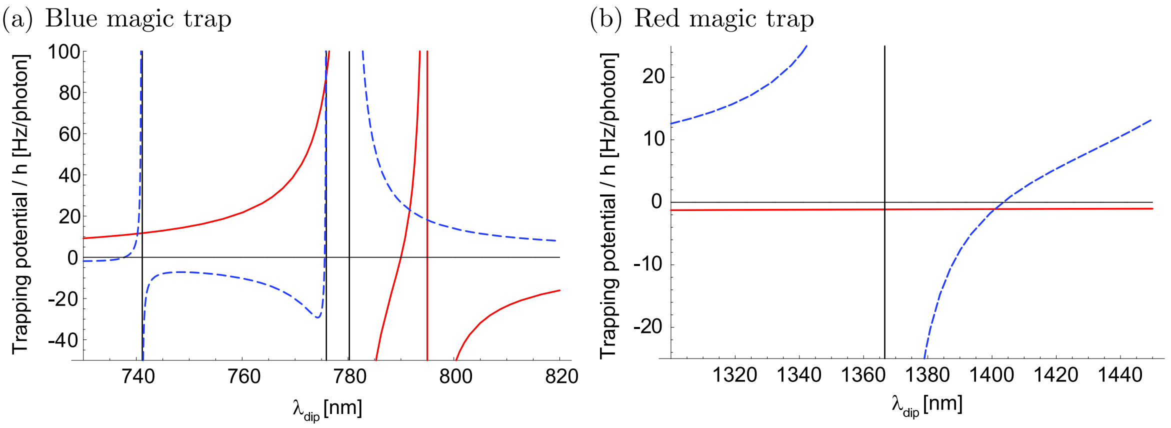
(a) Blue magic trap (b) Red magic trap

**Figure B.4: Magic wavelengths for linear polarization.** Trapping potential per photon for an atom in the ground state $5S_{1/2}F = 3, m_f = 3$ (solid line) and in the excited state $5P_{3/2}F = 4, m_f = 4$ (dashed line), for a dipole laser with linear polarization perpendicular to the quantization axis (lin⊥B). **(a)** Besides the crossing points of ground and excited state potentials at 740.2 nm and 775.8 nm, another crossing occurs at 791.6 nm, in the center between the D1 and the D2 line. The potentials are repulsive at all of these magic wavelengths. **(b)** A red magic wavelength can be found in the infrared at 1400.8 nm, arising from the coupling to the state $6S_{1/2}$.

fine-tuning. In such a blue-trap configuration, a Stark shift due to the longitudinal confinement might be largely avoided.

The new setup will also open the possibility to insert a dipole trap by shining a laser beam perpendicular to the cavity axis. If, in a new experiment, the closed near-resonant transition is maintained by keeping the small offset B-field which ensures that the quantization axis coincides with cavity axis, the purely circular dipole laser polarizations $q = \pm 1$ cannot be realized for such a beam. Instead, a basis for possible polarizations of a side beam is given by the two linear polarizations $lin \parallel B$ $(q = 0)$ or $lin \perp B$ (an equal superposition of $q = \pm 1$). The choice $(lin \perp B)$ offers different opportunities to build a magic trap (Fig. B.4): This polarization couples the state $5P_{3/2}F = 4, m_f = 4$, amongst others, to sublevels of the state $4D_{5/2}$, leading to a magic wavelength at 775.8 nm, and to $6S_{1/2}$, with a magic wavelength at 740.2 nm (the coupling to the state $4D_{3/2}$ is too weak to be of practical interest for a magic wavelength). Besides, the ground state now also couples to the state $5P_{1/2}$, which causes another magic wavelength to appear at 791.6 nm. All of these wavelengths provide repulsive potentials, hence a 3D lattice configuration is necessary in order to set up a closed trap (see Fig. B.5). In this configuration, the scattering rate of dipole photons is reduced as the atoms are stored at positions of low light intensity. Therefore, the cycling transition of the probe light would be less disturbed by such a trap as compared to a red trap. Notice that a red magic wavelength is also available, albeit at a quite large detuning ($\lambda_{dip} = 1400.8$ nm), consequently providing only a shallow potential depth per photon (Fig. B.4(b)).

The impact of using a magic trap on the efficiency of 3D cavity cooling is not yet clear, since this cooling relies on a gradient in the potential difference between ground and excited state which is largely removed in a magic trap. Applying magic

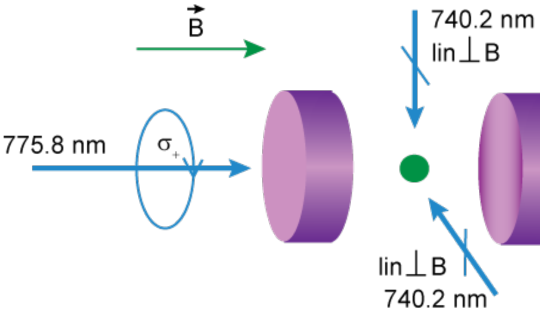

**Figure B.5: 3D magic trap.** A three-dimensional blue-detuned magic lattice for the transition $5S_{1/2}F = 3, m_f = 3 \leftrightarrow 5P_{3/2}F = 4, m_f = 4$ could be implemented by choosing trapping lasers with appropriate wavelengths and polarizations.

traps in only one of the three dimensions or tuning the gradient by adjusting the trap wavelength with respect to the magic wavelength might provide further insight into this issue.

# Bibliography

[1] M. Planck. Über das Gesetz der Energieverteilung im Normalspektrum. *Annalen der Physik* **4**, 553 (1901).

[2] A. Einstein. Über einen die Erzeugung und Verwandlung des Lichtes betreffenden heuristischen Gesichtspunkt. *Annalen der Physik* **322**, 132–148 (1905).

[3] Paul R. Berman, editor. *Cavity quantum electrodynamics.* Advances in atomic, molecular, and optical physics, New York: Academic Press, (1994).

[4] E. T. Jaynes and F. W. Cummings. Comparison of quantum and semiclassical radiation theories with application to the beam maser. *Proc. IEEE* **51**, 89–109 (1963).

[5] D. Meschede, H. Walther, and G. Müller. One-atom maser. *Phys. Rev. Lett.* **54**, 551–554 (1985).

[6] B.T.H. Varcoe, S. Brattke, B.G. Englert, and H. Walther. Fock State Rabi Oscillations; A Building Block for the Observation of New Phenomena in Quantum Optics. *Fortschr. Phys.* **48**, 679–687 (2000).

[7] S. Kuhr, S. Gleyzes, C. Guerlin, J. Bernu, U. B. Hoff, S. Deléglise, S. Osnaghi, M. Brune, J.-M. Raimond, S. Haroche, E. Jacques, P. Bosland, and B. Visentin. Ultrahigh finesse Fabry-Pérot superconducting resonator. *Applied Physics Letters* **90**, 4101 (2007).

[8] H. Walther, B. T. H. Varcoe, B.-G. Englert, and T. Becker. Cavity quantum electrodynamics. *Rep. Prog. Phys.* **69**, 1325–1382 (2006).

[9] J. M. Raimond, M. Brune, and S. Haroche. Manipulating quantum entanglement with atoms and photons in a cavity. *Rev. Mod. Phys.* **73**, 565–582 (2001).

[10] G. Rempe, H. Walther, and N. Klein. Observation of quantum collapse and revival in a one-atom maser. *Phys. Rev. Lett.* **58**, 353–356 (1987).

[11] M. Brune, F. Schmidt-Kaler, A. Maali, J. Dreyer, E. Hagley, J. M. Raimond, and S. Haroche. Quantum Rabi Oscillation: A Direct Test of Field Quantization in a Cavity. *Phys. Rev. Lett.* **76**, 1800–1803 (1996).

[12] H. M. Wiseman and G. J. Milburn. Quantum theory of field-quadrature measurements. *Phys. Rev. A* **47**, 642–662 (1993).

[13] H. J. Carmichael, H. M. Castro-Beltran, G. T. Foster, and L. A. Orozco. Giant violations of classical inequalities through conditional homodyne detection of the quadrature amplitudes of light. *Phys. Rev. Lett.* **85**, 1855–1858 (2000).

[14] Y. Zhu, D. J. Gauthier, S. E. Morin, Q. Wu, H. J. Carmichael, and T. W. Mossberg. Vacuum Rabi splitting as a feature of linear-dispersion theory: Analysis and experimental observations. *Phys. Rev. Lett.* **64**, 2499–2502 (1990).

[15] R. J. Thompson, G. Rempe, and H. J. Kimble. Observation of normal-mode splitting for an atom in an optical cavity. *Phys. Rev. Lett.* **68**, 1132 (1992).

[16] J. J. Childs, K. An, M. S. Otteson, R. R. Dasari, and M. S. Feld. Normal-mode line shapes for atoms in standing-wave optical resonators. *Phys. Rev. Lett.* **77**, 2901–2904 (1996).

[17] J. Gripp, S. L. Mielke, and L. A. Orozco. Evolution of the vacuum Rabi peaks in a detuned atom-cavity system. *Phys. Rev. A* **56**, 3262–3273 (1997).

[18] P. Maunz, T. Puppe, I. Schuster, N. Syassen, P. W. H. Pinkse, and G. Rempe. Normal-mode spectroscopy of a single-bound-atom-cavity system. *Phys. Rev. Lett.* **94**, 033002 (2005).

[19] A. Boca, R. Miller, K. M. Birnbaum, A. D. Boozer, J. McKeever, and H. J. Kimble. Observation of the Vacuum Rabi Spectrum for One Trapped Atom. *Phys. Rev. Lett.* **93**, 233603 (2004).

[20] T. Puppe, I. Schuster, A. Grothe, A. Kubanek, K. Murr, P. W. H. Pinkse, and G. Rempe. Trapping and observing single atoms in a blue-detuned intracavity dipole trap. *Phys. Rev. Lett.* **99**, 013002 (2007).

[21] H. J. Carmichael, L. Tian, W. Ren, and P. Alsing. Nonperturbative atom-photon interactions in an optical cavity. In Paul R. Berman, editor, *Cavity quantum electrodynamics*, pages 381–423. Advances in atomic, molecular, and optical physics, New York: Academic Press, (1994).

[22] L. A. Lugiato. Theory of optical bistability. In *Progress in optics*, volume 21, pages 69–216, North-Holland Physics Publishing, Amsterdam, (1984).

[23] L. Tian and H. J. Carmichael. Incoherent excitation of the Jaynes-Cummings system. *Quantum Opt.* **4**, 131–144 (1992).

[24] H. J. Carmichael, P. Kochan, and B. C. Sanders. Photon Correlation Spectroscopy. *Phys. Rev. Lett.* **77**, 631–634 (1996).

[25] L. Horvath and B. C. Sanders. Perturbative corrections to photon coincidence spectroscopy. *Journal of Physics B Atomic Molecular Physics* **34**, 3585–3606 (2001).

[26] G. Khitrova, H. M. Gibbs, M. Kira, S. W. Koch, and A. Scherer. Vacuum Rabi splitting in semiconductors. *Nature Phys.* **2**, 81–90 (2006).

[27] L. Schneebeli, M. Kira, and S. W. Koch. Characterization of strong light-matter coupling in semiconductor quantum-dot microcavities via photon-statistics spectroscopy. arXiv:quant-ph/0801.3604, (2008).

[28] G. Rempe, R. J. Thompson, R. J. Brecha, W. D. Lee, and H. J. Kimble. Optical bistability and photon statistics in cavity quantum electrodynamics. *Phys. Rev. Lett.* **67**, 1727–1730 (1991).

[29] S. L. Mielke, G. T. Foster, and L. A. Orozco. Nonclassical Intensity Correlations in Cavity QED. *Phys. Rev. Lett.* **80**, 3948–3951 (1998).

[30] G. T. Foster, L. A. Orozco, H. M. Castro-Beltran, and H. J. Carmichael. Quantum State Reduction and Conditional Time Evolution of Wave-Particle Correlations in Cavity QED. *Phys. Rev. Lett.* **85**, 3149–3152 (2000).

[31] K. M. Birnbaum, A. Boca, R. Miller, A. D. Boozer, T. E. Northup, and H. J. Kimble. Photon blockade in an optical cavity with one trapped atom. *Nature* **436**, 87–90 (2005).

[32] G. Rempe, R.J. Thompson, H.J. Kimble, and R. Lalezari. Measurement of ultralow losses in an optical interferometer. *Opt. Lett.* **17**, 363–365 (1992).

[33] C. N. Cohen-Tannoudji. Nobel Lecture: Manipulating atoms with photons. *Reviews of Modern Physics* **70**, 707–719 (1998).

[34] W. D. Phillips. Nobel Lecture: Laser cooling and trapping of neutral atoms. *Reviews of Modern Physics* **70**, 721–741 (1998).

[35] S. Chu. Nobel Lecture: The manipulation of neutral particles. *Reviews of Modern Physics* **70**, 685–706 (1998).

[36] H. Mabuchi, Q. A. Turchette, M. S. Chapman, and H. J. Kimble. Real-time detection of individual atoms falling through a high-finesse optical cavity. *Optics Letters* **21**, 1393–1395 (1996).

[37] P. Münstermann, T. Fischer, P. W. H. Pinkse, and G. Rempe. Single slow atoms from an atomic fountain observed in a high-finesse optical cavity. *Opt. Comm.* **159**, 63–67 (1999).

[38] P. W. H. Pinkse, T. Fischer, P. Maunz, and G. Rempe. Trapping an atom with single photons. *Nature* **404**, 365–368 (2000).

[39] C. J. Hood, T. W. Lynn, A. C. Doherty, A. S. Parkins, and H. J. Kimble. The atom-cavity microscope: Single atoms bound in orbit by single photons. *Science* **287**, 1447 (2000).

[40] T. W. Mossberg, M. Lewenstein, and Daniel J. Gauthier. Trapping and cooling of atoms in a vacuum perturbed in a frequency-dependent manner. *Phys. Rev. Lett.* **67**, 1723 (1991).

[41] A. C. Doherty, A. S. Parkins, S. M. Tan, and D. F. Walls. Motion of a two-level atom in an optical cavity. *Phys. Rev. A* **56**, 833 (1997).

[42] G. Hechenblaikner, M. Gangl, P. Horak, and H. Ritsch. Cooling an atom in a weakly driven high-Q cavity. *Phys. Rev. A* **58**, 3030–3042 (1998).

[43] V. Vuletić and S. Chu. Laser cooling of atoms, ions, or molecules by coherent scattering. *Phys. Rev. Lett.* **84**, 3787–3790 (2000).

[44] P. Domokos and H. Ritsch. Mechanical effects of light in optical resonators. *J. Opt. Soc. Am. B* **20**, 1098–1130 (2003).

[45] K. Murr. Large velocity capture range and low temperatures with cavities. *Phys. Rev. Lett.* **96**, 253001 (2006).

[46] P. Maunz, T. Puppe, I. Schuster, N. Syassen, P. W. H. Pinkse, and G. Rempe. Cavity cooling of a single atom. *Nature* **428**, 50–52 (2004).

[47] J. Ye, D. W. Vernooy, and H. J. Kimble. Trapping of single atoms in cavity QED. *Phys. Rev. Lett.* **83**, 4987–4990 (1999).

[48] J. McKeever, J. R. Buck, A. D. Boozer, A. Kuzmich, H.-C. Nägerl, D. M. Stamper-Kurn, and H. J. Kimble. State-insensitive cooling and trapping of single atoms in an optical cavity. *Phys. Rev. Lett.* **90**, 133602 (2003).

[49] Y. Miroshnychenko, W. Alt, I. Dotsenko, L. Förster, M. Khudaverdyan, D. Meschede, D. Schrader, and A. Rauschenbeutel. Quantum engineering: An atom-sorting machine. *Nature* **442**, 151 (2006).

[50] S. Nußmann, M. Hijlkema, B. Weber, F. Rohde, G. Rempe, and A. Kuhn. Submicron Positioning of Single Atoms in a Microcavity. *Phys. Rev. Lett.* **95**, 173602 (2005).

[51] Kevin M. Fortier, Soo Y. Kim, Michael J. Gibbons, Peyman Ahmadi, and Michael S. Chapman. Deterministic loading of individual atoms to a high-finesse optical cavity. *Phys. Rev. Lett.* **98**, 233601 (2007).

[52] Mkrtych Khudaverdyan, Wolfgang Alt, Igor Dotsenko, Tobias Kampschulte, Karim Lenhard, Arno Rauschenbeutel, Sebastian Reick, Karsten Schörner, Artur Widera, and Dieter Meschede. Controlled insertion and retrieval of atoms coupled to a high-finesse optical resonator. arXiv:quant-ph/0805.0765, (2008).

[53] S. Nußmann, K. Murr, M. Hijlkema, B. Weber, A. Kuhn, and G. Rempe. Vacuum-stimulated cooling of single atoms in three dimensions. *Nature Phys.* **1**, 122–125 (2005).

[54] K. Murr, S. Nußmann, T. Puppe, M. Hijlkema, B. Weber, S. C. Webster, A. Kuhn, and G. Rempe. Three-dimensional cavity cooling and trapping in an optical lattice. *Phys. Rev. A* **73**, 063415 (2006).

[55] C. J. Hood, M. S. Chapman, T. W. Lynn, and H. J. Kimble. Real-Time Cavity QED with Single Atoms. *Phys. Rev. Lett.* **80**, 4157–4160 (1998).

[56] R. J. Thompson, Q. A. Turchette, O. Carnal, and H. J. Kimble. Nonlinear spectroscopy in the strong-coupling regime of cavity QED. *Phys. Rev. A* **57**, 3084–3104 (1998).

[57] I. Schuster, A. Kubanek, A. Fuhrmanek, T. Puppe, P. W. H. Pinkse, K. Murr, and G. Rempe. Nonlinear spectroscopy of photons bound to one atom. *Nature Phys.* **4**, 382–385 (2008).

[58] Howard Carmichael. Cavity qed: Signs of anharmonicity. *Nature Phys.* **4**, 346–347 (2008).

[59] H. Mabuchi and A. C. Doherty. Cavity Quantum Electrodynamics: Coherence in Context. *Science* **298**, 1372–1377 (2002).

[60] S. Haroche. Cavity quantum electrodynamics. In J. Dalibard, J. M. Raimond, and J. Zinn-Justin, editors, *Fundamental Systems in Quantum Optics, Les Houches, Session LIII, 1990*, page 767, North-Holland, Amsterdam, (1992). Elsevier Science.

[61] M. Tavis and F. W. Cummings. The exact solution of N two level systems interacting with a single mode, quantized radiation field. *Phys. Lett. A* **25**, 714–715 (1967).

[62] H. Carmichael. *An Open Systems Approach to Quantum Optics.* Springer-Verlag, Berlin, (1993).

[63] P. Alsing, D.-S. Guo, and H. J. Carmichael. Dynamic Stark effect for the Jaynes-Cummings system. *Phys. Rev. A* **45**, 5135–5143 (1992).

[64] H.J. Briegel and B.G. Englert. Quantum optical master equation: The use of dampling bases. *Phys. Rev. A* **47**, 3311 (1993).

[65] Pierre Meystre and Murray III Sargent. *Elements of Quantum Optics.* Springer Verlag, Berlin, third edition, (1999).

[66] H.J. Carmichael. *Statistical Methods in Quantum Optics 1: Master Equations and Fokker-Planck Equations.* Springer Verlag, Berlin, (1999).

[67] C. Cohen-Tannoudji, J. Dupont-Roc, and G. Grynberg. *Atom-photon interactions.* J. Wiley & Sons, (1998).

[68] A.C. Doherty and H. Mabuchi. Atoms in microcavities: quantum electrodynamics, quantum statistical mechanics, and quantum information science. In K. Vahala, editor, *Optical microcavities*, pages 367–414. Advanced Series in Applied Physics, Volume 5: World Scientific, (2004).

[69] K. Murr. On the suppression of the diffusion and the quantum nature of a cavity mode. Optical bistability: forces and friction in driven cavities. *J. Phys. B* **36**, 2515 (2003).

[70] Yves Colombe, Tilo Steinmetz, Guilhem Dubois, Felix Linke, David Hunger, and Jakob Reichel. Strong atom-field coupling for Bose-Einstein condensates in an optical cavity on a chip. *Nature* **450**, 272–276 (2007).

[71] Ferdinand Brennecke, Tobias Donner, Stephan Ritter, Thomas Bourdel, Michael Kohl, and Tilman Esslinger. Cavity QED with a Bose-Einstein condensate. *Nature* **450**, 268–271 (2007).

[72] J. P. Reithmaier, G. Sęk, A. Löffler, C. Hofmann, S. Kuhn, S. Reitzenstein, L. V. Keldysh, V. D. Kulakovskii, T. L. Reinecke, and A. Forchel. Strong coupling in a single quantum dot-semiconductor microcavity system. *Nature* **432**, 197–200 (2004).

[73] David Press, Stephan Gotzinger, Stephan Reitzenstein, Carolin Hofmann, Andreas Loffler, Martin Kamp, Alfred Forchel, and Yoshihisa Yamamoto. Photon antibunching from a single quantum-dot-microcavity system in the strong coupling regime. *Phys. Rev. Lett.* **98**, 117402 (2007).

[74] E. Peter, P. Senellart, D. Martrou, A. Lemaitre, J. Hours, J. M. Gerard, and J. Bloch. Exciton-photon strong-coupling regime for a single quantum dot embedded in a microcavity. *Phys. Rev. Lett.* **95**, 067401 (2005).

[75] T. Yoshie, A. Scherer, J. Hendrickson, G. Khitrova, H. M. Gibbs, G. Rupper, C. Ell, O. B. Shchekin, and D. G. Deppe. Vacuum Rabi splitting with a single quantum dot in a photonic crystal nanocavity. *Nature* **432**, 200–203 (2004).

[76] A. Wallraff, D. I. Schuster, A. Blais, L. Frunzio, R.-S. Huang, J. Majer, S. Kumar, S. M. Girvin, and R. J. Schoelkopf. Strong coupling of a single photon to a superconducting qubit using circuit quantum electrodynamics. *Nature* **431**, 162 (2004).

[77] H. M. Gibbs, S. L. McCall, and T. N. C. Venkatesan. Differential gain and bistability using a sodium-filled fabry-perot interferometer. *Phys. Rev. Lett.* **36**, 1135–1138 (1976).

[78] Th. Elsässer, B. Nagorny, and A. Hemmerich. Optical bistability and collective behavior of atoms trapped in a high-q ring cavity. *Phys. Rev. A* **69**, 033403 (2004).

[79] C. M. Savage and H. J. Carmichael. Single atom optical bistability. *IEEE* **24**, 1495–1498 (1988).

[80] P. R. Rice and H. J. Carmichael. Single-atom cavity-enhanced absorption. I. Photon statistics in the bad-cavity limit. *IEEE* **24**, 1351–1366 (1988).

[81] D. M. Meekhof, C. Monroe, B. E. King, W. M. Itano, and D. J. Wineland. Generation of nonclassical motional states of a trapped atom. *Phys. Rev. Lett.* **76**, 1796–1799 (1996).

[82] Christine Guerlin, Julien Bernu, Samuel Deleglise, Clement Sayrin, Sebastien Gleyzes, Stefan Kuhr, Michel Brune, Jean-Michel Raimond, and Serge Haroche. Progressive field-state collapse and quantum non-demolition photon counting. *Nature* **448**, 889–893 (2007).

[83] H. J. Carmichael, R. J. Brecha, and P. R. Rice. Quantum interference and collapse of the wavefunction in cavity QED. *Opt. Comm.* **82**, 73–79 (1991).

[84] B. Dayan, A. S. Parkins, T. Aoki, E. P. Ostby, K. J. Vahala, and H. J. Kimble. A Photon Turnstile Dynamically Regulated by One Atom. *Science* **319**, 1062– (2008).

[85] Andrei Faraon, Ilya Fushman, Dirk Englund, Nick Stoltz, Pierre Petroff, and Jelena Vučković. Coherent generation of nonclassical light on a chip via photon-induced tunneling and blockade. arXiv:quant-ph/0804.2740v1, (2008).

[86] R. J. Schoelkopf and S. M. Girvin. Wiring up quantum systems. *Nature* **451**, 664–669 (2008).

[87] M. A. Sillanpää, J. I. Park, and R. W. Simmonds. Coherent quantum state storage and transfer between two phase qubits via a resonant cavity. *Nature* **449**, 438–442 (2007).

[88] F. Deppe, M. Mariantoni, E. P. Menzel, A. Marx, S. Saito, K. Kakuyanagi, H. Tanaka, T. Meno, K. Semba, H. Takayanagi, E. Solano, and R. Gross. Two-photon probe of the Jaynes-Cummings model and symmetry breaking in circuit QED. arXiv:cond-mat/0805.3294, (2008).

[89] I. Chiorescu, P. Bertet, K. Semba, Y. Nakamura, C. J. P. M. Harmans, and J. E. Mooij. Coherent dynamics of a flux qubit coupled to a harmonic oscillator. *Nature* **431**, 159–162 (2004).

[90] J. Johansson, S. Saito, T. Meno, H. Nakano, M. Ueda, K. Semba, and H. Takayanagi. Vacuum Rabi Oscillations in a Macroscopic Superconducting Qubit LC Oscillator System. *Phys. Rev. Lett.* **96**, 127006 (2006).

[91] D. I. Schuster, A. A. Houck, J. A. Schreier, A. Wallraff, J. M. Gambetta, A. Blais, L. Frunzio, J. Majer, B. Johnson, M. H. Devoret, S. M. Girvin, and R. J. Schoelkopf. Resolving photon number states in a superconducting circuit. *Nature* **445**, 515–518 (2007).

[92] A. Zrenner. A close look on single quantum dots. *J. Chem. Phys.* **112**, 7790–7798 (2000).

[93] K. Vahala, editor. *Optical microcavities.* Advanced Series in Applied Physics, Volume 5: World Scientific, (2004).

[94] K. Srinivasan and O. Painter. Linear and nonlinear optical spectroscopy of a strongly-coupled microdisk-quantum dot system. *Nature* **450**, 862–865 (2007).

[95] K. Hennessy, A. Badolato, M. Winger, D. Gerace, M. Atatüre, S. Gulde, S. Fält, E. L. Hu, and A. Imamoğlu. Quantum nature of a strongly coupled single quantum dot-cavity system. *Nature* **445**, 896–899 (2007).

[96] D. Englund, A. Faraon, N. Stoltz, P. Petroff, and J. Vučković. Controlling cavity reflectivity with a single quantum dot. *Nature* **450**, 857–861 (2007).

[97] N. Syassen. Linear and nonlinear spectroscopy of a strongly-coupled atom-cavity system. Diplomarbeit, Technische Universität München, (2004).

[98] T.A. Puppe. Trapping and observing single atoms in the dark. Ph.D. Thesis, Technische Universität München, (2007).

[99] A. Yariv. *Quantum Electronics.* J. Wiley & Sons, New York, 3rd edition, (1989).

[100] A. Fuhrmanek. Multiphoton transitions in a strongly-coupled atom-cavity system. Diplomarbeit, Technische Universität München, (2008).

[101] Stephen E. Harris. Electromagnetically induced transparency. (cover story). *Physics Today* **50**, 36 (1997).

[102] B. R. Mollow. Two-photon absorption and field correlation functions. *Phys. Rev.* **175**, 1555–1563 (1968).

[103] J. Janszky and Y. Yushin. Many-photon processes with the participation of squeezed light. *Phys. Rev. A* **36**, 1288–1292 (1987).

[104] N. Ph. Georgiades, E. S. Polzik, K. Edamatsu, H. J. Kimble, and A. S. Parkins. Nonclassical excitation for atoms in a squeezed vacuum. *Phys. Rev. Lett.* **75**, 3426–3429 (1995).

[105] D. F. Walls. Evidence for the quantum nature of light. *Nature* **280**, 451 (1979).

[106] R. Grimm and M. Weidemüller. Optical Dipole Traps for Neutral Atoms. In B. Bederson and H. Walther, editors, *Advances in atomic, molecular, and optical physics*, volume 42, pages 95–170. Elsevier Science, (1999).

[107] J. Dalibard and C. Cohen-Tannoudji. Atomic motion in laser light: connection between semiclassical and quantum descriptions. *J. Phys. B* **18**, 1661 (1985).

[108] P. Maunz. Cavity cooling and spectroscopy of a bound atom-cavity system. Ph.D. Thesis, Technische Universität München, (2004).

[109] J. P. Gordon and A. Ashkin. Motion of atoms in a radiation trap. *Phys. Rev. A* **21**, 1606 (1980).

[110] J.D. Jackson. *Klassische Elektrodynamik.* de Gruyter, Berlin, 2nd edition, (1982).

[111] G. Rempe and K. Murr. Light Forces In Cavity QED. In C. Roos, H. Haffner, and R. Blatt, editors, *Atomic Physics 20*, volume 869 of *American Institute of Physics Conference Series*, pages 136–143, (2006).

[112] P. Münstermann, T. Fischer, P. Maunz, P. W. H. Pinkse, and G. Rempe. Dynamics of Single-Atom Motion Observed in a High-Finesse Cavity. *Phys. Rev. Lett.* **82**, 3791–3794 (1999).

[113] T. Puppe, I. Schuster, P. Maunz, K. Murr, P. W. H. Pinkse, and G. Rempe. Light force fluctuations in a strongly coupled atom-cavity system. *J. Mod. Opt.* **54**, 1927–1937 (2007).

[114] H. Schwarz. *Numerische Mathematik.* B.G. Teubner, Stuttgart, (1997).

[115] W.H. Press, S.A. Teukolsky, W.T. Vettering, and B.P. Flannery. *Numerical Recipes in C++.* Cambridge University Press, (2002).

[116] M. Matsumoto and T. Nishimura. Mersenne twister: A 623-dimensionally equidistributed uniform pseudorandom number generator. *ACM Trans. on Modeling and Computer Simulations* , (1998).

[117] T. A. Savard, K. M. O'hara, and J. E. Thomas. Laser-noise-induced heating in far-off resonance optical traps. *Phys. Rev. A* **56**, 1095 (1997).

[118] I. Schuster. Beobachtung und Speicherung von Atomen in einem optischen Resonator hoher Finesse. Diplomarbeit, Technische Universität München, (2003).

[119] Harold J. Metcalf and Peter van der Straten. *Laser Cooling and Trapping (Graduate Texts in Contemporary Physics).* Springer, (2001).

[120] P. Münstermann. Dynamik einzelner Atome in einem optischen Resonator höchster Finesse. Ph.D. Thesis, Universität Konstanz, (1999).

[121] R. Hanbury Brown and R. Q. Twiss. A test of a new type of stellar interferometer on Sirius. *Nature* **178**, 1046 (1956).

[122] D. E. Chang, A. S. Sørensen, E. A. Demler, and M. D. Lukin. A single-photon transistor using nano-scale surface plasmons. *Nature Phys.* **3**, 807–812 (2007).

[123] L.-M. Duan and H. J. Kimble. Scalable photonic quantum computation through cavity-assisted interactions. *Phys. Rev. Lett.* **92**, 127902 (2004).

[124] M. Soljačić and J. D. Joannopoulos. Enhancement of nonlinear effects using photonic crystals. *Nature Materials* **3**, 211–219 (2004).

[125] E. Knill, R. Laflamme, and G. J. Milburn. A scheme for efficient quantum computation with linear optics. *Nature* **409**, 46–52 (2001).

[126] C. Monroe. Quantum information processing with atoms and photons. *Nature* **416**, 238–246 (2002).

[127] W. H. Zurek. Decoherence and the transition from quantum to classical – revisited. *arXiv:quant-ph/0306072v1* , (2003).

[128] M. A. Armen and H. Mabuchi. Low-lying bifurcations in cavity quantum electrodynamics. *Phys. Rev. A* **73**, 063801 (2006).

[129] H. J. Carmichael. Photon antibunching and squeezing for a single atom in a resonant cavity. *Phys. Rev. Lett.* **55**, 2790–2793 (1985).

[130] J. E. Reiner, W. P. Smith, L. A. Orozco, H. J. Carmichael, and P. R. Rice. Time evolution and squeezing of the field amplitude in cavity QED. *J. Opt. Soc. Am. B* **18**, 1911–1921 (2001).

[131] H. Mabuchi and H. M. Wiseman. Retroactive Quantum Jumps in a Strongly Coupled Atom-Field System. *Physical Review Letters* **81**, 4620–4623 (1998).

[132] C.W. Gardiner and P. Zoller. *Quantum Noise.* Springer, Berlin, 2nd edition, (1999).

[133] W. P. Smith, J. E. Reiner, L. A. Orozco, S. Kuhr, and H. M. Wiseman. Capture and Release of a Conditional State of a Cavity QED System by Quantum Feedback. *Phys. Rev. Lett.* **89**, 133601 (2002).

[134] R. van Handel, J. K. Stockton, and H. Mabuchi. REVIEW ARTICLE: Modelling and feedback control design for quantum state preparation. *Journal of Optics B: Quantum and Semiclassical Optics* **7**, 179 (2005).

[135] J. Almer. Aufbau und Charakterisierung eines längenveränderbaren optischen Hoch-Finesse-Resonators. Diplomarbeit, Technische Universität München, (2006).

[136] A. Grothe. Blau verstimmte Resonatormoden als Dipolfalle für einzelne Atome. Diplomarbeit, Technische Universität München, (2005).

[137] Hidetoshi Katori, Masao Takamoto, V. G. Pal'chikov, and V. D. Ovsiannikov. Ultrastable Optical Clock with Neutral Atoms in an Engineered Light Shift Trap. *Phys. Rev. Lett.* **91**, 173005 (2003).

[138] Tetsuya Ido and Hidetoshi Katori. Recoil-Free Spectroscopy of Neutral Sr Atoms in the Lamb-Dicke Regime. *Phys. Rev. Lett.* **91**, 053001 (2003).

[139] Carsten Degenhardt, Hardo Stoehr, Uwe Sterr, Fritz Riehle, and Christian Lisdat. Wavelength-dependent ac Stark shift of the $^1S_0 - ^3P_1$ transition at 657 nm in Ca. *Phys. Rev. A* **70**, 023414 (2004).

[140] Peter L. Smith, Claas Heise, Jim R. Esmond, and Robert L. Kurucz. Atomic spectral line database, built from R.L. Kurucz' CD-ROM 23.

[141] I. H. Deutsch and P. S. Jessen. Quantum-state control in optical lattices. *Phys. Rev. A* **57**, 1972–1986 (1998).

[142] Y.-N. Zheng, X.-J. Zhou, J.-B. Chen, and X.-Z. Chen. Magic Wavelength for Caesium Transition Line $6S_{1/2}$ $6P_{3/2}$. *Chinese Physics Letters* **23**, 1687–1690 (2006).

# List of Publications

I. Schuster, A. Kubanek, A. Fuhrmanek, T. Puppe, P. W. H. Pinkse, K. Murr, and G. Rempe. Nonlinear spectroscopy of photons bound to one atom. *Nature Phys.* **4**, 382-385 (2008).

T. Puppe, I. Schuster, A. Grothe, A. Kubanek, K. Murr, P. W. H. Pinkse, and G. Rempe. Trapping and observing single atoms in a blue-detuned intracavity dipole trap. *Phys. Rev. Lett.* **99**, 013002 (2007).

T. Puppe, I. Schuster, P. Maunz, K. Murr, P. W. H. Pinkse, and G. Rempe. Light force fluctuations in a strongly coupled atom-cavity system. *J. Mod. Opt.* **54**, 1927–1937 (2007).

K. Murr, P. Maunz, P. W. H. Pinkse, T. Puppe, I. Schuster, D. Vitali, and G. Rempe. Momentum diffusion for coupled atom-cavity oscillators. *Phys. Rev. A* **74**, 043412 (2006).

P. Maunz, T. Puppe, I. Schuster, N. Syassen, P. W. H. Pinkse, and G. Rempe. Normal-mode spectroscopy of a single-bound-atom-cavity system. *Phys. Rev. Lett.* **94**, 033002 (2005).

P. Maunz, T. Puppe, I. Schuster, N. Syassen, P. W. H. Pinkse, and G. Rempe. Cavity cooling of a single atom. *Nature* **428**, 50-52 (2004).

# List of Symbols

| | |
|---|---|
| $\bar{\beta}$ | friction tensor |
| $c$ | speed of light |
| C | cooperativity $g^2/(2\gamma\kappa)$ |
| $d_{ge}$ | reduced dipole transition matrix element |
| $\bar{D}_{sp}$ | diffusion tensor describing spontaneous emission |
| $\bar{D}_{dp}$ | diffusion tensor describing dipole force fluctuations |
| $\Delta_a$ | probe - atom detuning $\omega_l - \omega_a$ |
| $\Delta_a(\boldsymbol{r})$ | local probe - atom detuning $\Delta_{a,0} - 2S(\boldsymbol{r})$ |
| $\Delta_{ac}$ | atom-cavity detuning $\omega_c - \omega_a$ |
| $\Delta_{a,0}$ | probe - bare-atom detuning $\omega_l - \omega_{a,0}$ |
| $\Delta_c$ | probe - cavity detuning $\omega_l - \omega_c$ |
| $\tilde{\Delta}_a$ | complex probe-atom detuning $\Delta_a + i\gamma$ |
| $\tilde{\Delta}_c$ | complex probe-cavity detuning $\Delta_c + i\kappa$ |
| $\Delta_{dip}$ | detuning between dipole trap light and atom |
| $\varepsilon_0$ | permittivity of the vacuum |
| $\eta$ | strength of the pump field |
| $\mathcal{F}$ | cavity finesse (490 000) |
| FSR | free spectral range of the cavity ($2\pi \times 1.21$ THz) |
| $g$ | coupling strength of the atom to the probe light |
| $g_0$ | coupling strength of the atom to the probe light at an antinode ($2\pi \times 16$ MHz) |
| $g(\boldsymbol{r})$ | local coupling $g_0\ \psi(\boldsymbol{r})$ |
| $g_{dip}$ | maximal coupling strength of the atom to the dipole light ($2\pi \times 16$ MHz) |
| $\gamma$ | decay rate of the atomic polarization ($2\pi \times 3$ MHz) |

| | |
|---|---|
| $\kappa$ | decay rate of the intracavity field ($2\pi \times 1.25$ MHz) |
| $k$ | wavenumber of the probe light ($2\pi/\lambda$) |
| $k_{dip}$ | wavenumber of the probe light ($2\pi/\lambda_{dip}$) |
| $\lambda$ | wavelength of the probe light (780.2 nm) |
| $\lambda_{dip}$ | wavelength of the dipole light (785.2 nm) |
| $L$ | cavity length (123 $\mu$m) |
| $\mathcal{L}$ | Liouville superoperator |
| $\tilde{\mathcal{L}}$ | dual Liouville superoperator |
| $m$ | mass of $^{85}$Rb ($1.42 \times 10^{-25}$ kg) |
| $n_s$ | saturation photon number $\gamma^2/2g^2$ |
| $\nu$ | complex cooperativity $g^2/(\tilde{\Delta}_a\tilde{\Delta}_c)$ |
| $P_{pump}$ | power of the impinging probe light |
| $P_{dip}$ | power of the dipole trap |
| $\psi_{dip}(\boldsymbol{r})$ | spatial mode function of the dipole trap mode |
| $\psi(\boldsymbol{r})$ | spatial mode function of the near-resonant cavity mode |
| $s_0$ | saturation parameter of optical bistability |
| $S$ | Stark shift of the atomic ground state |
| $S_0$ | maximal Stark shift of the atomic ground state at an antinode of the trap |
| $S(\boldsymbol{r})$ | local Stark shift of the atomic ground state $S_0 \, \lvert\psi_{dip}(\boldsymbol{r})\rvert^2$ |
| $U_g(\boldsymbol{r})$ | potential of the dipole trap for the ground state |
| $U_e(\boldsymbol{r})$ | potential of the dipole trap for the excited state |
| $V$ | cavity volume ($\pi w_0^2 L/4$) |
| $w_0$ | mode waist (29 $\mu$m) |
| $\omega_l$ | probe frequency |
| $\omega_{a,0}$ | bare atom resonance frequency |
| $\omega_a$ | Stark-shifted atom resonance frequency $\omega_{a,0} - 2S$ |
| $\omega_c$ | cavity resonance frequency |

# Danksagung

Zunächst danke ich meinem Doktorvater Gerhard Rempe, der mir die Gelegenheit gab, an diesem spannenden Experiment mitzuwirken, für das entgegengebrachte Vertrauen und für viele hilfreiche Diskussionen und Kommentare. Er schaffte es mit seiner Begeisterung an der Physik, auch mich immer wieder neu zu motivieren.

Desweiteren danke ich Karim Murr, der das Projekt der Mehrphotonen-Spektroskopie angeregt und mit mir zusammen durchgeführt hat, für die gute Zusammenarbeit, viele ausführliche Diskussionen und auch dafür, dass er mir die Theorie des Atom-Resonator-Systems nähergebracht hat.

Eine solch umfangreiche und komplexe Apparatur kann nur von einem Team von Mitarbeitern gehandhabt werden; mein Dank gilt daher allen früheren und jetzigen Mitgliedern des Cavity-Teams für ihren Beitrag zum Aufbau und zur Verbesserung des Systems. Insbesondere danke ich Pepijn Pinkse für seine stetige Unterstützung und meinen direkten Vorgängern Peter Maunz und Thomas Puppe, die mich in die Geheimnisse des Experimentierens im allgemeinen und des bestehenden Messaufbaus im besonderen eingeführt haben und die mir die Apparatur in einem hervorragenden Zustand überlassen haben. Zudem danke ich Alexander Kubanek für seine große Hilfe bei der Durchführung der recht zeitintensiven Messungen, und Andreas Fuhrmanek für sein Engagement beim Voranbringen der Simulationen, welche einen wichtigen Beitrag zum Verständnis der Messergebnisse geleistet haben.

Ein ebenfalls wichtiger Beitrag zur Umsetzung jeglicher Messungen besteht in der technischen Unterstützung, die in unserer Gruppe in vorbildlicher Weise von Franz Denk, Helmuth Stehbeck und Tom Wiesmeier geleistet wird. Auch dafür herzlichen Dank.

Ich danke auch Sepp Bayerl für seine Ausdauer und guten Ideen bei der Planung und Konstruktion einer neuen längenveränderbaren Resonatorhalterung. Johannes Almer danke ich für seine Umsicht und Geduld beim Spiegelputzen und seine Hilfe beim Aufbau und Test des neuen Resonators, zu dessen Einbau es während meiner Zeit am Experiment nun leider nicht mehr kommt. Ich danke Markus Koch und Borys Hagemann dafür, dass sie die Arbeit am neuen Resonator fortführen, und wünsche ihnen viel Erfolg.

Bei der ganzen Quantendynamik-Abteilung möchte ich mich für die angenehme Atmosphäre bedanken, die stets von Kameradschaftlichkeit und großer Hilfsbereitschaft geprägt war. Dadurch ging der Spaß an der Arbeit nie verloren.

Zuletzt bedanke ich mich ganz herzlich bei meinen Eltern, Verwandten und Freunden für ihre bedingungslose Unterstützung während der vergangenen Jahre und für ihre Bemühungen, mich die Welt außerhalb der Physik nicht vergessen zu lassen.